

# Shock propagation in dilute inelastic and elastic media

*By*

**Jilmy P Joy**

**PHYS10201205012**

**The Institute of Mathematical Sciences, Chennai**

*A thesis submitted to the*

*Board of Studies in Physical Sciences*

*In partial fulfillment of requirements*

*For the Degree of*

**DOCTOR OF PHILOSOPHY**

*of*

**HOMI BHABHA NATIONAL INSTITUTE**



**April, 2019**



# Shock propagation in dilute inelastic and elastic media

*By*

**Jilmy P Joy**

**PHYS10201205012**

**The Institute of Mathematical Sciences, Chennai**

*A thesis submitted to the*

*Board of Studies in Physical Sciences*

*In partial fulfillment of requirements*

*For the Degree of*

**DOCTOR OF PHILOSOPHY**

*of*

**HOMI BHABHA NATIONAL INSTITUTE**



**April, 2019**



# Homi Bhabha National Institute

## Recommendations of the Viva Voce Committee

As members of the Viva Voce Committee, we certify that we have read the dissertation prepared by Jilmy P Joy entitled "Shock Propagation in dilute inelastic and elastic media" and recommend that it maybe accepted as fulfilling the thesis requirement for the award of Degree of Doctor of Philosophy.



Date: 16-10-2020

Chairman: Sitabhra Sinha



Date: 16/10/2020

Guide/Convener: Rajesh Ravindran



Date: Oct 16 2020

Member 1: Satyavani Vemparala



Date: 16/10/2020

Member 2: Pinaki Chaudhuri



Date: 16 Oct. 2020

External Examiner: Sanjay Puri

Final approval and acceptance of this dissertation is contingent upon the candidate's submission of the final copies of the dissertation to HBNI.

I hereby certify that I have read this dissertation prepared under my direction and recommend that it may be accepted as fulfilling the dissertation requirement.

Date: 16/10/2020

Place: CHENNAI



RAJESH RAVINDRAN

Guide



## STATEMENT BY AUTHOR

This dissertation has been submitted in partial fulfillment of requirements for an advanced degree at Homi Bhabha National Institute (HBNI) and is deposited in the Library to be made available to borrowers under rules of the HBNI.

Brief quotations from this dissertation are allowable without special permission, provided that accurate acknowledgement of source is made. Requests for permission for extended quotation from or reproduction of this manuscript in whole or in part may be granted by the Competent Authority of HBNI when in his or her judgement the proposed use of the material is in the interests of scholarship. In all other instances, however, permission must be obtained from the author.



Jilmy P Joy  
16/10/2020

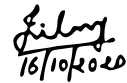
Jilmy P Joy





## DECLARATION

I, hereby declare that the investigation presented in the thesis has been carried out by me.  
The work is original and has not been submitted earlier as a whole or in part for a degree  
/ diploma at this or any other Institution / University.



Jilmy  
16/10/2020

Jilmy P Joy



## **DEDICATIONS**

*To My Parents*

*&*

*Sister*



## ACKNOWLEDGEMENTS

Firstly, I wish to express my sincere gratitude to my supervisor, **Prof. R. Rajesh** for the continuous support of my Ph.D. work and related research, for the patience, motivation, and immense knowledge and for the belief on me. Your guidance helped me in all the time of research and writing of this thesis. It is one of the blessings from God, to get an opportunity to work with you!

I thank my collaborator Prof. Dibyendu Das, for the discussions and knowledge sharing with patience during the work. A special gratitude goes out to Dr. Sudhir, who was accessible for the discussions, especially regarding computer programming, with great patience and was always willing to help and clarify even silly doubts.

The members of my doctoral committee, Prof. Sitabhra Sinha, Prof. Satyavani Vemparala, and Dr. Pinaki Chaudhuri, I am grateful to you for the interactions, critical questions, and suggestions.

The teachers who taught me during the course work period and the members of my monitoring committee, thank you so much for your continuous evaluation and support.

Prof. Indumathi D., I am grateful to you for standing with me when I was going through a hard situation in IMSc. I do remember your help, support, and motivations.

With a special mention to the high-performance computing facility in IMSc, I would like to thank Mr. Mangal Pandi and Mr. Srinivasan for the timely technical support.

I am thankful to all the administrative staffs in IMSc, especially Mr. Vishnu Prasad, and Mrs. Indra, for making my stay in IMSc smooth and pleasant.

My sincere thanks to all my classmates during the course work, and Ankita, Arjun, Di-

vakaran, Dipanjan, Lakshmi, Minati, late Pavan, Pooja, Prasad, Prasanna, Rathul, Renjan, and Vigneshwar for the discussions, helps, and supports. Also, my special hearty thanks to Anvy, Arya, and Meghna for being there for academic and non-academic cases.

I thank all my teachers from childhood for the support and motivation. I thank Somy, Divya, and Sr. Jasmine for being there. I specially thank Fr. Mani for the spiritual support and motivation.

Rinjo, I thank you so much for being there always and finding time for me.

I thank my grandma, all my relatives and friends from childhood till now who have supported me along the way.

Heartfelt thanks go to Chettayi, for the support and motivations. Iva, your presence, talks, and smile gave me happiness and relief from tensions and worries.

*Daddy and Mommy*, I owe it all to you! Your love, guidance, and encouragement always helped me to overcome any obstacles. You are my ultimate role models. *Chechy*, your love and guidance always helped me to handle situations. It is all you three, who have provided me through moral and emotional support, and positivity in my life. I am gratefully indebted to you always for supporting me spiritually throughout writing this thesis and my life in general. This thesis is dedicated to you three, with affection.

Finally, I thank almighty God for what I am, giving me nice family, good opportunity, etc.

## List of Publications arising from the thesis

- **Journal**

1. **Shock propagation in locally driven granular systems**

J. P. Joy, S. N. Pathak, D. Das, and R. Rajesh

*Physical Review E* **96**, 032908 (2017)

- **Others**

1. **Shock propagation following an intense explosion: comparison between hydrodynamics and simulations**

J. P. Joy, S. N. Pathak, and R. Rajesh

*arXiv* : 1812.03638 [cond-mat.stat-mech]

2. **Shock propagation in the hard sphere gas in two dimensions: comparison between simulations and hydrodynamics**

J. P. Joy, and R. Rajesh

*arXiv* : 1907.03416 [cond-mat.stat-mech]



Jilmy P Joy  
16/10/2020

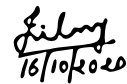
Jilmy P Joy





## List of presentations and participations at conferences

- *Fracmeet 2019*, IMSc Chennai, 04-07 March 2019
- *One Day Soft Matter Symposium*, IIT Madras, 25th January, 2019
- Poster presentation, *Indian Statistical Physics Community Meeting 2018* (ISPCM 2018), ICTS Bangalore, 16-18 February, 2018
- Poster presentation, *Fracmeet 2018*, IMSc Chennai, 05-09 February 2018
- *CompFlu 2017*, IIT Madras, 18-20 December, 2017
- Poster presentation, *Indian Statistical Physics Community Meeting 2017* (ISPCM 2017), ICTS Bangalore, 17-19 February, 2017
- *Fracmeet 2017*, IMSc Chennai, 04-07 January 2017
- *Bangalore School on Statistical Physics - VII*, ICTS Bangalore, 01-15 July, 2016
- *Fracmeet 2016*, IMSc Chennai, 01-04 February 2016
- *Bangalore School on Statistical Physics -VI*, RRI Bangalore, 02-18 July 2015



Jilmy P Joy



# Contents

<b>Contents</b>	<b>i</b>
<b>Synopsis</b>	<b>1</b>
<b>List of Figures</b>	<b>11</b>
<b>List of Tables</b>	<b>20</b>
<b>1 Introduction</b>	<b>21</b>
1.1 Shock propagation in dilute elastic gas . . . . .	22
1.2 Shock propagation in dilute inelastic gas . . . . .	25
1.2.1 Granular systems . . . . .	25
1.3 Organization of the chapters . . . . .	28
<b>2 Review of TvNS theory</b>	<b>31</b>
2.1 A historical note of the explosion problem . . . . .	31
2.2 Gas dynamics . . . . .	32
2.3 Shocks and boundary conditions . . . . .	34
2.4 TvNS solution . . . . .	36
2.5 Applications of TvNS theory . . . . .	43
<b>3 Computational Methods</b>	<b>47</b>
3.1 Time-Driven Molecular Dynamics Simulation . . . . .	47
3.2 Event-Driven Molecular Dynamics Simulation . . . . .	48
3.3 Numerical Method to solve the set of ODEs . . . . .	51

<b>4</b>	<b>Shock propagation following an intense explosion: Comparison between hydrodynamics and simulation</b>	<b>55</b>
4.1	Introduction . . . . .	55
4.2	Comparison with event-driven simulations . . . . .	58
4.3	Shock propagation in a hard sphere gas . . . . .	64
4.4	Local Equilibrium . . . . .	70
4.4.1	Equation of state . . . . .	71
4.4.2	Equipartition . . . . .	73
4.4.3	Skewness and Kurtosis . . . . .	75
4.5	Effect of heat conduction . . . . .	77
4.6	Sonic line . . . . .	79
4.7	Conclusion and discussion . . . . .	81
<b>5</b>	<b>Shock propagation following an intense explosion: Detailed comparison between hydrodynamics and simulation in two dimensions</b>	<b>85</b>
5.1	Introduction . . . . .	85
5.2	Simulation model and comparison with hydrodynamic solution in two dimensions . . . . .	86
5.2.1	TvNS solution in two dimensions . . . . .	87
5.2.2	Comparison with event-driven simulations . . . . .	88
5.3	Shock propagation in two dimensional elastic media . . . . .	94
5.4	Local Equilibrium . . . . .	100
5.4.1	Equation of state . . . . .	100
5.4.2	Equipartition . . . . .	101
5.4.3	Skewness and Kurtosis . . . . .	102
5.5	Conclusion and discussion . . . . .	104
<b>6</b>	<b>Shock propagation in locally driven granular systems</b>	<b>107</b>
6.1	Introduction . . . . .	107

6.2	Model . . . . .	108
6.3	Scaling Argument . . . . .	110
6.3.1	Conserved model . . . . .	111
6.3.2	Non-conserved model . . . . .	114
6.4	Numerical Results . . . . .	115
6.4.1	Elastic . . . . .	116
6.4.2	Inelastic . . . . .	119
6.5	Comparison with experiments . . . . .	121
6.6	Conclusion and discussion . . . . .	125
<b>7</b>	<b>Summary and outlook</b>	<b>127</b>
	<b>Bibliography</b>	<b>131</b>



# Synopsis

A system that is in thermal equilibrium or in a non-equilibrium steady state, when slightly perturbed, relaxes to its stationary state with time. For small perturbations, the relaxation may be studied within linear response theory. However, when the perturbation is strong, the system is taken far from the stationary state, and the response becomes difficult to study. A special class of a strong perturbation is one when the perturbation is localized in space, either as a single impact or continuous in time. When the perturbation is localized in space, then a shock wave may result if the flow velocity is much larger than the speed of sound in the medium. Such situations arise in many different physical phenomena. Examples include atomic explosion, supernova remnants, crater formation, viscous fingering, etc. In this thesis, we study shock propagation in both an elastic medium (dilute gas) and an inelastic medium (granular material).

## Shock propagation in a dilute gas

In an intense explosion, a large amount of energy is deposited at a point, which creates a shock wave that propagates radially outwards. The gas properties like density, velocity, pressure, and temperature inside the shock region vary continuously with radius, and have discontinuities at the shock front, which separates the disturbed region from the ambient gas at rest. The growth of the radius of the shock front  $R(t)$  may be found by simple dimensional analysis to be  $R(t) \sim t^{2/d+2}$  [1, 2, 3]. The dependence of the thermodynamic

quantities on radius was first studied, in the scaling limit, by Taylor, von Neumann, and Sedov and is known as the TvNS theory, and is one of the classic problems in gas dynamics. The mass, momentum, and energy are conserved locally so that the fluid flow is described by the corresponding continuity equations. Assumptions of local equilibrium, and absence of heat conduction further simplify the equations in the hydrodynamic limit. The assumption of local equilibrium implies that the flow is isentropic, and that the local temperature, pressure, and density are related through the equation of state of the gas, which in the TvNS theory is assumed to be that of the ideal gas. The values of the thermodynamic quantities behind the shock front are determined in terms of the corresponding values just ahead of the shock front through the Rankine-Hugoniot boundary conditions. With these assumptions it was possible to obtain an exact solution for the non-dimensionized scaling functions describing density, velocity, pressure, and temperature [1, 4, 2, 3, 5].

The radial growth described in TvNS theory has been verified experimentally in atomic explosion [4], cylindrically symmetric blast waves produced by focussing ultra fast laser pulses on gas jets [6], spherical blast waves produced by focussing laser beam on target pins [7], and in blast waves produced by focussing laser pulses with varying energy in a cluster media by using laser machining technique [8], etc. The radial growth has also been verified accurately in simulations of particle-based microscopic models [9, 10]. In addition, the TvNS theory has applications in the early stages of supernova remnants, formation of stars and galaxy.

There have been many studies that have generalized the TvNS theory by including the effects like radiation, heat conduction [11], viscous effect [12, 13] and implosions [14, 15, 16], etc. However, these were at the level of adding more terms to the hydrodynamic equations, and analyzing the resulting equations numerically. Surprisingly, there have been no simulation of particle-based microscopic models that check the validity of the TvNS theory. It has only been very recently that the predictions for the radial distribution



of density, flow velocity, and temperature fields in two dimensions have been compared with results from molecular dynamics simulations [17]. It was found that the simulations reproduce well the TvNS solution for low to medium densities, except for a small difference in the discontinuities at the shock front, and a slight discrepancy near the shock center. When the number density of the ambient gas is high, the TvNS solution was seen to not describe well the data near the shock front. However, the key assumptions of local equilibrium and the existence of an equation of state that are assumed in the TvNS solution were not tested in the simulations. Also, the simulation data was presented only for a single time, and thus it is not very clear whether the scaling limit has been reached. While these simulations were in two dimensions, there are no similar studies in three dimensions. Thus, it is not very clear where the TvNS solution is reproducible in microscopic models and which assumptions of the TvNS theory are actually valid.

In this thesis, we compare the TvNS results, for the scaling functions with the results from large scale event driven molecular dynamics simulations. We find that the TvNS solutions fail to describe the numerical data well in three dimensions. This is contrary to results from earlier molecular dynamics study in two dimensions [17]. In order to test the importance of spatial dimensions, we also compare TvNS solution in two dimensions with simulations in two dimensions. Consider a system of identical hard spheres which are initially at rest and uniformly distributed in space. The system is perturbed by an initial localized input of energy at the origin by giving kinetic energy to a few particle. The particles move ballistically until they undergo elastic, momentum conserving collisions with other particles. The initial perturbation creates a disturbance that propagates outwards in a radially symmetric fashion as shown in Fig 1. The conserved quantities in the model are density, momentum, and energy as in the TvNS theory. The main results obtained from simulations are briefly described below.

- We determine numerically the radial distribution of density, velocity, temperature, and pressure and show unambiguously that the TvNS theory fails to describe the

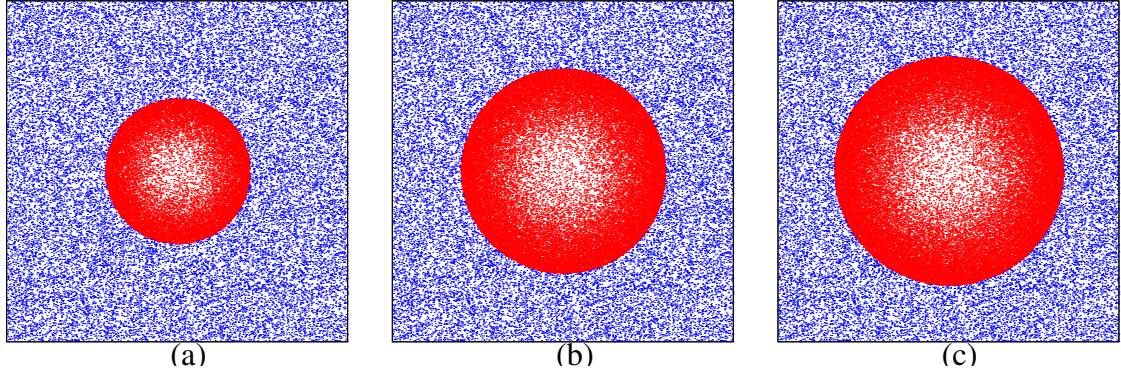


Figure 1: Snapshots of moving (red) and stationary (blue) particles following an impact near the center. Time increases from (a) to (c). All collisions are elastic and the simulations are in two dimensions.

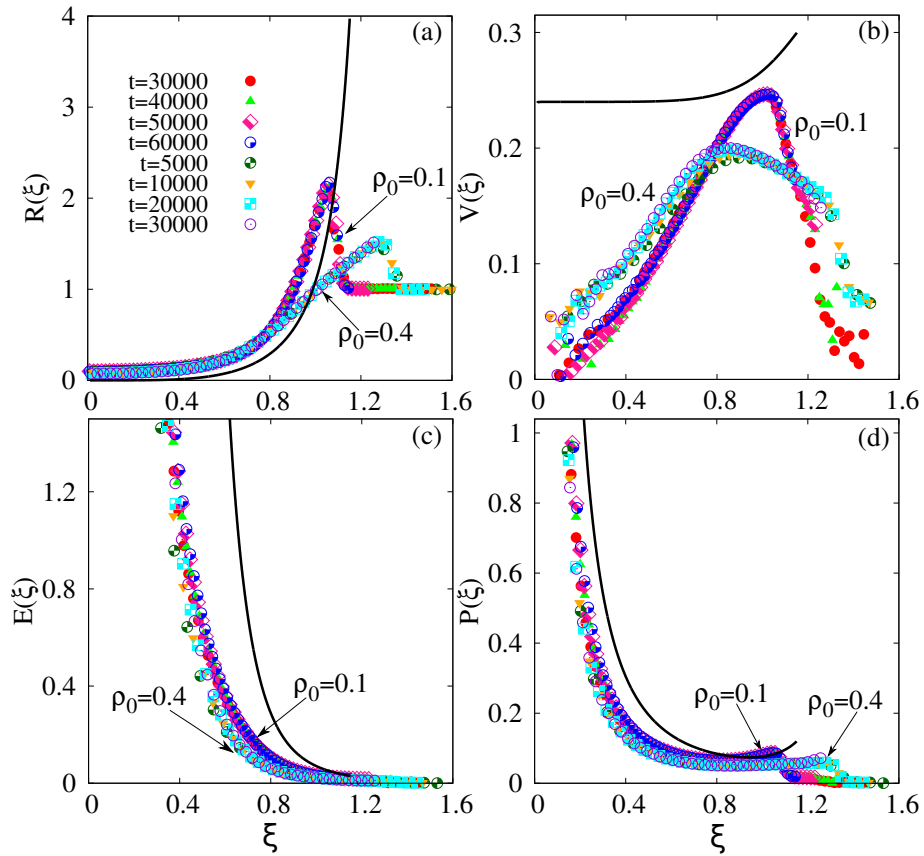


Figure 2: The variation of the scaling functions (a)  $R(\xi)$ , (b)  $V(\xi)$ , (c)  $E(\xi)$ , and (d)  $P(\xi)$  corresponding to non-dimensionalized density, velocity, temperature, and pressure with scaled distance  $\xi$  in three dimensions. The data are shown for 2 different initial densities  $\rho_0 = 0.1$  and  $0.4$ . The data correspond to different times as indicated in (a). The black solid lines correspond to the TvNS solution.

numerical data for most distances, ranging from the shock center to the shock front, both in two and three dimensions [see Figs 2 and 3].

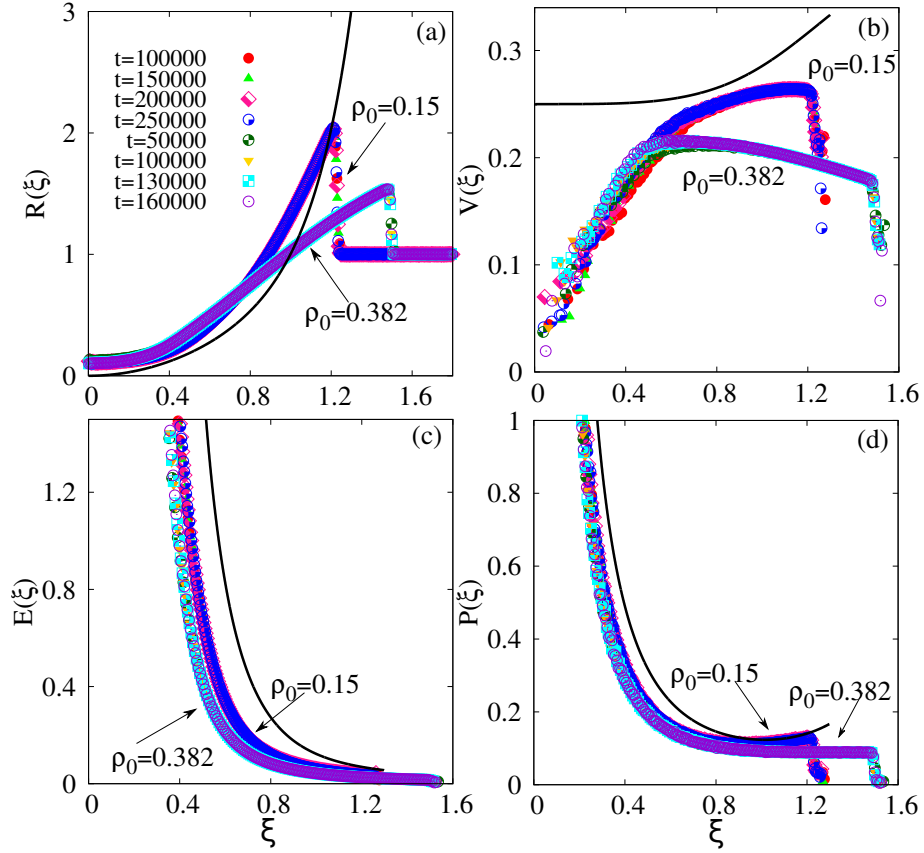


Figure 3: The variation of the scaling functions (a)  $R(\xi)$ , (b)  $V(\xi)$ , (c)  $E(\xi)$ , and (d)  $P(\xi)$  corresponding to non-dimensionalized density, velocity, temperature, and pressure with scaled distance  $\xi$  in two dimensions. The data are shown for 2 different initial densities  $\rho_0 = 0.15$  and  $0.382$ . The data correspond to different times as indicated in (a). The black solid lines correspond to the TvNS solution.

- We modify the TvNS theory to replace the constitutive relation of an ideal gas law to the virial equation of state (up to 10 terms) for a hard sphere gas. We show that while inclusion of the more realistic constitutive relation into the TvNS theory modifies the predictions for the scaling functions, especially near the shock front, they still fail to describe the data well in terms of the exponents characterizing the power law behavior near the shock center.
- By measuring pressure, temperature, and density independently, we show that, numerically, the virial equation of state is satisfied, justifying the key assumption of

TvNS theory of the existence of an equation of state.

- The energy is equipartitioned equally among the different degrees of freedom, as would be expected in a system in local equilibrium.
- We find that the distribution of the velocity fluctuations, in regions between the shock center and shock front, has non-gaussian tails. In particular, it is asymmetric with non-zero skewness and an exponential tail, showing that local thermal equilibrium is not reached. The lack of local equilibrium could be a possible reason for the TvNS theory to fail in three dimensions.
- The flow velocity is subsonic within the blast and supersonic when compared to the ambient gas into which the shock is expanding, as implicitly assumed in the TvNS solution.

## **Shock propagation in dilute granular gas**

Shocks can propagate in dilute inelastic gas also. The most common example of inelastic media is granular systems. Granular systems are ubiquitous in our daily life from microscopic scale to astrophysical scale including food grains, coffee beans, sand, steel balls, and planetary rings. The two important features associated with granular materials which make them unique are the irrelevance of the energy scale  $k_B T$  of temperature and the dissipative nature of interaction between particles. The dissipative nature of the interactions among the constituent particles can lead to diverse physical phenomena such as shock propagation, pattern formation, clustering instability, granular piles, jamming, segregation, stratification, shear flows, surface waves, fingering instability, and fluidization (see the reviews in [18, 19, 20]). A subclass of problems that have been of experimental and theoretical interest is the response of a granular system at rest to an external perturbation that is applied either as an instantaneous impulse or continuously in time.

One of the most commonly studied examples is the *globally perturbed* freely cooling granular gas, where homogeneously distributed macroscopic particles with random velocities move ballistically and dissipate energy through inelastic collisions, in the absence of external driving. Another interesting limit is the *locally perturbed* freely cooling granular gas, where initially all particles are at rest and kinetic energy is imparted to a few localized particles. The problem of atomic explosion is analogous to the second kind. In both cases discussed above, the perturbation was an impulse. One could also consider *continuous and locally perturbed* driven granular systems, where particles at rest are driven by a continuous injection of energy in a small domain. This scenario has been investigated in many recent experiments and includes pattern formation in granular material due to the injection of a gas [21, 22], grains [23], or fluid [24]. We study a simple model of spheres at rest that is driven at the origin by a continuous injection of particles from outside. From a combination of event-driven simulations and scaling arguments, we determine the exponents governing the growth of the disturbance. The results are compared with the data from two experiments [21, 22] and excellent agreement is obtained.

In this thesis, we consider a  $d$ -dimensional system of hard spheres. The particles move ballistically until they undergo inelastic, momentum-conserving binary collisions with other particles. Initially, all particles are at rest and uniformly distributed in space. The system is driven locally by a continuous input of energy restricted to a small region by injecting particles at a constant rate at the origin. The injected particles undergo their first collision with a particle in the system, after which the injected particles are removed from the system so that the total number of particles in the system is conserved. We also consider a nonconserved model in which the injected particles stay in the system, thereby increasing the total number of particles at a constant rate. It is observed that the scaling laws at large times are identical for both models, and we focus only on the model where total number of particles is conserved.

- When the energetic particles are injected from the center, particles upto a certain

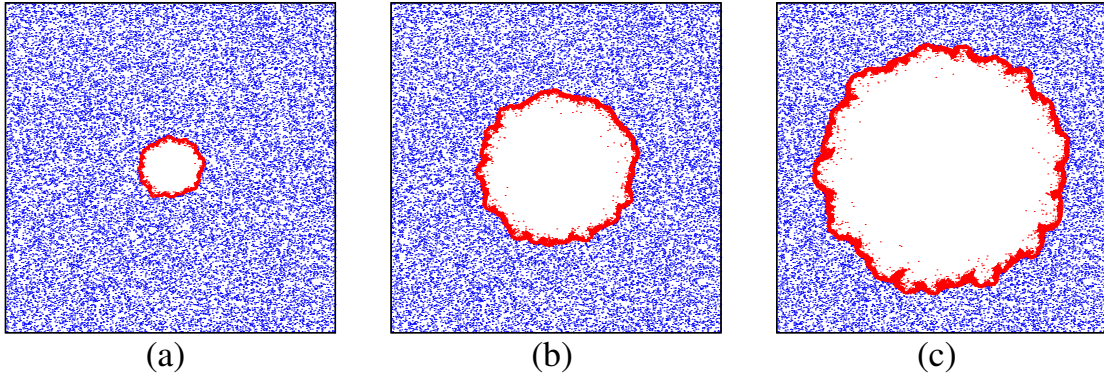


Figure 4: Snapshots of moving (red) and stationary (blue) particles following the continuous injection of particles at the center. Time increases from (a) to (c). All collisions are inelastic and the simulations are in two dimensions.

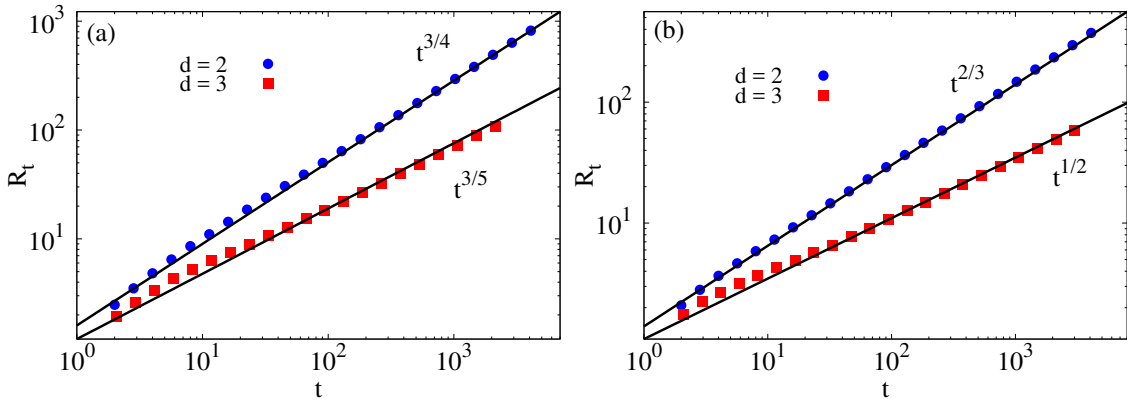


Figure 5: Simulation results for the temporal variation of radius  $R_t$  in two and three dimensions for (a) elastic system, and (b) inelastic system.

distance are disturbed, and the zone of disturbance propagates radially outward. In the case of the inelastic system, particles cluster together and form a dense band adjacent to the front of the disturbance, forming a vacant region around the center. The time evolution of the disturbance for an inelastic system is as shown in Fig 4. In contrast, in the elastic system, the circular region of moving particles has nonzero density everywhere.

- We assume a power-law growth for the radius of disturbance,  $R_t \sim t^\alpha$ . By identifying that energy grows linearly in the elastic system and radial momentum grows linearly in the inelastic system, the exponents governing the power-law growth of the radius of disturbance was obtained. From the scaling argument, we obtain  $\alpha = \frac{3}{d+2}$

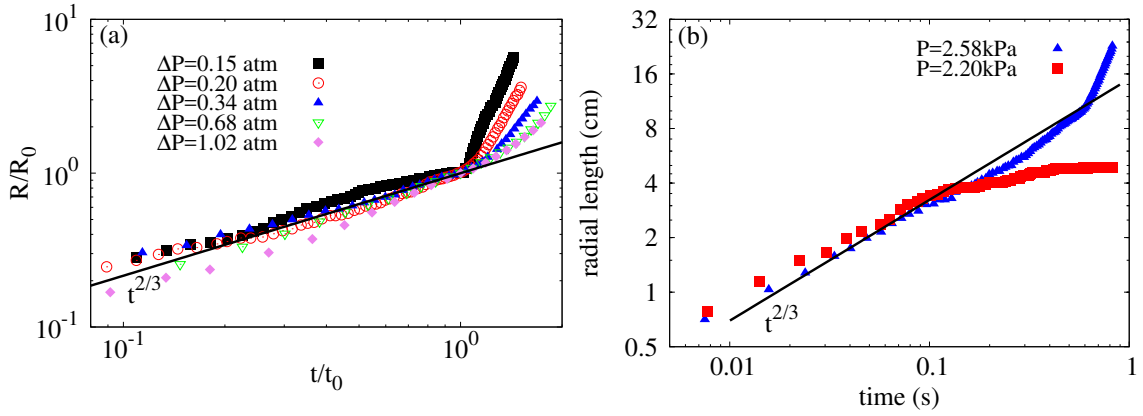


Figure 6: Experimental data taken from (a) Ref. [21] and (b) Ref. [22] for the growth of radial distance from the center.

for an elastic system and  $\alpha = \frac{2}{d+1}$  for an inelastic system, where  $d$  represents the spatial dimension.

- The simulation results match well the predictions for the power law growth for the radius of disturbance for elastic and inelastic systems both in two and three dimensions, as shown in Fig 5.
- We analyzed two experiments on pattern formation [21, 22] that arise due to the injection of a gas at localized point in a two-dimensional granular medium. The first experiment of interest is pattern formation in spherical glass beads that are distributed uniformly within a circular Hele-Shaw cell [21]. The beads, initially at rest, were perturbed by the continuous injection of pressurized nitrogen through a hole at the center of the bottom plate of the cell. When the driving pressure was high enough, the continuous perturbation led to the formation of a time-dependent growing viscous fingering pattern. We replot the published experimental data for scaled radius against scaled time as shown in Fig 6 (a). We also analyze data from a similar experiment with granular material confined in a circular Hele-Shaw cell with central air injection [22] and the radial growth is as shown in Fig 6 (b). When the injection pressure is sufficient enough, the particles in the system move out by forming a central (roughly circular) region devoid of particles. Around this central region, there is a zone where the granular material is compacted. In both the case,

experimentally obtained radial growth of the pattern was shown to be consistent with our simulation results by obeying the same power-law.



# List of Figures

1	Snapshots of moving (red) and stationary (blue) particles following an impact near the center. Time increases from (a) to (c). All collisions are elastic and the simulations are in two dimensions. . . . .	4
2	The variation of the scaling functions (a) $R(\xi)$ , (b) $V(\xi)$ , (c) $E(\xi)$ , and (d) $P(\xi)$ corresponding to non-dimensionalized density, velocity, temperature, and pressure with scaled distance $\xi$ in three dimensions. The data are shown for 2 different initial densities $\rho_0 = 0.1$ and 0.4. The data correspond to different times as indicated in (a). The black solid lines correspond to the TvNS solution. . . . .	4
3	The variation of the scaling functions (a) $R(\xi)$ , (b) $V(\xi)$ , (c) $E(\xi)$ , and (d) $P(\xi)$ corresponding to non-dimensionalized density, velocity, temperature, and pressure with scaled distance $\xi$ in two dimensions. The data are shown for 2 different initial densities $\rho_0 = 0.15$ and 0.382. The data correspond to different times as indicated in (a). The black solid lines correspond to the TvNS solution. . . . .	5
4	Snapshots of moving (red) and stationary (blue) particles following the continuous injection of particles at the center. Time increases from (a) to (c). All collisions are inelastic and the simulations are in two dimensions.	8
5	Simulation results for the temporal variation of radius $R_t$ in two and three dimensions for (a) elastic system, and (b) inelastic system. . . . .	8
6	Experimental data taken from (a) Ref. [21] and (b) Ref. [22] for the growth of radial distance from the center. . . . .	9

2.1	Schematic representation of normal shock to obtain the shock relations from the mass, momentum, and energy fluxes. The quantities $v_0$ , $p_0$ , $\rho_0$ , and $w_0$ are the velocity, pressure, density, and enthalpy ahead of the shock and the corresponding quantities with the subscript $f$ are those behind the shock. . . . .	35
2.2	The velocity, density, and pressure distributions inside the blast wave for $\gamma = 7/5$ . . . . .	43
2.3	The velocity, density, and pressure distributions inside the blast wave for a monoatomic gas with $\gamma = 5/3$ . . . . .	44
3.1	Schematic representation of the procedure to solve the equations numerically . . . . .	53
3.2	The scaling functions $R(\xi)$ , $V(\xi)$ , and $P(\xi)$ corresponding to density, velocity, and pressure respectively are plotted as a function of the scaled distance. The data are obtained by solving Eqs. (3.12) numerically for $\gamma = 5/3$ . . . . .	54
4.1	(a) The variation of the scaling function $R(\xi)$ corresponding to non-dimensionalized density [see Eq. (4.2)] with scaled distance $\xi$ . The data are shown for 2 different initial densities $\rho_0 = 0.1$ and $0.4$ . For $\rho_0 = 0.1$ , the different times are $t = 30000, 40000, 50000, 60000$ , and for $\rho = 0.4$ , $t = 5000, 10000, 20000, 30000$ , as indicated in (a). The black solid lines correspond to the TvNS solution [see Eqs. (2.36)-(2.38)]. (b) The data for $R$ are shown in logarithmic scale to emphasize the power-law divergence for small $\xi$ . . . . .	60

4.2 (a) The variation of the scaling function  $V(\xi)$  corresponding to non-dimensionalized velocity [see Eq. (4.2)] with scaled distance  $\xi$ . The data are shown for 2 different initial densities  $\rho_0 = 0.1$  and  $0.4$ . For  $\rho_0 = 0.1$ , the different times are  $t = 30000, 40000, 50000, 60000$ , and for  $\rho = 0.4$ ,  $t = 5000, 10000, 20000, 30000$ , as indicated in Fig. 4.1(a). The black solid lines correspond to the TvNS solution [see Eqs. (2.36)-(2.38)]. . . . . 61

4.3 (a) The variation of the scaling function  $E(\xi)$  corresponding to non-dimensionalized temperature [see Eq. (4.2)] with scaled distance  $\xi$ . The data are shown for 2 different initial densities  $\rho_0 = 0.1$  and  $0.4$ . For  $\rho_0 = 0.1$ , the different times are  $t = 30000, 40000, 50000, 60000$ , and for  $\rho = 0.4$ ,  $t = 5000, 10000, 20000, 30000$ , as indicated in Fig. 4.1(a). The black solid lines correspond to the TvNS solution [see Eqs. (2.36)-(2.38) and Eq. (4.4)]. The black solid lines correspond to the TvNS solution. (b) The data for  $E$  are shown in logarithmic scale to emphasize the power-law divergence for small  $\xi$ . . . . . 62

4.4 (a) The variation of the scaling function  $P(\xi)$  corresponding to non-dimensionalized pressure [see Eq. (4.2)] with scaled distance  $\xi$ . The data are shown for 2 different initial densities  $\rho_0 = 0.1$  and  $0.4$ . For  $\rho_0 = 0.1$ , the different times are  $t = 30000, 40000, 50000, 60000$ , and for  $\rho = 0.4$ ,  $t = 5000, 10000, 20000, 30000$ , as indicated in (a). The black solid lines correspond to the TvNS solution [see Eqs. (2.36)-(2.38)]. (b) The data for  $P$  are shown in logarithmic scale to emphasize the power-law divergence for small  $\xi$ . . . . . 63

- 4.5 The scaling functions (a)  $R(\xi)$ , (b)  $V(\xi)$ , (c)  $E(\xi)$ , and (d)  $P(\xi)$  corresponding to density, velocity, temperature and pressure respectively versus  $\xi$  for ambient density  $\rho_0 = 0.1$  is compared with the theoretical solution for the hydrodynamic equations with virial EOS for the hard sphere gas. The simulation data (represented by points) correspond to four different times with keys as shown in Fig 4.1(a). The lines represent the virial EOS solution with the virial expansion truncated at  $n = 2, 4, 6, 8, 10$ . Black solid curve represents the case of ideal gas. The inset shows the plots on a log-log scale, accentuating the small  $\xi$  behavior. . . . . 68
- 4.6 The scaling functions (a)  $R(\xi)$ , (b)  $V(\xi)$ , (c)  $E(\xi)$ , and (d)  $P(\xi)$  corresponding to density, velocity, temperature and pressure respectively versus  $\xi$  for ambient density  $\rho_0 = 0.4$  is compared with the theoretical solution for the hydrodynamic equations with virial EOS for the hard sphere gas. The simulation data (represented by points) correspond to four different times with keys as shown in Fig 4.1(a). The lines represent the virial EOS solution with the virial expansion truncated at  $n = 2, 4, 6, 8, 10$ . Black solid curve represents the case of ideal gas. The inset shows the plots on a log-log scale, accentuating the small  $\xi$  behavior. . . . . 69
- 4.7 The scaling functions corresponding to density, velocity, temperature, and pressure at the shock front, denoted by (a)  $R(\xi_f)$ , (b)  $V(\xi_f)$ , (c)  $E(\xi_f)$ , and (d)  $P(\xi_f)$  respectively, versus the ambient density  $\rho_0$ . The data are for the virial EOS solution with the virial expansion truncated at  $n = 2, 4, 6, 8, 10$ . 70
- 4.8 The variation of  $\chi(n)$  [see Eq. (4.18)] with  $\xi$  for  $n = 2, 4, 6, 8, 10$ . The data in (a) are for times 40000 and 60000 with ambient number density  $\rho_0 = 0.1$  and in (b) are for times 10000 and 30000 with ambient number density  $\rho_0 = 0.4$ . For large  $n$ ,  $\chi(n)$  fluctuates about 1 in both the case. . . 72

4.9	The variation of $\chi(10)$ with $\xi$ , where the temperature in Eq. (4.18) is replaced by $T_r$ or $T_\perp$ defined through the radial and perpendicular components of the velocity fluctuations. The data are for times 40000 and 60000 and ambient density $\rho_0 = 0.1$ . . . . .	73
4.10	The variation of $\zeta$ , the ratio of energies in the radial and $\theta$ - $\phi$ directions [see Eq. (4.23)] with the scaled distance $\xi$ . The data is for four different times with keys as in Fig 4.1(a), for two ambient densities $\rho_0 = 0.1$ and 0.4. Away from the shock front, $\zeta \approx 1$ . . . . .	74
4.11	The variation with scaled distance $\xi$ of (a) the kurtosis $\kappa_r$ for the radial velocity fluctuations [see Eq. (4.24)]. (b) the kurtosis $\kappa_\perp$ for the velocity fluctuations in the $\theta$ - $\phi$ direction [see Eq. (4.25)] and (c) skewness $S$ for the radial velocity fluctuations [see Eq. (4.26)]. The black solid line in (a) and (b) are reference lines of 1, corresponding to gaussianity. The data are for $\rho_0 = 0.1$ and $\rho_0 = 0.4$ and for four different times with keys as in Fig 4.1(a). (d) The distribution of the radial velocity fluctuations $P(\delta v)$ measured at $r = 61.5$ , $t = 30000$ and $\rho_0 = 0.4$ , corresponding to $\xi = 0.58$ . The black solid curve represents the gaussian distribution fitted to the data near zero. The blue solid line is an exponential and a guide to the eye. . . . .	76
4.12	The parametric plot of sound velocity(C)-flow velocity(V). The data are from simulations. The solid reference line represents the sonic line [see Eq. (4.37)]. The arrows indicate the direction of increasing $\xi$ . (a) The full data. (b) Reduced data, where the data beyond the shock front have been removed. The data are for four different times with keys as in Fig 4.1(a). . . . .	80
4.13	The parametric plot of sound velocity(C)-flow velocity(V). The data are from TvNS solution with virial EOS truncated at the tenth virial coefficient. The solid reference line represents the sonic line [see Eq. (4.37)]. The arrows indicate the direction of increasing $\xi$ . . . . .	81

5.1	Moving (red) and stationary (blue) particles at times (a) $t = 100000$ , (b) $t = 150000$ , (c) $t = 200000$ and (d) $t = 250000$ . Energetic particles are injected at the center. All collisions are elastic with $r = 1$ . The data are for the ambient density $\rho_0 = 0.15$ . . . . .	89
5.2	The variation of the scaling functions (a) $R(\xi)$ , (b) $V(\xi)$ , (c) $E(\xi)$ and (d) $P(\xi)$ corresponding to non-dimensionalized density, velocity, temperature and pressure [see Eq. (2.32)] with scaled distance $\xi$ . The data are shown for 2 different initial densities $\rho_0 = 0.15$ and $0.382$ . For $\rho_0 = 0.15$ , the different times are $t = 100000, 150000, 200000, 250000$ , and for $\rho = 0.382, t = 50000, 100000, 130000, 160000$ , as indicated in (a). The black solid lines correspond to the TvNS solution [see Eqs. (2.36)-(2.38) and Eq. (4.4)]. The data for $R, P$ , and $E$ are also shown on a logarithmic scale in Fig. 5.3. . . . .	91
5.3	The data in Fig. 5.2(a), (c) and (d) are shown in logarithmic scale to emphasize the power-law divergence for small $\xi$ . The three plots show the variation of the scaling functions (a) $R(\xi)$ , (b) $E(\xi)$ and (c) $P(\xi)$ with scaled distance $\xi$ . The data are for 2 different initial densities $\rho_0 = 0.15$ and $0.382$ . Each density has data for four different times and the symbols are same as described in Fig 5.2 (a). The black solid lines correspond to the TvNS solution. . . . .	92
5.4	The virial equation of state truncated at $n = 10$ and the Henderson relation are plotted. It is observed that both the curve match well. . . . .	94

- 5.5 The scaling functions (a)  $R(\xi)$ , (b)  $V(\xi)$ , (c)  $E(\xi)$ , and (d)  $P(\xi)$  corresponding to density, velocity, temperature and pressure respectively versus  $\xi$  for ambient density  $\rho_0 = 0.15$  is compared with the theoretical solution for the hydrodynamic equations with virial EOS for the hard sphere gas. The simulation data (represented by points) correspond to four different times with keys as shown in Fig 5.2(a). The lines represent the virial EOS solution with the virial expansion truncated at  $n = 2, 4, 6, 8, 10$ . Black solid curve represents the case of ideal gas. The inset shows the plots on a log-log scale, accentuating the small  $\xi$  behavior. . . . . 98
- 5.6 The scaling functions (a)  $R(\xi)$ , (b)  $V(\xi)$ , (c)  $E(\xi)$ , and (d)  $P(\xi)$  corresponding to density, velocity, temperature and pressure respectively versus  $\xi$  for ambient density  $\rho_0 = 0.382$  is compared with the theoretical solution for the hydrodynamic equations with virial EOS for the hard sphere gas. The simulation data (represented by points) correspond to four different times with keys as shown in Fig 5.2(a). The lines represent the virial EOS solution with the virial expansion truncated at  $n = 2, 4, 6, 8, 10$ . Black solid curve represents the case of ideal gas. The inset shows the plots on a log-log scale, accentuating the small  $\xi$  behavior. . . . . 99
- 5.7 The variation of  $\chi(n)$  [see Eq. (5.17)] with  $\xi$  for  $n = 2, 4, 6, 8, 10$ . The data are for times 150000 and 250000 and for ambient number density  $\rho_0 = 0.15$ . For large  $n$ ,  $\chi(n)$  fluctuates about 1. . . . . 101
- 5.8 The variation of  $\zeta$ , the ratio of energies in the radial and transverse directions [see Eq. (5.18)] with the scaled distance  $\xi$ . The data is for four different times with keys as in Fig 5.2(a), for two ambient densities  $\rho_0 = 0.15$  and 0.382. Away from the shock front,  $\zeta \approx 1$ . . . . . 102

5.9	The variation with scaled distance $\xi$ of (a) the kurtosis $\kappa_r$ for the radial velocity fluctuations. (b) the kurtosis $\kappa_\perp$ for the velocity fluctuations in the $\theta$ direction and (c) skewness $S$ for the radial velocity fluctuations. The data are for $\rho_0 = 0.15$ and $\rho_0 = 0.382$ and for four different times with keys as in Fig 5.2(a). (d) The distribution of the radial velocity fluctuations $P(\delta v)$ measured at $r = 462.5$ , $t = 250000$ and $\rho_0 = 0.15$ , corresponding to $\xi = 0.41$ . The black solid curve represents the gaussian distribution fitted to the data near zero. . . . .	103
6.1	Moving (red) and stationary (blue) particles at times (a) $t = 500$ , (b) $t = 1000$ , (c) $t = 1500$ and (d) $t = 2000$ . Energetic particles are injected at the center. All collisions are elastic with $r = 1$ . The data are for the conserved model. . . . .	112
6.2	Moving (red) and stationary (blue) particles at times (a) $t = 1000$ , (b) $t = 2000$ , (c) $t = 4000$ and (d) $t = 8000$ . Energetic particles are injected at the center. All collisions are inelastic with $r = 0.1$ . The data are for the conserved model. . . . .	113
6.3	Radial momentum as a function of time $t$ for two and three-dimensional inelastic systems, showing a linear increase. The inset shows the data on a log-log scale, which show an initial transient regime before the linear growth is attained. The data are for the conserved model. . . . .	115
6.4	Simulation results for the elastic system ( $r = 1$ ) for the temporal variation of (a) radius $R_t$ , (b) kinetic energy $E_t$ , and (c) number of moving particles $N_t$ in two and three dimensions. The solid lines are power laws with exponents as predicted by the scaling arguments presented in the text. The data are for the conserved model. . . . .	117



6.5	Scaled radial distribution functions against scaled distances $r/t^\alpha$ for the elastic gas: (a) $\rho(r, t)$ , (c) $v(r, t)$ , (e) $e(r, t)$ , and (g) $\langle \cos \theta(r, t) \rangle$ in two dimensions and (b), (d), (f), and (h) corresponding quantities in three dimensions. Here $\alpha = 3/(d + 2)$ , as in Eq. (6.4), and $\beta = 2(1 - \alpha)$ . The data are for the conserved model. . . . .	118
6.6	Simulation results for the inelastic system ( $r = 0.1$ ) for the temporal variation of (a) radius $R_t$ , (b) kinetic energy $E_t$ , and (c) number of moving particles $N_t$ in two and three dimensions. The solid lines are power laws with exponents as predicted by the scaling arguments presented in the text. The data are for the conserved model. . . . .	120
6.7	Scaled radial distribution functions against scaled distances $r/t^\alpha$ for the inelastic gas: (a) $\rho(r, t)$ , (c) $v(r, t)$ , (e) $e(r, t)$ , and (g) $\langle \cos \theta(r, t) \rangle$ in two dimensions and (b), (d), (f), and (h) corresponding quantities in three dimensions. Here $\alpha = 2/(d + 1)$ , as in Eq. (6.5), and $\beta = 2(1 - \alpha)$ . The data are for the conserved model. . . . .	122
6.8	Experimental data (taken from Ref. [21]) for the scaled radius $R$ of the longest finger from the center, as a function of normalized time $t/t_0$ . Here $R_0 = R(t_0)$ . The data have been plotted for different gas overpressures. The solid lines are power laws $t^{1/2}$ , $t^{2/3}$ , and $t^1$ and are shown for reference.	123
6.9	Experimental data (taken from Ref. [22]) for the growth of maximum radial coordinate of the central zone of disturbance with time for two different values of injection pressures. The solid lines are power laws $t^{1/2}$ , $t^{2/3}$ , and $t^1$ and are shown for reference. . . . .	124

# List of Tables

4.1	The values of the virial coefficients $B_n$ for the hard sphere gas in three dimensions. The data are taken from Ref. [71]. . . . .	66
5.1	The values of the virial coefficients $B_n$ for the hard sphere gas in two dimensions. The data are taken from Ref. [71]. . . . .	96

# Chapter 1

## Introduction

Thermodynamic systems may be in equilibrium or out of equilibrium. A system is in equilibrium if the macroscopic properties of the system do not change with time, and there are no currents in the system. There is a well developed frame work for calculating expectation value of observables in equilibrium: a configuration  $C$  occurs with probability proportional to  $e^{-\beta E(C)}$ , where  $\beta = 1/k_B T$ ,  $T$  is the absolute temperature, and  $E(C)$  is the energy of the configuration.

The study of non-equilibrium systems is one of the developing and fascinating areas in current science. A comprehensive theory for describing systems far from equilibrium is still lacking, though almost all systems around us, ranging from nanoscale to astrophysical scale, are far from equilibrium. Some of them include powders, colloids, granular systems, astrophysical systems, and biological systems. These systems show many complex phenomena like pattern formation, clustering, shock propagation, avalanche, stratification, chaos, turbulence, earthquake, etc.

When a system in equilibrium is perturbed slightly, it relaxes to its stationary state with time. For small perturbations, the relaxation of such systems can be studied within linear response theory. When the perturbation is strong, the system is taken far from equilibrium and it is difficult to predict the response of such a system. A special case of a strong

perturbation is a localized perturbation, either as a single impact or continuous in time. When the perturbation is localized in space, then a shock wave may result if the flow velocity is much larger than the speed of sound in the medium. Such situations arise in many different physical situations, both in elastic and inelastic media. Some of the examples of shock waves include those during an atomic explosion, the shock wave generated during when aircraft break the speed of sound, bullet bow shock waves created when a bullet is fired from a rifle, and the wakes of a fast-moving boat. Astrophysical shocks, created by supernovae, are one of the major energy sources in the interstellar medium. The propagation of shocks in elastic and inelastic media is the subject matter of this thesis.

## 1.1 Shock propagation in dilute elastic gas

In an intense explosion, a large amount of energy is deposited at a point, which creates a shock wave that propagates radially outwards. The growth of the radius of the shock front  $R(t)$  may be found by simple dimensional analysis to be  $R(t) \sim t^{2/(d+2)}$  [1, 2, 3]. Inside the blast wave, the gas properties like density, temperature, and pressure vary continuously with a discontinuity at the shock front, the layer which separates the disturbed region from the ambient gas at rest. The dependence of these thermodynamic quantities on radius was first studied, in the scaling limit, by Taylor, von Neumann, and Sedov [1, 4, 2, 3, 5], and will be referred to in the remainder of the thesis as TvNS theory, which is one of the classic problems in gas dynamics. In the case of strong shocks, the perturbed matter moves faster than the rate at which energy is transferred through heat or sound modes, and the expansion of the gas is self-similar in time.

The scaling law for  $R(t)$  was first verified, to a high degree of accuracy, in the Trinity nuclear explosion of 1945 [1, 4], later on in the intermediate time evolution of supernova remnants [3, 25, 26, 27], and in laboratory experiments of laser-driven blast waves in gas jets [6], plasma [7], or cluster media [8]. Experimental studies and applications for the

evolution of astrophysical systems like supernova explosion are summarized in Ref. [28, 29]. The radial growth has also been verified accurately in simulations of particle-based microscopic models [9, 10].

In a very intense blast wave in the air, such as a nuclear explosion, more complicated phenomena than that described by hydrodynamics are also observed. Due to the extremely large temperatures that are generated, initially, energy is transported mostly as radiation. The air atoms are ionized resulting in varying adiabatic index. As the gas cools, radiation becomes less important, and the transport of energy is dominated by the shock wave. It is this intermediate regime that is described by hydrodynamics, and where the TvNS theory is applicable. We note that in our simulations of hard spheres, only this intermediate hydrodynamic regime can be studied.

TvNS theory is valid in the hydrodynamic limit. The conserved quantities in the problem are mass, momentum, and energy. Their evolution is described by the corresponding continuity equations. Within the assumption of negligible viscous effects and heat conduction, the flow becomes isentropic. Further assumption of the existence of local thermal equilibrium means that the density, pressure, and temperature are not independent, but are related through an equation of state. In the TVNS theory, the equation of state is taken to be the ideal gas law. The theory gives the solution for the radial distribution of pressure, density, temperature, and flow velocity fields in a blast wave propagating through a medium at rest, following an intense explosion, starting from hydrodynamic equations. Other generalizations of TvNS theory include the effect of including heat conduction [11, 30, 31], viscous effect [12, 32, 33, 13], radiation [11], instability [34], and implosions [14, 15, 35, 36, 37, 16].

The TvNS theory is also applicable to related problems. In some physical systems, there is a continuous input of energy in a localized region. The TvNS theory has been extended to describe such cases both analytically [38] as well as numerically [39] and is relevant for the early stage of supernova explosions, powerful wind from stars and hidden neutrino

sources [40], and for interstellar bubbles [41, 42]. The TvNS theory is also of interest in understanding the response of inelastic systems to localized perturbations, either as an impact or continuous in time. The conservation laws for such systems are fewer in number, as energy is not conserved, and the TvNS theory has recently been generalized to include dissipative interactions [43, 17].

Even though the hydrodynamic equations and their modifications have been studied, surprisingly, there has been little or no verification of the theory and its assumptions using simulations of particle-based microscopic models. In the first part of this thesis, we compare the results and assumptions of the hydrodynamic theory with results from large scale event-driven molecular dynamics simulations of a hard sphere gas in three dimensions. We unambiguously show that the TvNS solutions do not match with the data obtained from simulation. Then we check assumptions made in the theory within the simulation. First, we replace the ideal gas equation of state with the more general virial equation of state and compare the results from the hydrodynamic theory with that obtained by simulation. The adoption of the virial equation of state improves the predictions, however it still does not describe the data well. We also check the existence of local thermal equilibrium by measuring the equipartition of energy, kurtosis, and skewness. We find that the probability distribution of velocity fluctuation deviates from Gaussian. But, we find numerically that the key assumption of the existence of an equation of state of the gas is valid.

In contrast to our results for the scaling functions in three dimensions, recent simulations in Ref. [17] performed in two dimensions found that the TvNS solution described the results from simulations quite well in most of the region, except a slight discrepancy near the shock center. To resolve this contradiction, we perform large scale simulations in two dimensions and compare the results with the TvNS solutions in two dimensions. We show that, like in three dimensions, the TvNS solution does not match well with the simulation data in almost the entire region.

## 1.2 Shock propagation in dilute inelastic gas

One of the most common examples of inelastic media is granular systems.

### 1.2.1 Granular systems

A granular system is a collection of macroscopic particles. The interaction between the particles is mainly on contact and through friction and collision. Granular materials are ubiquitous in our daily lives. Examples include sugar, coffee beans, salt, rice grains, sand, rocks, etc. In astrophysical systems, granular materials show their presence in the form of Saturn rings, planetary rings, granular asteroids, etc. The study of granular systems is important because of their wide range of applications. Examples include agriculture and food processing industry where seeds, grains, and food materials are transported and manipulated, the pharmaceutical industry in which processing and handling of medicines, glass industry, and construction-related industry (civil engineering). They play a major role in Earth science, for example, geological processes such as sand dunes, landslides, erosion, pyroclastic flow, and underwater gravity currents determine the morphology of Earth.

The prediction of the macroscopic behavior of granular systems, starting from microscopic interactions is not easy. The unique properties of granular materials are mainly due to two important aspects. One is that the temperature does not play a role. To understand this, consider a typical sand grain of mass,  $m = 1\text{mg}$  kept at a distance of its diameter  $d = 1\text{mm}$  above the ground. The thermal energy at room temperature  $T = 300\text{K}$  is,  $E_{th} = k_B T \sim 10^{-21}\text{J}$ , where  $k_B \sim 10^{-23}\text{JK}^{-1}$ . The corresponding potential energy  $E_p = mgd \sim 10^{-6}10^1 10^{-3}\text{J} \sim 10^{-8}\text{J}$ . So, the thermal energy is insignificant as compared to the gravitational potential energy. Likewise, for a typical velocity of  $1\text{cm/sec}$ , the kinetic energy of a granular particle,  $E_K \sim mv^2 \sim 10^{-6}10^{-4}\text{J} \sim 10^{-10}\text{J}$ , which strengthens the irrelevance of temperature. Since the thermal fluctuations are insignificant, granu-

lar systems can not explore the phase space and exhibit multiple metastable steady-state, which are far from equilibrium and will last indefinitely unless they gain energy from an external perturbation.

The second property that is characteristic of granular material is the dissipative interaction between particles. The binary collisions between particles are inelastic which lead to dissipation. In particular, depending on the way it is handled, a granular material can behave like a solid, a liquid or a gas or we can consider the state of granular media is a different one from the usual state of matter and the different flow regimes can also coexist in a single configuration. From a theoretical perspective, granular physics represents an attractive intersection of fluid dynamics, non-equilibrium statistical mechanics, and the theory of pattern formation.

The dissipative nature of the interactions among the constituent particles can lead to diverse physical phenomena such as shock propagation, pattern formation, clustering instability, granular piles, jamming, segregation, stratification, shear flows, surface waves, fingering instability, and fluidization (see the reviews in [18, 19, 20]). There is no unified theory to describe granular matter. A subclass of problems that have been of experimental and theoretical interest is the response of a granular system at rest to an external perturbation that is applied either as an instantaneous impulse or continuously in time.

One of the most commonly studied examples is the globally perturbed freely cooling granular gas, where homogeneously distributed macroscopic particles with random velocities move ballistically and dissipate energy through inelastic collisions, in the absence of external driving. The homogeneity in the initial stage is unstable because of dissipation, and the system evolves to inhomogeneous regime containing clusters. This regime is mostly studied in simulations. Here the perturbation is the energy that is initially given. In the early stage of evolution, when the system is spatially homogeneous, the kinetic energy of the system  $E(t)$  decays with time  $t$  as  $t^{-2}$  (Haff's law) [44] in all dimensions. At later times, due to inelastic collisions, the system becomes spatially in-



homogeneous [45, 46] and energy decreases as  $t^{-\theta_d}$ , where  $\theta_d$  is less than 2 and depends on dimension  $d$  [47, 48, 49, 50, 51, 52, 53, 54, 55, 56]. Haff's law for the homogeneous regime has been confirmed in experiments [57, 58], while  $\theta_d$  characterizing the inhomogeneous regime has still not been observed in any experiment.

A different limit is the locally perturbed freely cooling granular gas, where initially all particles are at rest and kinetic energy is imparted to a few localized particles. Due to collisions, the disturbance grows radially outward, with a shock front separating the moving particles from the stationary ones. The elastic version of this problem is analogous to the problem of an intense explosion, mentioned in Sec. 1.1. In an inelastic system, the disturbance is concentrated in dense bands that moves radially outward. Examples of such systems include crater formation in a granular bed following an impact of an object or a continuous jet [59, 60, 61], shock propagation in a granular medium following a sudden impact [62, 63]. The shock propagation in granular systems following a sudden localized impact has been studied in simulations [10, 64]. The relevant exponents of radial growth may be obtained through scaling arguments based on the conservation of radial momentum [10, 64] and is verified in simulations. The exponents obtained thus may be used to describe [64] experiments on shock propagation in flowing glass beads that are perturbed by the impact of steel balls [62]. The variation of physical quantities inside the dense band may be obtained through a hydrodynamic description [43, 17].

In both cases discussed above, the perturbation was an impulse. One could also consider continuous and locally perturbed driven granular systems, where particles at rest are driven by a continuous injection of energy in a small domain. This scenario has been investigated in many recent experiments and includes viscous fingering [65] and pattern formation in granular material due to the injection of a gas [21, 22], grains [23], or fluid [24]. In the second part of this thesis, we study a particle-based model that determines the exponents for such situations. These predictions are compared with the results of two experiments and is shown to be in good agreement.

## 1.3 Organization of the chapters

The remainder of the thesis is organized as follows.

In **Chapter 2**, we review the TvNS solution of the atomic explosion problem using hydrodynamics.

**Chapter 3** describes the computational methods used in the thesis. These include event-driven simulations and the numerical algorithm to solve the ODEs in the hydrodynamic description of the shocks in elastic media.

The remaining chapters contain the original work of the thesis.

In **Chapter 4**, we compare the solution of the atomic explosion in the hydrodynamic limit, with the results from large scale event-driven molecular dynamics simulations of a hard sphere gas in three dimensions. We find that the predictions for the radial distribution of the thermodynamic quantities do not match well with the numerical data. We improve the theory by replacing the ideal gas law with a more realistic virial equation of state for the hard sphere gas. While this improves the theoretical predictions, we show that they still fail to describe the data well. To understand the reasons for this discrepancy, the different assumptions of the hydrodynamic theory are tested within the simulations. A key assumption of the theory is the existence of a local equation of state. We validate this assumption by showing that the local pressure, temperature, and density obey the equation of state for a hard sphere gas. However, the probability distribution of the velocity fluctuations has non-gaussian tails, especially away from the shock front, showing that the assumption of local equilibrium is violated. This, along with neglect of heat conduction, could be the possible reasons for the mismatch between theory and simulations.

It has only been very recently that the predictions for the radial distributions of density, flow velocity, and temperature fields in two dimensions have been compared with results from molecular dynamics simulations [17]. It was found that the simulations reproduce

well the TvNS solution for low to medium densities, in most of the regions. This result is contrary to our results in three dimensions. In **chapter 5**, we compare the TvNS results in two dimensions with the results from simulations in two dimensions through large scale event-driven simulations. We find that the TvNS results do not match with the simulation results in two dimensions too.

In **chapter 6**, we study shock propagation in a system of initially stationary hard spheres that is driven by a continuous injection of particles at the origin. The disturbance created by the injection of energy spreads radially outward through collisions between particles. Using scaling arguments, we determine the exponent characterizing the power-law growth of this disturbance in all dimensions. The scaling functions describing the various physical quantities are determined using large scale event-driven simulations in two and three dimensions for both elastic and inelastic systems. The results are shown to describe well the data from two different experiments on granular systems that are similarly driven.



# Chapter 2

## Review of TvNS theory

In this chapter, we review the TvNS theory for the propagation of shock following an intense, isotropic, localized explosion.

### 2.1 A historical note of the explosion problem

In the early 1940s, the Civil Defence Research Committee of the Ministry of Home Security told Taylor that it might be possible to produce a bomb in which a very large amount of energy would be released by nuclear fission. His first attempt was to get an idea of mechanical effects produced by the sudden release of a large amount of gas in a common explosion. He first considered the ideal problem of the sudden release of energy in an infinitely concentrated form. He then used the similarity assumption for an expanding blast wave in a conservative system, where the total energy is constant, starting from the equation which indicates the radial growth of the blast wave with time varies as  $R \sim t^{2/5}$  [1]. Then he compared, few years later, this radial growth with the photographs of the first atomic explosion in New Mexico. The predicted radial growth behavior is surprisingly verified accurately over a range of distance [4]. At almost exactly the same time during Taylor's involvement in the problem, John von Neumann in the USA and Leonid Sedov

in the Soviet Union were also working in the same problem independently. Neumann and Sedov found the exact solution and Taylor found the numerical solution.

By virtue of the sudden release of a large amount of energy from a point source, the speed of propagation of the wave can be faster than the speed of sound and gives rise to shock wave or blast wave. As a result of this, a region of very high pressure propagates to a region of low pressure, where the gas is at rest. As the shock propagates, the high-pressure area increase which results in decreasing pressure and density. Inside the shock wave region, the density, velocity, temperature, and pressure fields change continuously. But at the shock front, the region which separates the shock from the ambient gas, there is a large discontinuity in these quantities. The hydrodynamic description of the blast wave following the sudden release of a large amount of energy in a localized region, as in a nuclear explosion, is one of the classic problems in gas dynamics.

## **2.2 Gas dynamics**

A fluid can be described by local macroscopic quantities such as velocity, density, pressure, and temperature. A change in fluid flow velocity results in a change in pressure which leads to a change in density. At small velocities, the pressure change can be small compared to the atmospheric pressure which gives rise to a very small change in density and the fluid may be considered to be incompressible. If the velocity is large enough to cause a large pressure variation, the variation in fluid density is not negligible and the fluid is compressible. Gas dynamics deals with the study of compressible fluid flows.

An important quantity in gas dynamics is the Mach number, which is the ratio of flow velocity to the sound speed. Whenever this ratio is less than 1, the flow is said to be subsonic and when it is greater than 1, the flow is said to be supersonic. Shock waves are the characteristics of supersonic flow.

The understanding of gas dynamics has been developed by the nineteenth century mainly

by Poisson, Reimann, Rankine, Hugoniot, Mach, Prandtl, and Meyer. Gas dynamics have significant applications in gas turbines for the electricity production, aircraft engines, supersonic aircraft, rockets, scramjets, turbo compressors used in modern cars, torches used for welding and plasma surface treatment, kidney stone destruction by ultrasound waves, and astronomy to understand the evolution of stars and galaxies. In gas dynamics, the perturbations can be arbitrarily large enough to involve non-linear phenomena such as the formation of shock waves. Many non-linear phenomena like tsunami waves, car traffic waves, etc. are described by gas dynamics. The changes in the macroscopic quantities are described by different conservation laws.

- Conservation of mass: The fluid mass is conserved; that is, the fluid is neither created nor destroyed. That is,

$$\left( \begin{array}{l} \text{Rate of inflow of} \\ \text{the material to system} \end{array} \right) - \left( \begin{array}{l} \text{Rate of outflow of the} \\ \text{material from system} \end{array} \right) = \left( \begin{array}{l} \text{Rate of accumulation} \\ \text{inside the system} \end{array} \right). \quad (2.1)$$

Or,

$$\frac{\partial \rho}{\partial t} + \nabla \cdot (\rho \vec{v}) = 0. \quad (2.2)$$

This is the equation of continuity, where  $\rho$  is the fluid density,  $\vec{v}$  is the flow velocity, and the quantity  $\rho \vec{v}$  is the mass flux density.

- Conservation of momentum: According to the conservation of (linear) momentum,

$$\left( \begin{array}{l} \text{Rate of change} \\ \text{of momentum in} \\ \text{a control mass} \end{array} \right) = \left( \begin{array}{l} \text{Rate of momentum inflow} \\ \text{to control mass} \end{array} \right) - \left( \begin{array}{l} \text{Rate of momentum} \\ \text{outflow} \\ \text{from control mass} \end{array} \right) + \left( \begin{array}{l} \text{Sum of forces} \\ \text{acting on} \\ \text{control mass} \end{array} \right), \quad (2.3)$$

which is the Newton's second law of motion which states that the rate of change of momentum of a system of particles is equal to the sum of external forces acting on

them. This can be written as

$$\frac{\partial \vec{v}}{\partial t} + (\vec{v} \cdot \nabla) \vec{v} = -\frac{1}{\rho} \nabla p + \vec{f}, \quad (2.4)$$

where  $\partial_t \vec{v} + (\vec{v} \cdot \nabla) \vec{v} \equiv \frac{d\vec{v}}{dt}$ , is the rate of change of velocity of a given fluid particle as it moves about in space,  $\nabla p$  is the force acting on the fluid per unit volume and  $\vec{f}$  is the body forces act on the fluid particle. Equation (2.4) is known as the Euler's equation, one of the fundamental equations in fluid dynamics.

- Conservation of energy: According to the conservation of energy,

$$\left( \begin{array}{c} \text{Rate of change of energy} \\ \text{in a fluid element} \end{array} \right) = \left( \begin{array}{c} \text{Work done by the body} \\ \text{forces and surface forces} \end{array} \right) + \left( \text{Net heat flow} \right). \quad (2.5)$$

$$\rho \left( \frac{\partial e}{\partial t} + (\vec{v} \cdot \nabla) e \right) + p \nabla \cdot \vec{v} + \nabla \cdot \vec{q} = \rho \vec{f} \cdot \vec{v}, \quad (2.6)$$

where  $e$  is the energy, and  $\vec{q}$  is the heat flux. The last term comes from the work done on the fluid particle by external forces.

## 2.3 Shocks and boundary conditions

Under certain fluid flow conditions, there is an abrupt change in the fluid properties across a small region called the discontinuities and gives rise to shock waves. Here we go through a quick description of normal shocks. Normal shocks are shocks that are perpendicular to the flow velocity. Consider an infinitely thin shock in the  $yz$ -plane and the fluid flow is in the  $x$ -direction. The conservation laws for such a one-dimensional stationary flow in the



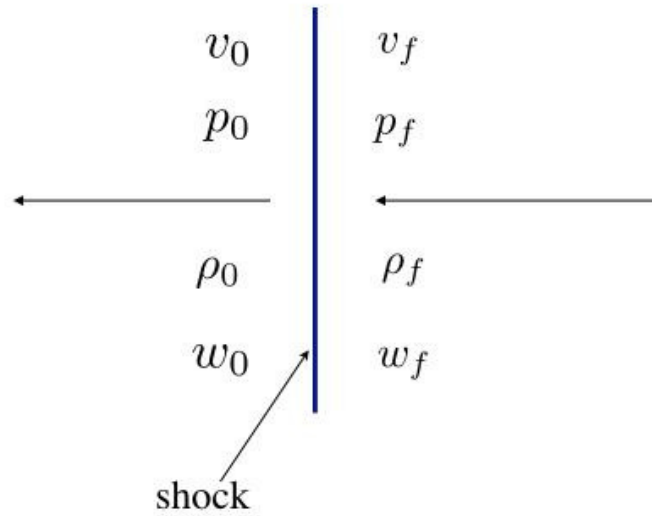


Figure 2.1: Schematic representation of normal shock to obtain the shock relations from the mass, momentum, and energy fluxes. The quantities  $v_0$ ,  $p_0$ ,  $\rho_0$ , and  $w_0$  are the velocity, pressure, density, and enthalpy ahead of the shock and the corresponding quantities with the subscript  $f$  are those behind the shock.

absence of external forces and heat flux can be written as

$$\begin{aligned}
 \frac{\partial}{\partial x}(\rho v) &= 0, \\
 \frac{\partial}{\partial x}(\rho v v) &= -\frac{\partial p}{\partial x}, \\
 \frac{\partial}{\partial x} \left[ \left( \frac{1}{2} \rho v^2 + \rho e \right) v \right] &= -\frac{\partial p v}{\partial x},
 \end{aligned} \tag{2.7}$$

where  $\rho$  is the density,  $v$ , the velocity,  $p$ , the pressure, and  $e$ , the internal energy of the fluid. In the case of normal shocks as shown in Fig 2.1, the jump conditions can be obtained as,

$$\begin{aligned}
 \rho_0 v_0 &= \rho_f v_f, \\
 p_0 + \rho_0 v_0^2 &= p_f + \rho_f v_f^2, \\
 w_0 + \frac{v_0^2}{2} &= w_f + \frac{v_f^2}{2},
 \end{aligned} \tag{2.8}$$

where  $w = e + \frac{p}{\rho}$  is the enthalpy of the shock, the suffix 0 represents the quantities ahead of the shock and the suffix  $f$  represents the quantities behind the shock and these conditions are called Rankine-Hugoniot conditions [35, 66].

## 2.4 TvNS solution

This section describes the exact solution to the problem of gas motion due to the sudden release of a finite amount of energy from the center. Note that, this is not the solution for the entire blast problem. In the real blast problem, thermal wave radiation, conduction, viscosity, radiation, ionization, etc. exist. But there is an intermediate scaling regime, where the problem can be solved hydrodynamically. The TvNS solution is the exact solution for the blast problem in the hydrodynamic limit. Initially, the gas is assumed to be at rest with vanishing pressure and arbitrary density  $\rho_0$ , except at the center. The mass, momentum, and energy are conserved locally so that the fluid flow is described by the corresponding continuity equations. The equations of motion for a compressible fluid is obtained from the conservation laws for density, momentum, and energy given in Eqs. (2.2)-(2.6) with  $f = 0$  as there is no body force.

Here, the energy  $e$  contains two parts, one is the kinetic part from the mean flow of the particles and the other is from fluctuations about this flow velocity, same as temperature so that a local temperature is defined in the problem. During the energy deposit, the disturbed region moves radially outward, leads to the quantities that do not depend on  $\theta$  and  $\phi$  coordinates. By considering isotropy, Eqs. (2.2)-(2.6) can be written in radial coordinates as,

$$\partial_t \rho + \partial_r(\rho v) + 2r^{-1} \rho v = 0, \quad (2.9)$$

$$\partial_t v + v \partial_r v + \rho^{-1} \partial_r p = 0, \quad (2.10)$$

$$\rho (\partial_t e + v \partial_r e) + p \left( \frac{2}{r} v + \partial_r v \right) + \frac{1}{r^2} \partial_r (r^2 q_r) = 0, \quad (2.11)$$

Assumptions of local equilibrium, and absence of heat conduction simplify the equations in the hydrodynamic limit. Also, from the first law of thermodynamics,

$$\begin{aligned} T ds &= de + p d\left(\frac{1}{\rho}\right) \\ &= de - \frac{p}{\rho^2} d\rho, \end{aligned} \quad (2.12)$$

$$T \frac{ds}{dt} = \frac{de}{dt} - \frac{p}{\rho^2} \frac{d\rho}{dt}, \quad (2.13)$$

where  $T$  is the temperature. Replace  $\frac{de}{dt}$  with Eq. (2.6),

$$\begin{aligned} T \frac{ds}{dt} &= -\frac{p}{\rho} \nabla \cdot \vec{v} - \frac{1}{\rho} \nabla \cdot \vec{q} - \frac{p}{\rho^2} \frac{d\rho}{dt} \\ &= -\frac{1}{\rho} \nabla \cdot \vec{q}, \end{aligned} \quad (2.14)$$

where, Eq. (2.2) is used. The assumption of neglect the heat conduction results in an isentropic flow (see Eq. (2.14)) (For the closed system like the one considered here, no energy flows out or coming in just after the initial impact. But the entropy in the system can increase according to the second law of thermodynamics. But the assumption of local equilibrium leads the entropy of the system to be a constant, called the isentropic process.). Therefore, Eq. (2.11) reduces to

$$\frac{ds}{dt} \equiv \partial_t s + v \partial_r s = 0. \quad (2.15)$$

Because of the assumption of local equilibrium, the local temperature, pressure, and density are related through the equation of state (EOS) of the gas, which is assumed to be that of the ideal gas in the TvNS theory. If we define the adiabatic index  $\gamma = c_p/c_v$ , the ratio of specific heats of the gas, using the ideal gas law one can write the entropy,

$s = c_v \ln\left(\frac{p}{\rho^\gamma}\right) + \text{constant}$ . The resulting equations for the conservation laws are [35, 66, 67]

$$\partial_t \rho + \partial_r(\rho v) + 2r^{-1} \rho v = 0, \quad (2.16)$$

$$\partial_t v + v \partial_r v + \rho^{-1} \partial_r p = 0, \quad (2.17)$$

$$\partial_t(p\rho^{-\gamma}) + v \partial_r(p\rho^{-\gamma}) = 0, \quad (2.18)$$

where  $\rho(r, t)$  is the density,  $v(r, t)$  is the radial velocity,  $p(r, t)$  is the pressure, and  $r$  is the radial distance from the location of the initial disturbance. Equations (2.16)–(2.18) describe the conservation of mass, momentum, and entropy respectively.

The main assumptions that have been made are

- Neglecting the effect of heat conduction, viscosity and gravity
- Existence of local equilibrium and an equation of state
- Gas obeys ideal gas law

The thermodynamic quantities are discontinuous across the shock front, the discontinuities being given by the Rankine-Hugoniot conditions [35, 66] described in Sec. 2.3. The mass flux, momentum flux, and energy flux give the following relations where the frame of reference moves with the shock front:

$$\rho_f(v_f - D) = \rho_0(v_0 - D), \quad (2.19)$$

$$p_f + \rho_f(v_f - D)^2 = p_0 + \rho_0(v_0 - D)^2, \quad (2.20)$$

$$1/2(v_f - D)^2 + w_f = 1/2(v_0 - D)^2 + w_0^2, \quad (2.21)$$

where  $D = \frac{dr_f}{dt}$  is the velocity of the shock,  $w$  is the enthalpy per particle and the suffix  $f$  represents the quantities behind the shock front. If the explosion is strong enough, the pressure behind the shock are very high compared to the pressure ahead, resulting that the unperturbed pressure  $p_0 = 0$ . Also, the initial velocity of the gas is zero; these two facts

reduce the Equations (2.19)–(2.21) to,

$$\rho_f(v_f - D) = -\rho_0 D, \quad (2.22)$$

$$p_f + \rho_f(v_f - D)^2 = \rho_0 D^2, \quad (2.23)$$

$$1/2(v_f - D)^2 + w_f = 1/2 D^2. \quad (2.24)$$

Equations (2.23) and (2.24) can be rewritten as,

$$p_f + \rho_f v_f(v_f - D) = 0, \quad (2.25)$$

$$\rho_f(v_f - D) \left[ 1/2(v_f - D)^2 + w_f \right] = -\rho_0 D^3/2. \quad (2.26)$$

The enthalpy per particle,  $w = u + \frac{p}{\rho} = \frac{p}{\rho} \left( \frac{\gamma}{\gamma-1} \right)$ , where  $u = 3/2 k_B T = c_v T$ , is the internal energy per mass. Therefore, the Eq. (2.26) now takes the form,

$$\rho_f(v_f - D) \left[ \frac{1}{2}(v_f - D)^2 + \frac{\gamma}{\gamma-1} \frac{p_f}{\rho_f} \right] = -\frac{1}{2} \rho_0 D^3. \quad (2.27)$$

By simplifying Equations (2.22), (2.25), and (2.27) we obtain the quantities behind the shock front in terms of the initial density and the shock velocity as given below:

$$v_f = \frac{2D}{\gamma+1}, p_f = \frac{2}{\gamma+1} \rho_0 D^2, \rho_f = \frac{\gamma+1}{\gamma-1} \rho_0. \quad (2.28)$$

The energy of the gas behind the shock contains kinetic part comes from the motion of the particles and thermal energy, due to the fluctuations. The energy per mass of the gas is

$$\begin{aligned} e &= \rho \left( \frac{v^2}{2} + c_v T \right) \\ &= \rho \left( \frac{v^2}{2} + \frac{p}{(\gamma-1)\rho} \right). \end{aligned} \quad (2.29)$$

Initially the gas is at rest with some arbitrary density which gives the initial conditions as:

$\rho(r, 0) = \rho_0, p(r, 0) = 0, v(r, 0) = 0$ , except at the centre.

The total energy inside the gas which is  $E_0$  deposited at the centre,

$$4\pi \int_0^\infty \rho \left[ \frac{v^2}{2} + \frac{1}{\gamma - 1} \frac{p}{\rho} \right] r^2 dr = E_0. \quad (2.30)$$

The properties of the system  $\rho$ ,  $p$ , and  $v$  depend on the parameters  $\rho_0$ ,  $E_0$ ,  $r$ ,  $t$ , and  $\gamma$  with dimensions  $[ML^{-3}]$ ,  $[ML^2T^{-2}]$ ,  $L$ ,  $T$ , and 1, which give rise to two independent parameters  $\xi$  and the constant  $\gamma$ , where

$$\xi = r \left( \frac{E_0 t^2}{\rho_0} \right)^{-1/5}, \quad (2.31)$$

is non-dimensionalized length. Non-dimensionalizing the different thermodynamic quantities converts the Eqs. (2.16)–(2.18) into ordinary differential equations (ODE). From dimensional analysis,

$$\begin{aligned} p &= \frac{\rho_0 r^2}{t^2} P(\xi), \\ \rho &= \rho_0 R(\xi), \\ v &= \frac{r}{t} V(\xi), \end{aligned} \quad (2.32)$$

where  $P$ ,  $R$ , and  $V$ , are scaling functions.

In terms of the scaling functions, Eqs. (2.16)–(2.18) simplify to

$$\begin{aligned} \left( V - \frac{2}{5} \right) R \frac{dV}{d \ln \xi} + \frac{dP}{d \ln \xi} - RV + RV^2 + 2P &= 0, \\ \frac{dV}{d \ln \xi} + \left( V - \frac{2}{5} \right) \frac{d \ln R}{d \ln \xi} + 3V &= 0, \\ \frac{d}{d \ln \xi} \left( \ln \frac{P}{R^\gamma} \right) - \frac{2(1-V)}{V-2/5} &= 0. \end{aligned} \quad (2.33)$$

The boundary conditions for this system of ODEs are obtained by substituting Equa-

tions (2.32) into Equations (2.28) and are given as:

$$\begin{aligned} P(\xi_f) &= \frac{8}{25(\gamma + 1)}, \\ V(\xi_f) &= \frac{4}{5(\gamma + 1)}, \\ R(\xi_f) &= \frac{\gamma + 1}{\gamma - 1}, \end{aligned} \quad (2.34)$$

where  $\xi_f$  is the position of the shock front which is determined by the condition that total energy is conserved:

$$4\pi \int_0^{\xi_f} R(\xi) \left[ \frac{V^2(\xi)}{2} + \frac{P(\xi)}{(\gamma - 1)R(\xi)} \right] \xi^4 d\xi = 1. \quad (2.35)$$

The exact solution of Eq. (2.33) in three dimensions with the boundary condition as in Eq. (2.34) is [1, 2, 3, 5, 67]:

$$\left[ \frac{\xi_f}{\xi} \right]^5 = C_1 V^2 \left[ 1 - \frac{3\gamma - 1}{2} V \right]^{v_1} \left[ \frac{5}{2} \gamma V - 1 \right]^{v_2}, \quad (2.36)$$

$$R = C_2 \left[ \frac{5}{2} \gamma V - 1 \right]^{v_3} \left[ 1 - \frac{3\gamma - 1}{2} V \right]^{v_4} \left[ 1 - \frac{5}{2} V \right]^{v_5}, \quad (2.37)$$

$$P = C_3 V^2 \left[ 1 - \frac{5V}{2} \right]^{v_6} \left[ \frac{5\gamma V}{2} - 1 \right]^{v_7} \left[ 1 - \frac{(3\gamma - 1)V}{2} \right]^{v_8}, \quad (2.38)$$

where

$$\begin{aligned} C_1 &= \left[ \frac{5}{4}(\gamma + 1) \right]^2 \left[ \frac{5(\gamma + 1)}{7 - \gamma} \right]^{v_1} \left( \frac{\gamma + 1}{\gamma - 1} \right)^{v_2}, \\ C_2 &= \left( \frac{\gamma + 1}{\gamma - 1} \right)^{v_3 + v_5 + 1} \left[ \frac{5(\gamma + 1)}{7 - \gamma} \right]^{v_4}, \\ C_3 &= \frac{1}{2} \left( \frac{\gamma + 1}{\gamma - 1} \right)^{-v_5 - v_3} (1 + \gamma) \left[ \frac{5(1 + \gamma)}{7 - \gamma} \right]^{v_4}, \end{aligned} \quad (2.39)$$

and

$$\begin{aligned}
v_1 &= \frac{12 - 7\gamma + 13\gamma^2}{-1 + \gamma + 6\gamma^2}, & v_2 &= -\frac{5(\gamma - 1)}{2\gamma + 1}, \\
v_3 &= \frac{3}{1 + 2\gamma}, & v_4 &= \frac{-12 + 7\gamma - 13\gamma^2}{(-2 + \gamma)(-1 + \gamma + 6\gamma^2)}, \\
v_5 &= \frac{2}{-2 + \gamma}, & v_6 &= \frac{\gamma}{-2 + \gamma}, \\
v_7 &= \frac{2 - 2\gamma}{1 + 2\gamma}, & v_8 &= v_4.
\end{aligned} \tag{2.40}$$

Near the shock front, the four scaling functions  $V$ ,  $R$ , and  $P$  are discontinuous, as given by Eq. (2.34). Near the shock center ( $\xi \rightarrow 0$ ), the scaling functions have power law singularities. These may be determined from Eqs. (2.36) to (2.38). From Eq. (2.36), when  $\xi \rightarrow 0$ , it is easy to see that  $V \rightarrow 2/(5\gamma)$ .  $V$  approaches the limit as  $V - 2/(5\gamma) \sim \xi^{-5/v_2}$ . From Eqs. (2.37) and (2.38), we obtain  $R(\xi) \sim \xi^{-5v_3/v_2}$ , and  $P(\xi) \sim \xi^{-5v_7/v_2}$ . Summarizing,  $\xi \rightarrow 0$ ,

$$V - \frac{2}{5\gamma} \sim \xi^{-5/v_2}, R(\xi) \sim \xi^{-5v_3/v_2}, P(\xi) \sim \xi^{-5v_7/v_2}. \tag{2.41}$$

The assumption of ideal gas equation of state in the TvNS theory allows one to relate the scaling functions too. So,  $P = RE$ , where  $E$  is the scaled thermal energy, and near the shock center,  $\xi \rightarrow 0$ , the scaled thermal energy,

$$E(\xi) \sim \xi^{-5(v_7 - v_3)/v_2}. \tag{2.42}$$

Air mainly consists of diatomic gases nitrogen and oxygen. For a diatomic gas, there are 3 translational degrees of freedom and 2 rotational degrees of freedom, so that the total internal energy is  $\frac{5}{2}RT$ , where  $R$  is the universal gas constant. This implies that  $\gamma = 7/5$  (or 1.4). From Eq. (2.35), it is observed that the shock front is located at  $\xi_f = 1.032778$  for  $\gamma = 7/5$ . The density, velocity, and pressure of the gas are distributed as shown in Fig 2.2.

One question arose was whether  $\gamma = 7/5$  is applicable inside the shock region or not! It



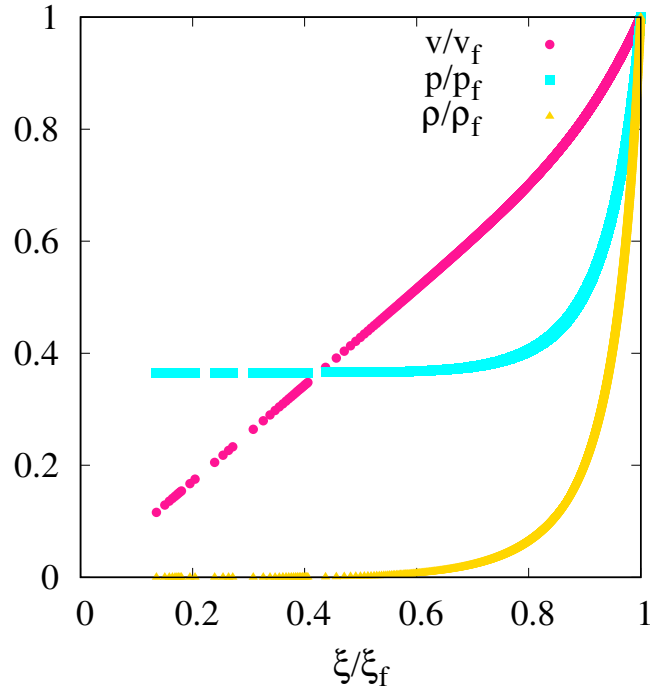


Figure 2.2: The velocity, density, and pressure distributions inside the blast wave for  $\gamma = 7/5$ .

could be the case that the diatomic gas decomposes to monoatomic inside the fireball and in that case  $\gamma = 5/3$  (or 1.67). Also, in this thesis, we compare the TvNS results with the results from the simulation. The simulation is carried out for a system of hard spheres which is monoatomic and so,  $\gamma = 5/3$ . So the density, velocity, and pressure distributions for a gas with  $\gamma = 5/3$  are plotted in Fig 2.3. In this case, the shock front is located at  $\xi_f = 1.151667$ .

## 2.5 Applications of TvNS theory

The radial growth described in the TvNS theory has been observed in laser-driven blast waves formed in the laboratory model to explore the astrophysically relevant hydrodynamic phenomena. Few of them are summarized below:

- **M. J. Edwards *et al.* [6]:** In this experiment, cylindrically symmetric blast waves

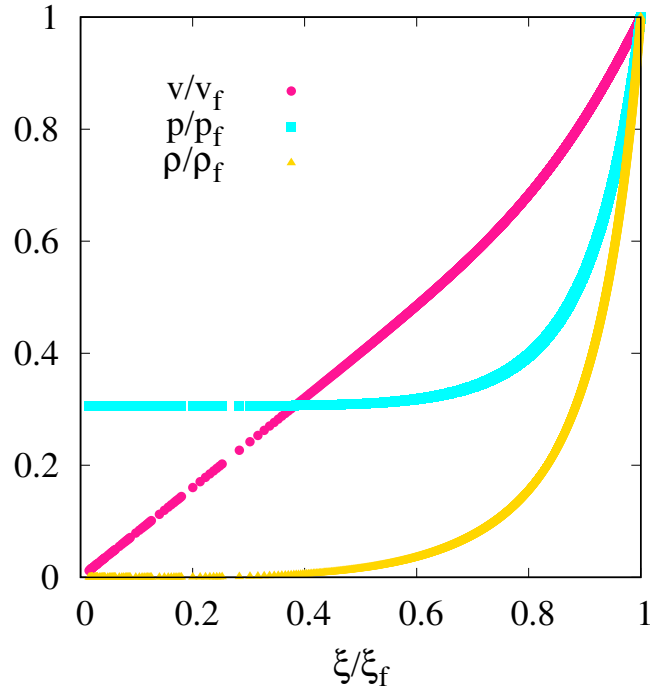


Figure 2.3: The velocity, density, and pressure distributions inside the blast wave for a monoatomic gas with  $\gamma = 5/3$ .

are formed by focussing laser pulses in gas jets of neon, argon, and xenon. The laser pulses are focussed along the axis perpendicular to the axis of gas jets. In gases with a high atomic number, the radiative effects are important and prior to blast wave, these gases radiate much more than the gases with less atomic number. In both neon and argon, the radius of the blast wave exhibits the power-law behavior with time,  $R(t) \sim t^{1/2}$  as described in TvNS theory. While in the case of xenon gas, the radial growth shows a behavior at which the power is less than 1/2 because of the radiative effect.

- **A. D. Edens *et al.* [7]:** Here, the laser beam varying in a range of energy illuminates a pin target of steel or nylon in a chamber filled with xenon or nitrogen gas. This results in an explosion that forms a spherical blast wave in the surrounding gas. The trajectory of blast wave evolved in xenon gas is highly radiative during earlier stages of time and later the trajectory is consistent with the TvNS solution. The

evolution of the shock in nitrogen gas is consistent with TvNS solution always.

- **A. S. Moore *et al.* [8]:** In this paper, the experiment performed in a cluster media is explained. Here, an intense laser pulse is focussed in plasma by 'laser machining technique' which destroys clusters in selected regions while keeping the atomic density constant. This energy deposition produces cylindrical blast waves. The 'tailored' blast waves produced in the cluster media indicate a radial growth of  $\sim 0.5$  as described by TvNS theory.



# Chapter 3

## Computational Methods

This chapter briefly describes the computational methods employed in this thesis. These are event-driven molecular dynamics (MD) simulations for simulating shocks in microscopic particle-based models, and a numerical algorithm for solving the ODEs describing hydrodynamics of shocks in elastic media.

Simulations play an important role in the study of a system of granular materials because of the lack of a comprehensive theory. A widely used simulation method is molecular dynamics (MD) simulation which can be of either time-driven MD simulation or event-driven MD simulation. The conventional time-driven MD simulations are used in the case of continuous potential and is based on solving Newton's equation of motion. On the other hand, event-driven MD simulations are efficiently used in the case of hard particles.

### 3.1 Time-Driven Molecular Dynamics Simulation

Granular particles interact only through mechanical contact and the quantum effects can be neglected. The motion of such a kind of system are described by Newton's equation of

motion:

$$m\ddot{\vec{r}}_i = \vec{F}_i(\vec{r}_1, \vec{v}_1, \dots, \vec{r}_N, \vec{v}_N), \quad (3.1)$$

where  $\vec{r}_i$  is the position of the  $i$  th particle,  $\vec{v}_i$  is the velocity of particle  $i$ , and  $\vec{F}_i$  is the force acting on the  $i$  th particle by all the other particles  $j$ , where  $j \neq i$ . The mass  $m$  has been assumed to be same for all particles. It is not always possible to solve this set of coupled equations analytically. But the approximate solution can be found numerically by conventional molecular dynamics simulations. Here, time is discretized into small intervals  $\Delta t$ , and the position and velocity of the particles are updated for each  $\Delta t$ . Time marches forward in discrete steps and when the number of particles becomes large, it can be quite time-consuming.

## 3.2 Event-Driven Molecular Dynamics Simulation

In the case of hard particles where there is no long-range interaction and the interaction is only on contact, a more efficient simulation method is used. In hard sphere systems the potential  $u(r)$  between two particles is

$$u(r) = \begin{cases} +\infty & (0 \leq r \leq a), \\ 0 & (a \leq r), \end{cases} \quad (3.2)$$

where  $a$  is the diameter of the particle. Due to this infinite potential, the duration of contact of the particles in a collision is zero. As a consequence, the collisions can be considered to be instantaneous and all collisions to be binary. Also, in hard sphere system, particles move ballistically until they encounter a collision. Hence, given the velocity and position of a particle at some time  $t$ , one can determine all the future collision events. Here, the simulation method proceeds with discrete events of collision known as the event-driven molecular dynamics (EDMD) simulation [68]. In EDMD time marches forward in jumps and for dilute systems, it is much more efficient than the conventional MD.

A simple event-driven algorithm for force-free granular gas is given below:

1. Initialize the positions  $\vec{r}_i$  and velocities  $\vec{v}_i$  of the particles at time  $t = 0$ . The particles should not overlap each other as the system contains hard particles.
2. Find the earliest occurring collision in the system. In order to obtain this, we must know the time of occurrence of all possible future collisions.
  - Consider two particles  $i, j$  having mass  $m$  and diameter  $d$  at positions  $\vec{r}_i$  and  $\vec{r}_j$  respectively at time  $t_k$ . They will collide at some future time  $t_{k+1}$  if,

$$|(\vec{r}_i + (t_{k+1} - t_k)\vec{v}_i) - (\vec{r}_j + (t_{k+1} - t_k)\vec{v}_j)| = d, \quad (3.3)$$

has a solution  $t_{k+1}$  with  $t_{k+1} > t_k$ . By defining  $\vec{r}_{ij} = \vec{r}_i - \vec{r}_j$  and  $\vec{v}_{ij} = \vec{v}_i - \vec{v}_j$ , above equation becomes

$$(t_{k+1} - t_k)^2 + 2(t_{k+1} - t_k)\frac{\vec{r}_{ij} \cdot \vec{v}_{ij}}{\vec{v}_{ij}^2} + \frac{\vec{r}_{ij}^2 - d^2}{\vec{v}_{ij}^2} = 0. \quad (3.4)$$

A necessary condition for collision is,

$$\vec{r}_{ij} \cdot \vec{v}_{ij} < 0, \quad (3.5)$$

since the particles must approach each other for a collision to happen. Equation (3.4) has real solutions if

$$\left[ \frac{\vec{r}_{ij} \cdot \vec{v}_{ij}}{\vec{v}_{ij}^2} \right]^2 + \frac{d^2 - \vec{r}_{ij}^2}{\vec{v}_{ij}^2} > 0. \quad (3.6)$$

The particles  $i$  and  $j$  will collide at  $t_{k+1}$  only when Eqs. (3.5) and (3.6) are satisfied. By solving Eq. (3.4),

$$t_{k+1} - t_k = -\frac{\vec{r}_{ij} \cdot \vec{v}_{ij}}{\vec{v}_{ij}^2} - \sqrt{\left( \frac{\vec{r}_{ij} \cdot \vec{v}_{ij}}{\vec{v}_{ij}^2} \right)^2 + \frac{d^2 - \vec{r}_{ij}^2}{\vec{v}_{ij}^2}}. \quad (3.7)$$

As the numerical evaluation of Eq. (3.7) in a computer algorithm is not stable, we use a mathematically equivalent expression of Eq. (3.7) which is numerically stable:

$$t_{k+1} - t_k = \frac{\vec{r}_{ij}^2 - d^2}{-\vec{r}_{ij} \cdot \vec{v}_{ij} + \sqrt{(\vec{r}_{ij} \cdot \vec{v}_{ij})^2 + \vec{v}_{ij}^2(d^2 - \vec{r}_{ij}^2)}}. \quad (3.8)$$

In this way we can determine the future collision time  $t_{k+1}$  of all pairs  $(i, j)$ . The earliest future collision time is determined by minimum of all these.

### 3. Increase time to the time of occurrence of this earliest collision

- New position of the particles can be found out easily as the particles move ballistically between successive collisions.

$$\vec{r}_i(t_{k+1}) = \vec{r}_i(t_k) + \vec{v}_i(t_k)(t_{k+1} - t_k), \quad 1 \leq i \leq N, \quad (3.9)$$

where  $t_k$  is the time at  $k$  th instant with  $t_k < t_{k+1}$  and  $v_i(t_k)$  represents the velocity of the  $i$  th particle after the collision which occurred at time  $t_k$ .

- Compute the new velocities of the particles after their collisions at  $t_{k+1}$  using the collision rule, which gives the post-collision velocities in terms of pre-collision velocities, described as below:

If  $\vec{u}_1$  and  $\vec{u}_2$  are the velocities of two particles 1 and 2 before the collision, then the velocities after the collision,  $\vec{v}_1$  and  $\vec{v}_2$ , are given by

$$\vec{v}_1 = \vec{u}_1 - \frac{1+r}{2}[\hat{n} \cdot (\vec{u}_1 - \vec{u}_2)]\hat{n}, \quad (3.10)$$

$$\vec{v}_2 = \vec{u}_2 - \frac{1+r}{2}[\hat{n} \cdot (\vec{u}_2 - \vec{u}_1)]\hat{n}, \quad (3.11)$$

where  $r$  is the coefficient of restitution and  $\hat{n}$  is the unit vector along the line joining the centers of particles 1 and 2. The collisions are elastic when  $r = 1$ , and inelastic and dissipative otherwise. In a collision, the tangential compo-



ment of the relative velocity remains unchanged as there is no force acting along this direction, while the magnitude of the longitudinal component is reduced by a factor  $r$ .

- Velocities of the other particles remain unchanged.

4. Repeat the steps 2-3 for all the next collisions.

To determine the earliest collision occurring in the system, we must calculate the collision time for all the  $O(N^2)$  pairs of particles and so the algorithm becomes inefficient. In order to improve efficiency, we divide the simulation box into small cells whose size is same as the diameter of the particle. Now we determine the collision time of a particle with its neighboring particles instead of calculating that with all the other  $N - 1$  particles. For a particle to collide with a particle other than one of its neighbors, it has to move out of its cell. Therefore introduce an additional event known as cell-crossing. During cell-crossing, the particle leaves its present cell and moves to an adjacent cell. Future collision time of this particle can be calculated with its new neighbors. Even though including events of cell-crossings increase the number of events, the calculation of collision times involves only local cells and becomes independent of  $N$  rather than proportional to  $N^2$ . This speeds up the algorithm considerably.

### **3.3 Numerical Method to solve the set of ODEs**

We describe the algorithm used to solve the hydrodynamic equations describing the shock. While the TvNS solution exists when the equation of state is that of an ideal gas, such solutions do not exist for a more complicated equation of state. Here we describe the numerical method that we use to solve the set of hydrodynamic equations. We reproduce

the set of hydrodynamic equations (see Eq. (2.33)) to make this chapter self-contained:

$$\begin{aligned} \left(V - \frac{2}{5}\right)R \frac{dV}{d \ln \xi} + \frac{dP}{d \ln \xi} - RV + RV^2 + 2P &= 0, \\ \frac{dV}{d \ln \xi} + \left(V - \frac{2}{5}\right) \frac{d \ln R}{d \ln \xi} + 3V &= 0, \\ \frac{d}{d \ln \xi} \left( \ln \frac{P}{R^\gamma} \right) - \frac{2(1-V)}{V-2/5} &= 0. \end{aligned} \quad (3.12)$$

with boundary conditions

$$\begin{aligned} P(\xi_f) &= \frac{8}{25(\gamma+1)}, \\ V(\xi_f) &= \frac{4}{5(\gamma+1)}, \\ R(\xi_f) &= \frac{\gamma+1}{\gamma-1}, \end{aligned} \quad (3.13)$$

where the scaled variable  $\xi$  is bounded by  $\xi_f$  at which the shock front is located. The solution of Eqs. (3.12) and (3.13) satisfies the constraint equation

$$4\pi \int_0^{\xi_f} R(\xi) \left[ \frac{V^2(\xi)}{2} + \frac{P(\xi)}{(\gamma-1)R(\xi)} \right] \xi^4 d\xi = 1. \quad (3.14)$$

This set of ODEs in the TvNS theory can be solved numerically as follows. First convert the boundary value problem to an initial value problem, by choosing a value of  $\xi_f$  treating the boundary conditions (Eq. (3.13)) as initial value. Then solve for  $V(\xi)$ ,  $R(\xi)$ , and  $P(\xi)$  for all  $0 < \xi < \xi_f$ . Check if the solution satisfies Eq. (3.14) within a pre-defined tolerance of  $10^{-6}$ . If not, choose a new value of  $\xi_f$  and iterate till the solution satisfies Eq. (3.14). The procedure to determine  $\xi_f$  is represented schematically as shown in Fig 3.1. For every  $\xi_f$  the ODEs are solved on MATHEMATICA.

To benchmark this procedure, we find the solution of Eq. (3.12) and compare this with the exact solutions given in Eqs. (2.36)-(2.38) for  $\gamma = 5/3$ . From the constraint equation (Eq. (3.14)), we obtain  $\xi_f = 1.15167$  for  $\gamma = 5/3$ . The scaled quantities obtained by

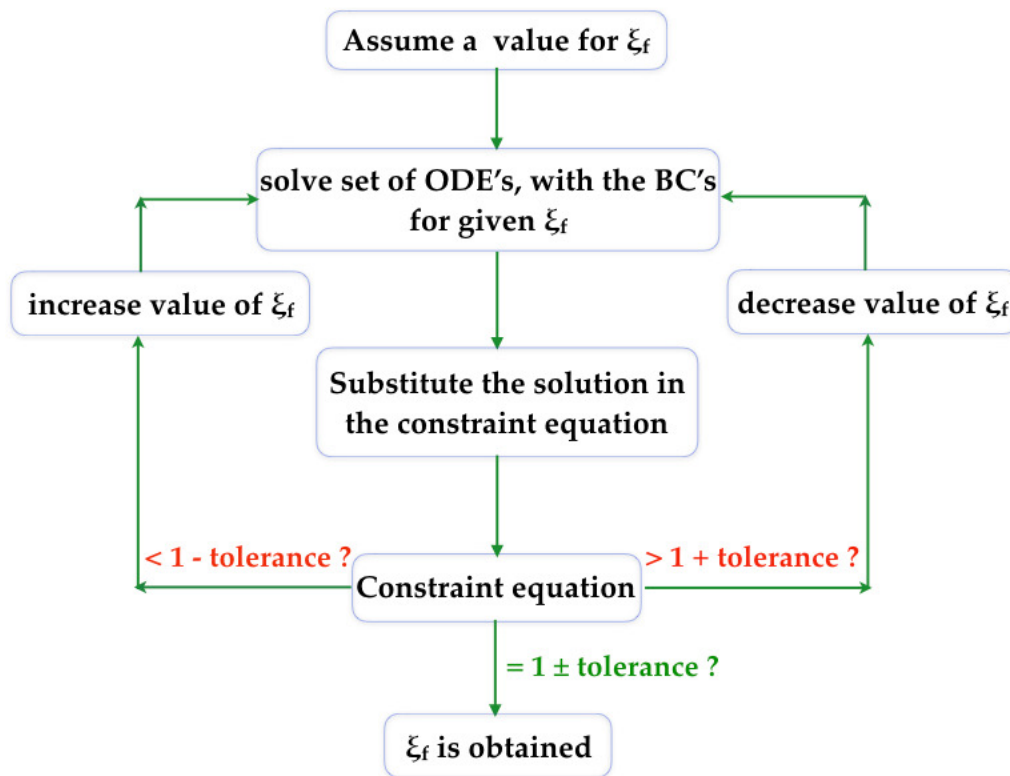


Figure 3.1: Schematic representation of the procedure to solve the equations numerically solving the set of equations numerically matches well with the exact solutions as shown in Fig 3.2, where the points represent data by solving the set of equations numerically and the solid line represents the exact solution.

The same exercise can be done for the case of  $\gamma = 7/5$  for which  $\xi_f = 1.032778$  which is same as that found earlier in Ref. [67].

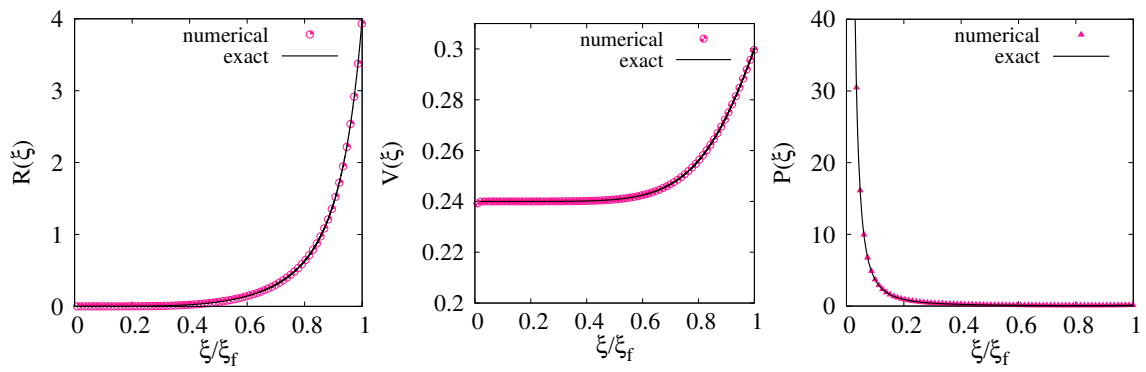


Figure 3.2: The scaling functions  $R(\xi)$ ,  $V(\xi)$ , and  $P(\xi)$  corresponding to density, velocity, and pressure respectively are plotted as a function of the scaled distance. The data are obtained by solving Eqs. (3.12) numerically for  $\gamma = 5/3$ .

# Chapter 4

## Shock propagation following an intense explosion: Comparison between hydrodynamics and simulation

### 4.1 Introduction

In this chapter, we compare the results and assumptions of TvNS theory with the solutions from large scale event-driven MD simulation of hard sphere gas in three dimensions. From the global conservation law for energy, it is straightforward to obtain, using dimensional analysis, that the radius of the shock front  $R(t)$  scales with time  $t$  as  $R(t) \sim t^{2/d+2}$  where  $d$  is the spatial dimension [1, 4, 2, 3, 5]. In addition to the scaling law for  $R(t)$ , from the local conservation laws for density, momentum, and energy, it is possible to obtain self-similar scaling solution for the radial distribution of pressure, density, velocity, and temperature. The exact solution found by Taylor, von Neumann and Sedov [1, 4, 2, 3, 5], called TvNS theory was described in Chapter 2 [See Eqs. (2.36)-(2.38)].

While the hydrodynamic equations and their modifications have been studied in detail,

there has been little or no verification of the theory or its assumptions using microscopic models. It is only been more recently that the radial growth in the TvNS theory has been tested in simulations of microscopic models in which kinetic energy is given to a few particles at the center of a collection of stationary elastic particles. The radius of the disturbance has been shown to match with the TvNS prediction in both two [9, 10] and three dimensions [10]. The predictions for the radial distribution of density, flow velocity, and temperature fields in two dimensions have recently been compared with results from molecular dynamics simulations [17]. Here, in the TvNS solution, the ideal gas law was replaced with a more realistic constitutive relation expressing pressure in terms of density and temperature. It was found that the simulations reproduce well the TvNS solution for low to medium densities, except for a small difference in the discontinuities at the shock front, and a slight discrepancy near the shock center. When the number density of the ambient gas is high, the TvNS solution was seen to not describe well the data near the shock front [17]. However, the key assumptions of local equilibrium and the existence of an equation of state that are assumed in the TvNS solution were not tested in the simulations. Also, the simulation data was presented only for a single time, and thus it is not very clear whether the scaling limit has been reached. While these simulations were in two dimensions, there are no similar studies in three dimensions. Thus, it is not very clear where the TvNS solution is reproducible in microscopic models and which assumptions of the TvNS theory are actually valid.

We perform extensive event-driven molecular dynamics simulations of hard spheres in three dimensions to test the predictions as well as the validity of the assumptions of the TvNS theory. We show unambiguously that the TvNS theory does not match well to describe the numerical data for most distances, ranging from the shock center to the shock front. We modify the TvNS theory to replace the constitutive relation from the ideal gas law to the virial equation of state (EOS) (up to 10 terms) for a hard sphere gas. While inclusion of the more realistic constitutive relation into the TvNS theory modifies the predictions for the scaling functions, especially near the shock front, they still inadequate to

describe the data well in terms of the exponents characterizing the power law behavior near the shock center. To understand this discrepancy, we test numerically the various assumptions of the TvNS theory. A key assumption of the TvNS theory is the existence of an equation of state linking pressure, temperature and density. By measuring these quantities independently, we show that numerically, the virial EOS is satisfied, justifying this key assumption. We also find that energy is equipartitioned equally among the different degrees of freedom, as would be expected in a system in local equilibrium. However, we find that the distribution of the velocity fluctuations, in regions between the shock center and shock front, has non-gaussian tails. In particular, it is asymmetric with non-zero skewness and an exponential tail, showing that local thermal equilibrium is not reached. The lack of local equilibrium could be a possible reason for the TvNS theory to fail to explain the simulation results in three dimensions. Also, we check that within the densities that we have studied, the motion is subsonic within the wave and supersonic with respect to the ambient gas, as implicitly assumed in the TvNS solution.

The remainder of the chapter is organized as follows. In Sec. 4.2, we give details of the simulations and we present a detailed comparison between the numerically obtained data and the TvNS solution for two different number densities of the ambient gas. In Sec. 4.3, we describe how the TvNS theory is modified when a more realistic virial EOS is used for the hard sphere gas. The effect of including higher order terms is discussed and compared with results from simulation. In Sec. 4.4, we show that, within the simulations, the virial EOS is obeyed locally. Also, equipartitioning of energy is shown to hold. It is also shown that the distribution of the velocity fluctuations is non-gaussian. In Sec. 4.5, a discussion is developed on the possible effects of including heat conduction. In Sec. 4.6, we show that the flow velocity is subsonic within the blast and supersonic when compared to the ambient gas into which the shock is expanding. We summarize this chapter in Sec. 4.7. The content of this chapter is included in Ref. [69].

## 4.2 Comparison with event-driven simulations

In this section, we compare the predictions of the TvNS solution for density, velocity, pressure, and temperature profiles with results from large scale event-driven simulations [68] of a collection of elastic hard spheres. Consider a system of identical hard spheres in three dimensions whose mass and diameter are set to one. Initially, all particles are at rest and uniformly distributed in space. The system is perturbed by an initial localized input of energy at the origin. We model an isotropic impulse by giving a speed  $v_0 = 1$  to 6 particles near the center along  $\pm x$ ,  $\pm y$  and  $\pm z$  directions. The particles move ballistically until they undergo elastic momentum conserving collisions with other particles. If  $\vec{u}_1$  and  $\vec{u}_2$  are the velocities of two particles 1 and 2 before collision, then the velocities after collision,  $\vec{v}_1$  and  $\vec{v}_2$ , are given by

$$\begin{aligned}\vec{v}_1 &= \vec{u}_1 - [\hat{n} \cdot (\vec{u}_1 - \vec{u}_2)]\hat{n}, \\ \vec{v}_2 &= \vec{u}_2 - [\hat{n} \cdot (\vec{u}_2 - \vec{u}_1)]\hat{n},\end{aligned}\tag{4.1}$$

where  $\hat{n}$  is the unit vector along the line joining the centers of particles 1 and 2.

We simulate systems with number densities  $\rho_0 = 0.1$  and  $0.4$ , much smaller than the random closed packing density. The system is large enough so that the moving particles do not reach the boundary up to the times we have simulated, so that there are no boundary effects. The data are averaged over 150 different histories. We also check that the data for an intermediate density [ $\rho_0 = 0.25$ ] show a trend that is intermediate between that for  $\rho_0 = 0.1$  and  $0.4$ .

The initial perturbation creates a disturbance that propagates outward in a radially symmetric fashion. A shock front separates the moving particles from the stationary ones. The radius of this shock front has been earlier shown to increase as  $t^{2/5}$  in event-driven simulations, consistent with the TvNS solution [10]. But the scaling functions have not yet been tested with simulations to the best of our knowledge.



The set of partial differential equations described in Eqs. (2.16)–(2.18) are converted to the solvable ordinary differential equations (see Eq. (2.33)) by using dimensional analysis as given in Eq. (2.32). But in simulation, one can get temperature easily and this gives an additional check. Dimensional analysis gives,

$$\begin{aligned}
p &= \frac{\rho_0 r^2}{t^2} P(\xi), \\
\rho &= \rho_0 R(\xi), \\
v &= \frac{r}{t} V(\xi), \\
\varepsilon &= \frac{k_B T}{m_0} = \frac{r^2}{t^2} E(\xi),
\end{aligned} \tag{4.2}$$

where

$$\xi = r \left( \frac{E_0 t^2}{\rho_0} \right)^{-1/5}, \tag{4.3}$$

is non-dimensionalized length,  $E_0$  is the initial energy that is deposited into the system,  $\rho_0$  is the ambient mass density,  $T$  is the local temperature,  $k_B$  is Boltzmann constant,  $m_0$  is the mass of a particle, and  $P$ ,  $R$ ,  $V$ , and  $E$ , are scaling functions.  $\varepsilon$  is the thermal energy per unit mass. The four scaling functions are not independent, but related through the ideal gas law as

$$P = RE. \tag{4.4}$$

Our aim is to numerically determine the scaling functions  $R(\xi)$ ,  $V(\xi)$ ,  $E(\xi)$ , and  $P(\xi)$ , corresponding to density, velocity, temperature, and pressure respectively. The thermal energy is measured from the velocity fluctuations obtained by subtracting out the mean radial velocity  $v_r(r, t)\hat{r}$  from the instantaneous velocity. The pressure is measured from the local collision rate. For the hard sphere gas in three dimensions, pressure is given by the expression [70]

$$p = \rho T - \frac{\rho}{3N\delta t} \sum_{\text{collisions}} b_{ij}, \tag{4.5}$$

where  $b_{ij} = \vec{r}_{ij} \cdot \vec{v}_{ij}$ , where  $\vec{r}_{ij}$  and  $\vec{v}_{ij}$  respectively are the relative positions and velocities of the particles  $i$  and  $j$  undergoing collisions,  $\delta t$  is the time duration of measurement, and

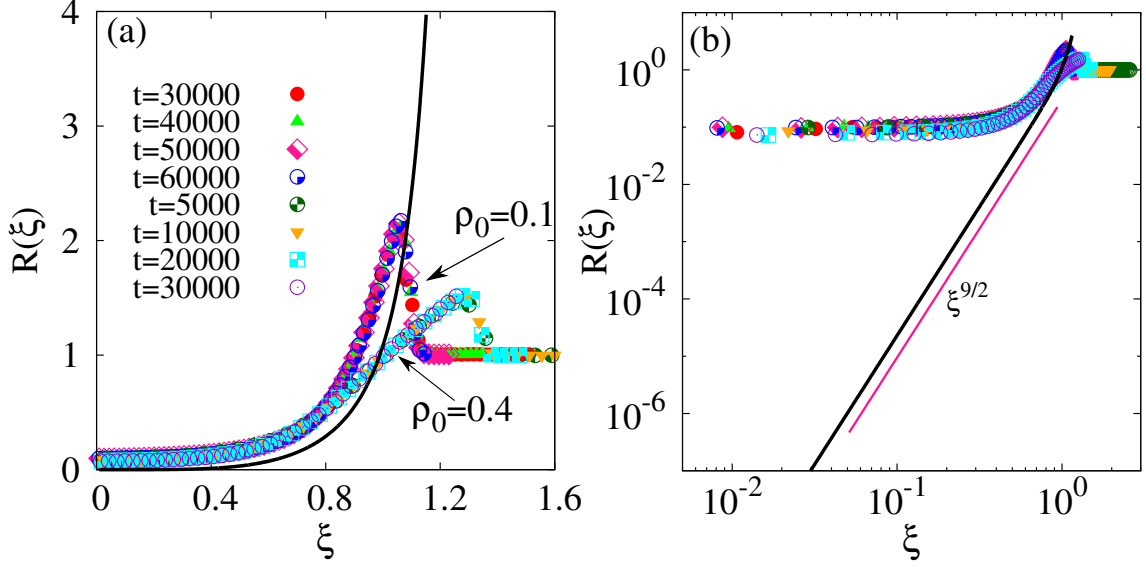


Figure 4.1: (a) The variation of the scaling function  $R(\xi)$  corresponding to non-dimensionalized density [see Eq. (4.2)] with scaled distance  $\xi$ . The data are shown for 2 different initial densities  $\rho_0 = 0.1$  and  $0.4$ . For  $\rho_0 = 0.1$ , the different times are  $t = 30000$ ,  $40000$ ,  $50000$ ,  $60000$ , and for  $\rho = 0.4$ ,  $t = 5000$ ,  $10000$ ,  $20000$ ,  $30000$ , as indicated in (a). The black solid lines correspond to the TvNS solution [see Eqs. (2.36)-(2.38)]. (b) The data for  $R$  are shown in logarithmic scale to emphasize the power-law divergence for small  $\xi$ .

$N$  is the mean number of particles in the radial bin whose pressure is being computed.

The numerically obtained scaling functions  $R(\xi)$ ,  $V(\xi)$ ,  $E(\xi)$ , and  $P(\xi)$  are shown in Fig. 4.1–4.4 for initial number densities  $0.1$  and  $0.4$ . For each of the densities, four different times are shown. The data for the different times collapse onto one curve when plotted against  $\xi$ . The TvNS solution is shown in solid black line. Since the simulations correspond to a monoatomic gas, we set  $\gamma = 5/3$  in the TvNS solution.

The scaling function  $R(\xi)$  depends on the initial number density  $\rho_0$ , especially close to the shock front [see Fig 4.1(a)]. As  $\rho_0$  decreases, the discontinuity in density at the shock front increases, and it is possible that it may approach the theoretical result in the limit of infinite dilution. However, when compared with the entire range of  $\xi$ , the numerically obtained curves are very different from the TvNS solution. In particular, as shown in Fig. 4.1(b), the TvNS scaling function increases as a power law  $\xi^{9/2}$  for small  $\xi$  [as in Eq. (2.41)] with  $\gamma = 5/3$ , while the numerically obtained scaling function tends to a

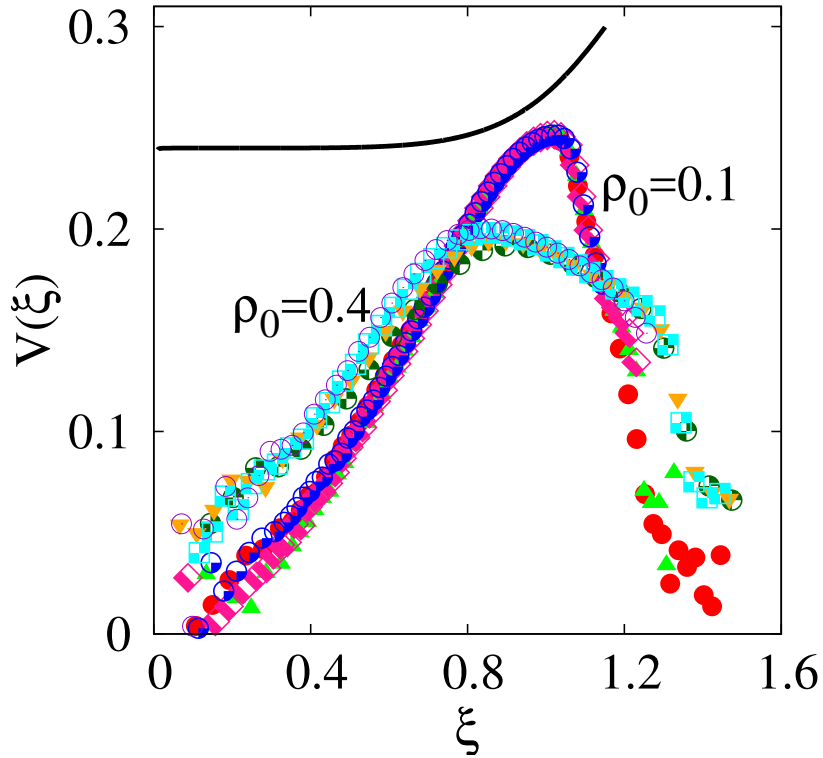


Figure 4.2: (a) The variation of the scaling function  $V(\xi)$  corresponding to non-dimensionalized velocity [see Eq. (4.2)] with scaled distance  $\xi$ . The data are shown for 2 different initial densities  $\rho_0 = 0.1$  and  $0.4$ . For  $\rho_0 = 0.1$ , the different times are  $t = 30000, 40000, 50000, 60000$ , and for  $\rho_0 = 0.4$ ,  $t = 5000, 10000, 20000, 30000$ , as indicated in Fig. 4.1(a). The black solid lines correspond to the TvNS solution [see Eqs. (2.36)-(2.38)].

non-zero constant.

The scaling function  $V$ , shown in Fig 4.2, increases linearly from zero, reaches a maximum and then decreases to its value at the shock front. The data for  $V$  from the simulations are again not consistent with the TvNS solution in which  $V$  is non-zero at  $\xi = 0$ , and then monotonically increases to its value at the shock front. Decreasing the ambient number density  $\rho_0$  shifts the numerical data further away from the TvNS solution for small  $\xi$ .

The scaling function  $E(\xi)$ , which measures the local velocity fluctuations, is shown in Fig 4.3(a). There is only a weak dependence on the number density  $\rho_0$ . From Fig 4.3(b), it can be seen that  $E$  diverges as a power law as  $\xi \rightarrow 0$ , with an exponent that we numerically estimate to be close to  $-2$ . The TvNS solution predicts that  $E$  diverges with decreasing

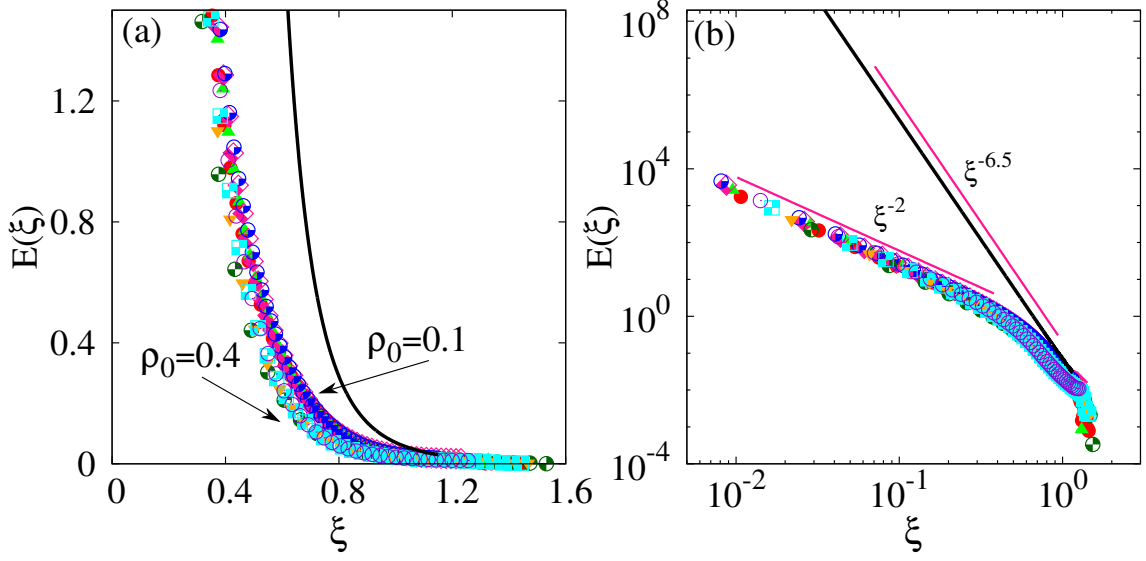


Figure 4.3: (a) The variation of the scaling function  $E(\xi)$  corresponding to non-dimensionalized temperature [see Eq. (4.2)] with scaled distance  $\xi$ . The data are shown for 2 different initial densities  $\rho_0 = 0.1$  and  $0.4$ . For  $\rho_0 = 0.1$ , the different times are  $t = 30000, 40000, 50000, 60000$ , and for  $\rho_0 = 0.4$ ,  $t = 5000, 10000, 20000, 30000$ , as indicated in Fig. 4.1(a). The black solid lines correspond to the TvNS solution [see Eqs. (2.36)-(2.38) and Eq. (4.4)]. The black solid lines correspond to the TvNS solution. (b) The data for  $E$  are shown in logarithmic scale to emphasize the power-law divergence for small  $\xi$ .

$\xi$  as  $E \sim \xi^{-13/2}$  [see Eq. (2.42)]. Again, the data from simulations are quantitatively different from the TvNS solution.

The dependence of the scaled pressure on  $\xi$  is shown in Fig 4.4(a). Unlike the other scaling functions, the data from simulations are much closer to the TvNS solution. In particular, both data diverge as  $\xi^{-2}$  for small  $\xi$  [see Fig 4.4(b)]. Also, as the number density  $\rho_0$  is decreased, the data tends towards the analytical solution, though it is not possible to extrapolate the data to  $\rho_0 = 0$  with the current data.

In summary, the TvNS solution is inadequate to describe the numerical data. Also, the data from simulations show that the results depend on  $\rho_0$ . On the other hand the TvNS solution is independent of  $\rho_0$ . There could be multiple plausible reasons for the observed differences. One is that the simulations are performed for hard spheres, while the TvNS solution is for the ideal gas. In the hard sphere simulations, there is an upper bound for the local number density, while there is no such bound in the ideal gas. This particularly

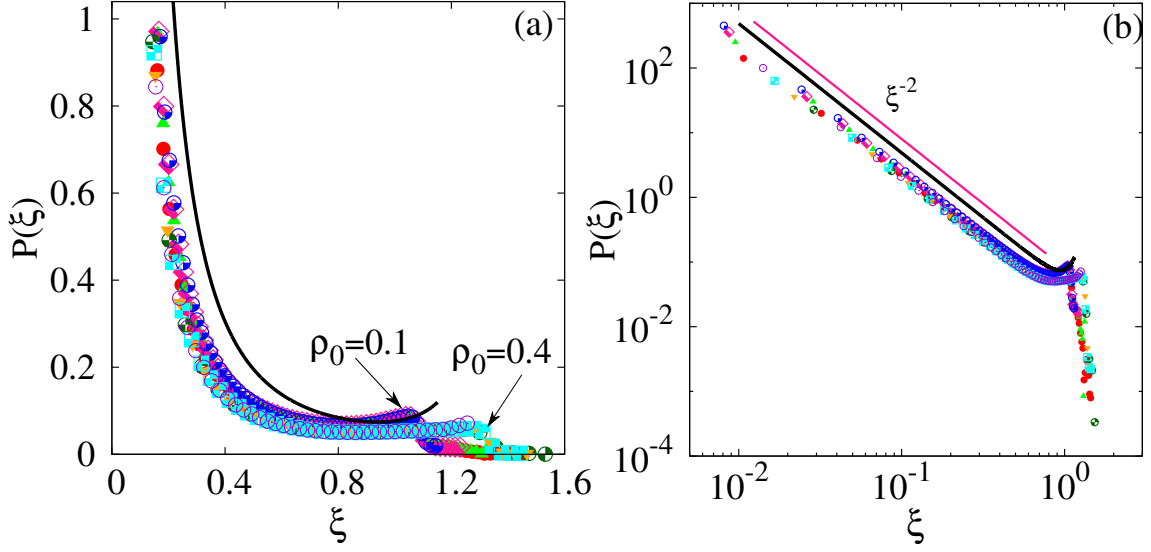


Figure 4.4: (a) The variation of the scaling function  $P(\xi)$  corresponding to non-dimensionalized pressure [see Eq. (4.2)] with scaled distance  $\xi$ . The data are shown for 2 different initial densities  $\rho_0 = 0.1$  and  $0.4$ . For  $\rho_0 = 0.1$ , the different times are  $t = 30000, 40000, 50000, 60000$ , and for  $\rho_0 = 0.4$ ,  $t = 5000, 10000, 20000, 30000$ , as indicated in (a). The black solid lines correspond to the TvNS solution [see Eqs. (2.36)-(2.38)]. (b) The data for  $P$  are shown in logarithmic scale to emphasize the power-law divergence for small  $\xi$ .

becomes significant near the shock front where the density becomes high irrespective of the initial density. Secondly, the medium through which shock is propagating is inherently a system out of equilibrium, and the assumption of local equilibrium in the TvNS solution may be incorrect.

In the following, we test these assumptions. First, we incorporate effects of explosion in the hard sphere model into the TvNS solution by replacing the EOS for an ideal gas with a virial expansion for the hard sphere gas. Second, we test the assumption of local equilibrium.

### 4.3 Shock propagation in a hard sphere gas

The EOS and the free energy of the hard sphere gas may be expressed as a virial expansion:

$$\frac{p}{k_B T \rho} = 1 + \sum_{n=2}^{\infty} B_n \rho^{n-1}, \quad (4.6)$$

$$\frac{F(N, V, T)}{N k_B T} = \ln(\Lambda^d \rho) - 1 + \sum_{n=2}^{\infty} B_n \frac{\rho^{n-1}}{n-1}, \quad (4.7)$$

where  $p$  is pressure,  $T$  is temperature,  $k_B$  is Boltzmann constant,  $\rho$  is number density,  $B_n$  is the  $n$ th virial coefficient,  $F$  is the free energy, and  $\Lambda = h / \sqrt{2\pi m k_B T}$  is the thermal wavelength.

From Eqs. (4.6) and (4.7), the entropy is,

$$s = k_B \left[ \frac{d}{2} - [\ln(\Lambda^d \rho) - 1] - \sum_{n=2}^{\infty} \frac{\rho^{n-1}}{n-1} \left( B_n + T \frac{dB_n}{dT} \right) \right]. \quad (4.8)$$

For a hard sphere gas, the virial coefficients are independent of the temperature and hence  $\frac{dB_n}{dT} = 0$ . This simplifies the internal energy per particle as  $u = \frac{d}{2} k_B T$ . Thus, the enthalpy per particle is,

$$w = k_B T \left( 1 + \frac{d}{2} + \sum_{n=2}^{\infty} B_n \rho^{n-1} \right). \quad (4.9)$$

Now, the set of hydrodynamic equations describing the propagation of the shock in the ideal gas [see Eqs. (2.16)-(2.18)], have to be modified. It is more convenient to work in terms of the local temperature rather than the local pressure. So we consider Eq. (2.15) for the conservation of entropy. In this chapter, we concentrate on three-dimensional case, so  $d = 3$ . Replacing  $p$  in Eq. (2.17) with the virial equation in Eq. (4.6) and  $s$  in Eq. (2.15)

with the Eq. (4.8), the equations of motion are modified to

$$\partial_t \rho + \partial_r(\rho v) + 2r^{-1}\rho v = 0, \quad (4.10)$$

$$\partial_t v + v\partial_r v + k_B T \left(1 + \sum_{n=2}^{\infty} n B_n \rho^{n-1}\right) \partial_r \ln \rho + k_B T \left(1 + \sum_{n=2}^{\infty} B_n \rho^{n-1}\right) \partial_r \ln T = 0, \quad (4.11)$$

$$(\partial_t + v\partial_r) \frac{3 \ln T}{2} - \left(1 + \sum_{n=2}^{\infty} B_n \rho^{n-1}\right) (\partial_t + v\partial_r) \ln \rho = 0. \quad (4.12)$$

Transforming to dimensionless variables using Eqs. (4.2), the hydrodynamic equations reduce to

$$\begin{aligned} \left(V - \frac{2}{5}\right) \xi R \frac{dV}{d\xi} + \xi \frac{d}{d\xi} \left[ ER \left(1 + \sum_{n=2}^{\infty} B_n \rho_0^{n-1} R^{n-1}\right) \right] - RV + RV^2 \\ + 2RE \left[1 + \sum_{n=2}^{\infty} B_n \rho_0^{n-1} R^{n-1}\right] = 0, \end{aligned} \quad (4.13)$$

$$\left(V - \frac{2}{5}\right) \xi \frac{dR}{d\xi} + \xi R \frac{dV}{d\xi} + 3RV = 0, \quad (4.14)$$

$$-\left(1 + \sum_{n=2}^{\infty} B_n \rho_0^{n-1} R^{n-1}\right) \left(V - \frac{2}{5}\right) \frac{\xi}{R} \frac{dR}{d\xi} + \frac{3}{2} \left(V - \frac{2}{5}\right) \frac{\xi}{E} \frac{dE}{d\xi} + 3(V - 1) = 0. \quad (4.15)$$

The Rankine-Hugoniot boundary conditions at the shock front  $\xi_f$  are now

$$\begin{aligned} \frac{1}{R(\xi_f)} \left[1 + \frac{3}{1 + \sum_{n=2}^{\infty} B_n \rho_0^{n-1} R(\xi_f)^{n-1}}\right] &= 1, \\ V(\xi_f) &= \frac{6}{5} \frac{1}{R(\xi_f) \left[1 + \sum_{n=2}^{\infty} B_n \rho_0^{n-1} R(\xi_f)^{n-1}\right]}, \\ E(\xi_f) &= \frac{1}{3} V(\xi_f)^2. \end{aligned} \quad (4.16)$$

For a given  $\xi_f$ , Eqs. (4.13)-(4.15) with the boundary conditions in Eqs. (4.16) may be solved numerically.  $\xi_f$ , as before, is determined by the condition that total energy is conserved, which in terms of the scaling functions is

$$4\pi \int_0^{\xi_f} R(\xi) \left[ \frac{V^2(\xi)}{2} + \frac{3}{2} E(\xi) \right] \xi^4 d\xi = 1, \quad (4.17)$$

$n$	$B_n$
2	$\frac{2\pi}{3}$
3	$\frac{5}{8}B_2^2$
4	$\left[ \frac{2707}{4480} + \frac{219\sqrt{2}}{2240\pi} - \frac{4131}{4480} \frac{\arccos[1/3]}{\pi} \right] B_2^3$
5	$0.110252B_2^4$
6	$0.03888198B_2^5$
7	$0.01302354B_2^6$
8	$0.0041832B_2^7$
9	$0.0013094B_2^8$
10	$0.0004035B_2^9$

Table 4.1: The values of the virial coefficients  $B_n$  for the hard sphere gas in three dimensions. The data are taken from Ref. [71].

which is same as Eq. (2.35) with  $\gamma = 5/3$  and  $P = RE$ .

For the hard sphere gas in three dimensions, the virial coefficients  $B_n$  are known analytically for up to  $n = 4$  and through Monte Carlo simulations up to  $n = 10$  [71]. These are tabulated in Table 4.1.

From the hydrodynamic equations as well as the boundary conditions, it is clear that the initial density  $\rho_0$  now affects the results, since it explicitly appears in the equations. The limit  $\rho_0 \rightarrow 0$  in these equations should reproduce the TvNS solution. We thus expect that there could be significant deviations for larger densities. We now compare the results for the solution for the hydrodynamic equation with virial EOS for hard sphere gas with that for the ideal gas as well as those obtained from simulations.

In Figs. 4.5 and 4.6, the TvNS solution with virial EOS is denoted by lines while the simulation data are shown by points for  $\rho_0 = 0.1$  and  $\rho_0 = 0.4$  respectively. We first focus on the effect of truncating the virial EOS by including only the first  $n$  virial terms. We find that the scaling functions for density, velocity, temperature, and pressure for  $n = 6, 8, 10$  are indistinguishable from each other for both densities [see Figs. 4.5 and 4.6], showing that errors introduced by truncating the EOS at  $n = 10$  are negligible. Second, we observe that as  $n$  or  $\rho_0$  increases, the discontinuities at the shock front decreases, and the position



of the shock front  $\xi_f$  increases. Third, and more importantly, the inclusion of virial EOS does not alter the exponents of the power law divergence of the scaling functions at small  $\xi$ . Also, the exponents are independent of  $\rho_0$ . For high densities, there are qualitative changes induced by including virial EOS. For example, the scaling function for velocity changes from monotonically increasing for ideal gas to monotonically decreasing for the virial EOS [see Fig. 4.6(b)].

Near the shock front, in comparison to the ideal gas EOS, we find that the virial EOS does a better job of describing the scaling functions obtained from simulations. For the density scaling function, the discontinuity at the shock front is better captured by the virial EOS for both densities [see Figs. 4.5(a) and 4.6(a)]. For the velocity scaling function, the virial EOS matches with the simulation data close to the shock front for  $\rho_0 = 0.1$  [see Fig. 4.5(b)], and captures the correct trend for  $\rho_0 = 0.4$  [see Fig. 4.6(b)]. For both temperature [see Figs. 4.5(c) and 4.6(c)] and pressure [see Figs. 4.5(d) and 4.6(d)], the scaling functions obtained from virial EOS are closer to the simulation data than the ideal gas EOS.

Away from the shock front, the power-law behavior of the scaling function remain unchanged with the inclusion of the virial EOS. This is because near the shock center, the gas is dilute, and the virial EOS tends towards the ideal gas law. Thus, as for the TvNS theory discussed in Sec. 4.2, the modified theory is incapable to describe the simulation data [see insets of Figs. 4.5 and 4.6].

The discontinuity at the shock front is plotted in Fig 4.7. For more realistic virial EOS, the discontinuities deviate further away from the ideal gas case with inclusion of more terms, though the values converge by  $n = 8$ . The deviations are more for larger ambient densities.

Thus, we conclude that while replacing the ideal gas assumption in the TvNS solution with the virial EOS for the hard sphere gas introduces some dependence on the initial density  $\rho_0$ , it fails to capture the strong deviations from the TvNS solution that is observed

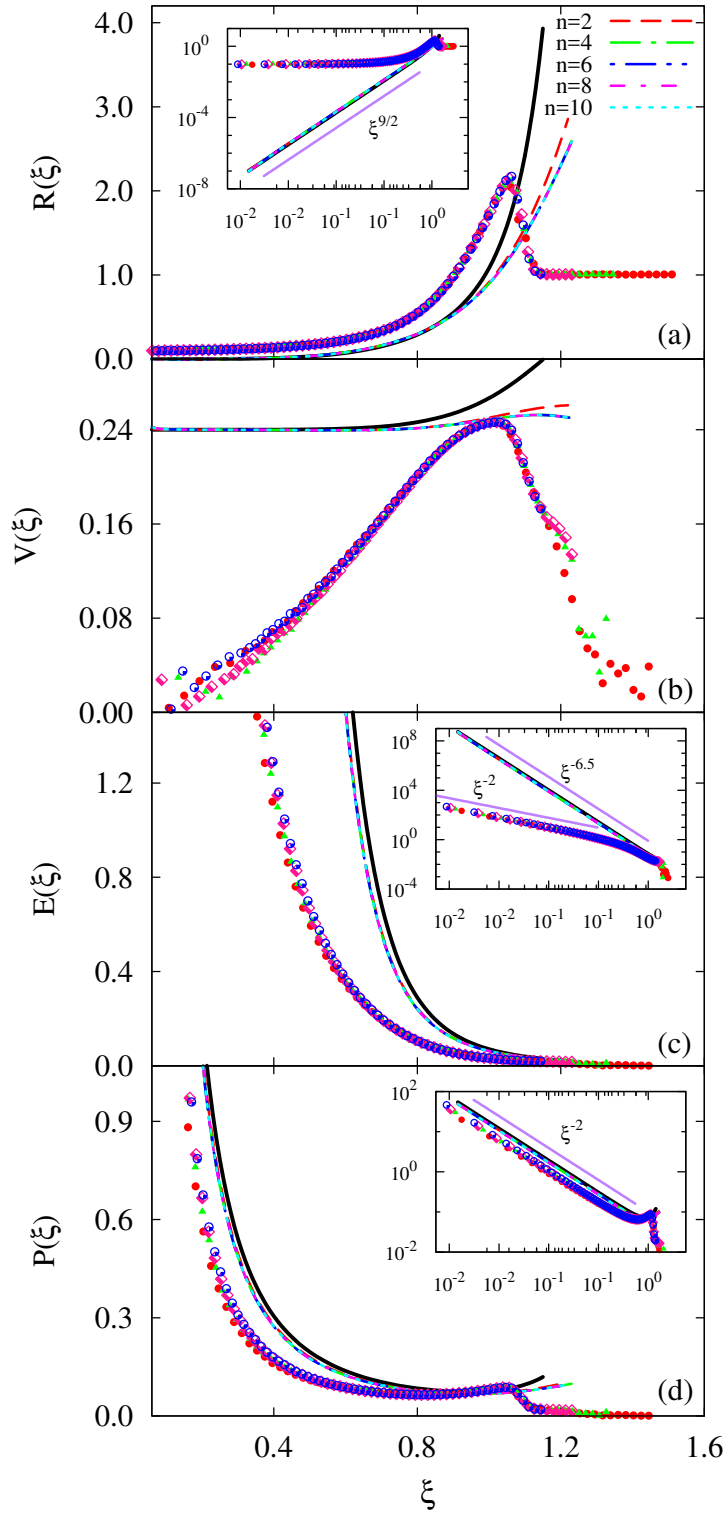


Figure 4.5: The scaling functions (a)  $R(\xi)$ , (b)  $V(\xi)$ , (c)  $E(\xi)$ , and (d)  $P(\xi)$  corresponding to density, velocity, temperature and pressure respectively versus  $\xi$  for ambient density  $\rho_0 = 0.1$  is compared with the theoretical solution for the hydrodynamic equations with virial EOS for the hard sphere gas. The simulation data (represented by points) correspond to four different times with keys as shown in Fig 4.1(a). The lines represent the virial EOS solution with the virial expansion truncated at  $n = 2, 4, 6, 8, 10$ . Black solid curve represents the case of ideal gas. The inset shows the plots on a log-log scale, accentuating the small  $\xi$  behavior.

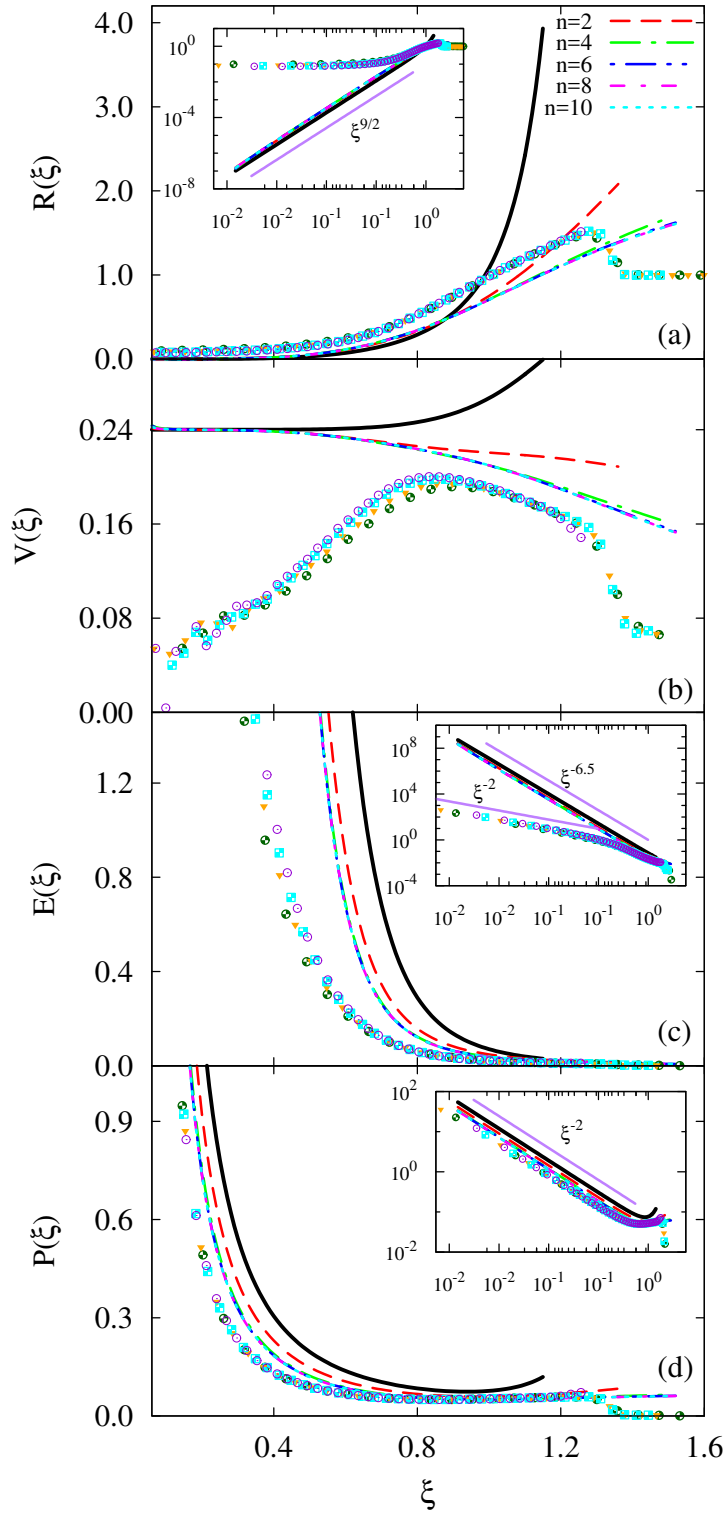


Figure 4.6: The scaling functions (a)  $R(\xi)$ , (b)  $V(\xi)$ , (c)  $E(\xi)$ , and (d)  $P(\xi)$  corresponding to density, velocity, temperature and pressure respectively versus  $\xi$  for ambient density  $\rho_0 = 0.4$  is compared with the theoretical solution for the hydrodynamic equations with virial EOS for the hard sphere gas. The simulation data (represented by points) correspond to four different times with keys as shown in Fig 4.1(a). The lines represent the virial EOS solution with the virial expansion truncated at  $n = 2, 4, 6, 8, 10$ . Black solid curve represents the case of ideal gas. The inset shows the plots on a log-log scale, accentuating the small  $\xi$  behavior.

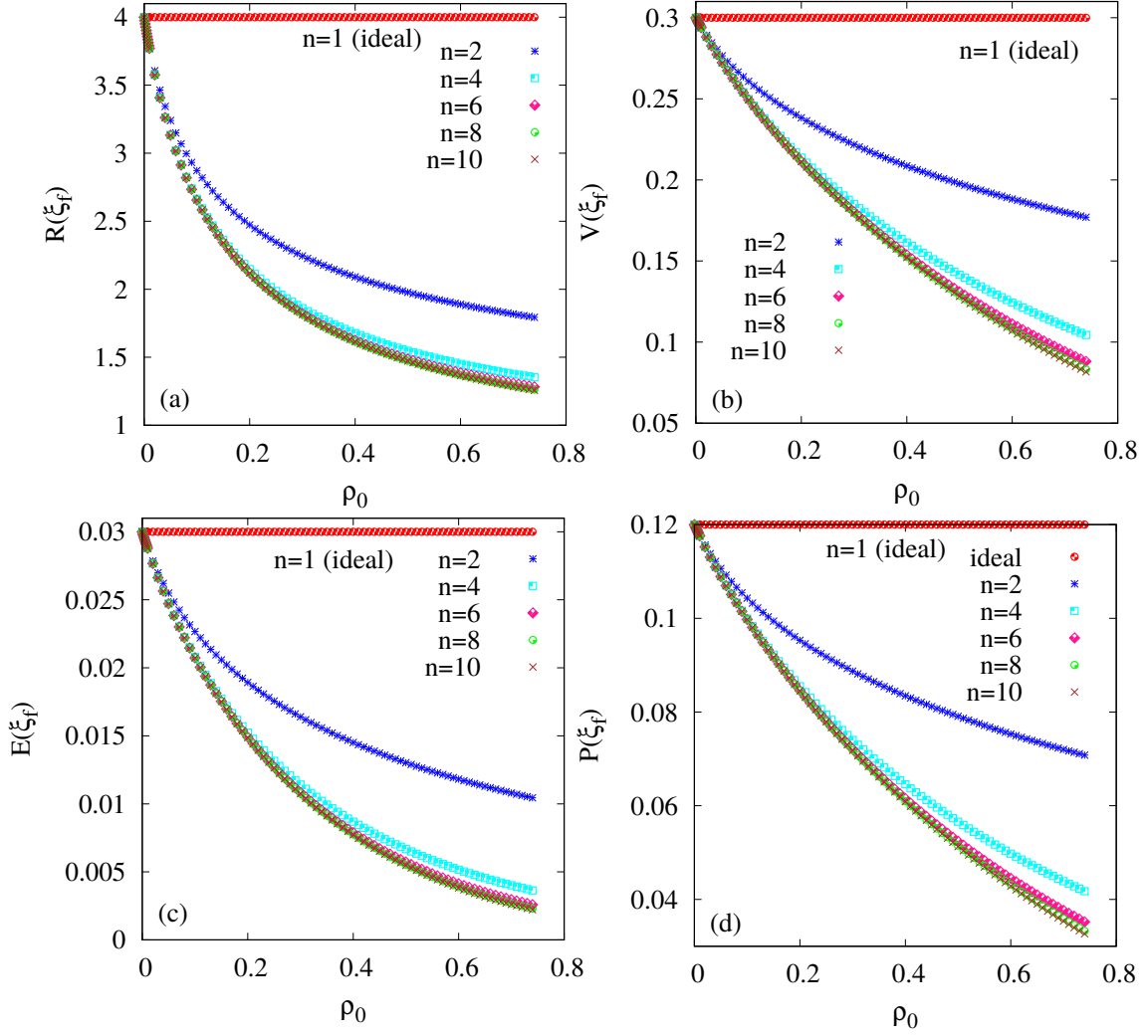


Figure 4.7: The scaling functions corresponding to density, velocity, temperature, and pressure at the shock front, denoted by (a)  $R(\xi_f)$ , (b)  $V(\xi_f)$ , (c)  $E(\xi_f)$ , and (d)  $P(\xi_f)$  respectively, versus the ambient density  $\rho_0$ . The data are for the virial EOS solution with the virial expansion truncated at  $n = 2, 4, 6, 8, 10$ .

in the event-driven simulations.

## 4.4 Local Equilibrium

We now numerically check the assumption of local equilibrium in the TvNS solution. First, we check whether the EOS of a hard sphere gas is obeyed. Second, we check whether the thermal energy is locally equipartitioned equally in all three directions. Finally, we calculate the skewness and kurtosis of the distribution of velocity fluctuations to

check the deviation from a gaussian.

#### 4.4.1 Equation of state

A central assumption of the TvNS solution is that the local pressure, density and temperature are not independent, but related to each other through an EOS, which is assumed to be that of the ideal gas. To test the assumption of EOS, we measure the local thermodynamic quantities and check whether they obey the hard sphere virial EOS. To do so, we measure the ratio

$$\chi(n) = \frac{P(\xi)}{E(\xi)R(\xi) \left[ 1 + \sum_{k=2}^n B_k \rho_0^{k-1} R(\xi)^{k-1} \right]}, \quad (4.18)$$

where  $n$  is the number of terms retained in the virial expansion [ $n = 1$  corresponds to ideal gas]. For large  $n$ , if  $\chi \approx 1$ , then we conclude that the virial EOS is obeyed, and the assumption of EOS is justified.

The dependence of  $\chi(n)$  on  $\xi$  for  $n = 2, 4, 6, 8, 10$  is shown in Fig. 4.8 for the two ambient densities, for two different times. While for small  $n$ , there is deviation from one near the shock front, quite remarkably, as  $n$  increases,  $\chi(n)$  fluctuates about 1 for all  $\xi$ . This clearly shows that the assumption of an EOS is quite justified. There is an ambiguity about whether we define temperature using the full velocity fluctuations, i.e.,  $T = \frac{1}{3} (\langle \delta v_r^2 \rangle + \langle \delta v_\perp^2 \rangle)$  or by only considering the radial or transverse components. To show that the evidence of EOS is not dependent on this choice, consider Fig 4.9 where  $\chi(10)$  is shown for both  $T_r$  [based on radial component] and  $T_\perp$  [based on transverse component], where

$$T_r = \langle (\delta v_r)^2 \rangle, \quad (4.19)$$

$$T_\perp = \frac{1}{2} \langle (\delta v_\perp)^2 \rangle, \quad (4.20)$$

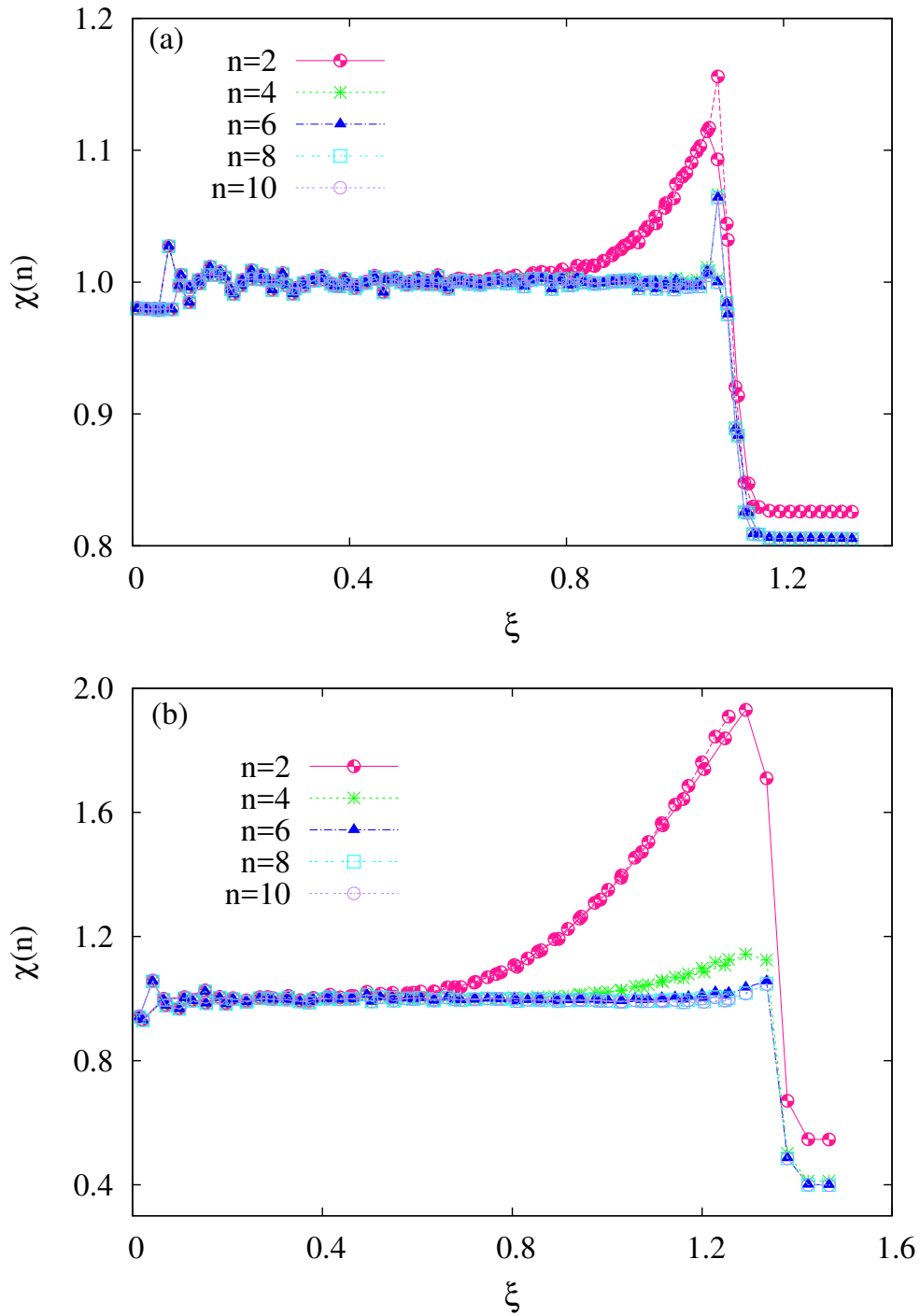


Figure 4.8: The variation of  $\chi(n)$  [see Eq. (4.18)] with  $\xi$  for  $n = 2, 4, 6, 8, 10$ . The data in (a) are for times 40000 and 60000 with ambient number density  $\rho_0 = 0.1$  and in (b) are for times 10000 and 30000 with ambient number density  $\rho_0 = 0.4$ . For large  $n$ ,  $\chi(n)$  fluctuates about 1 in both the case.

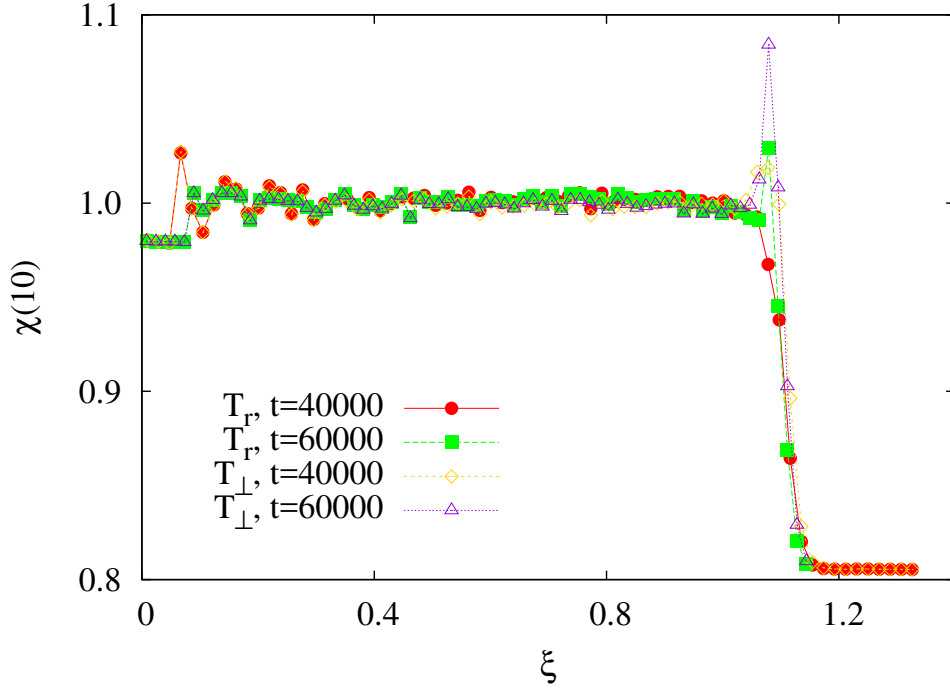


Figure 4.9: The variation of  $\chi(10)$  with  $\xi$ , where the temperature in Eq. (4.18) is replaced by  $T_r$  or  $T_\perp$  defined through the radial and perpendicular components of the velocity fluctuations. The data are for times 40000 and 60000 and ambient density  $\rho_0 = 0.1$ .

where the factor of 2 accounts for the two degrees of freedom in the  $\theta$ - $\phi$  directions and,

$$\langle \delta v_r^2 \rangle = \langle (v_r - \langle v_r \rangle)^2 \rangle, \quad (4.21)$$

$$\begin{aligned} \langle \delta v_\perp^2 \rangle &= \langle (v_\perp - \langle v_\perp \rangle)^2 \rangle \\ &= \langle v_\perp^2 \rangle. \end{aligned} \quad (4.22)$$

Clearly, the results are independent of the choice, except very close to the shock front.

#### 4.4.2 Equipartition

We check whether the thermal energy is equipartitioned equally in all three directions by measuring the ratio

$$\zeta = \frac{\langle \delta v_r^2 \rangle}{\langle \delta v_\perp^2 \rangle / 2}, \quad (4.23)$$

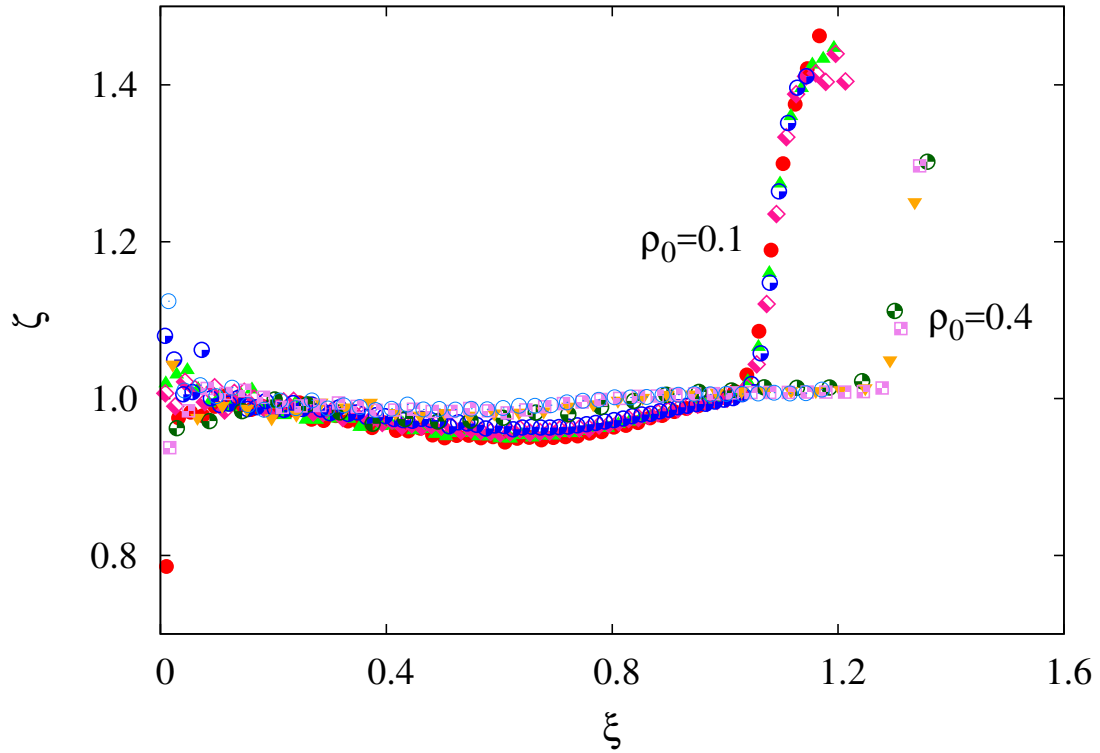


Figure 4.10: The variation of  $\zeta$ , the ratio of energies in the radial and  $\theta$ - $\phi$  directions [see Eq. (4.23)] with the scaled distance  $\xi$ . The data is for four different times with keys as in Fig 4.1(a), for two ambient densities  $\rho_0 = 0.1$  and  $0.4$ . Away from the shock front,  $\zeta \approx 1$ .

where  $\delta v_r$  and  $\delta v_\perp$  are the velocity fluctuations in the radial and transverse  $\theta$ - $\phi$  directions respectively. The factor of 2 accounts for the two degrees of freedom in the  $\theta$ - $\phi$  directions. If the thermal energy is equipartitioned, then  $\zeta = 1$ . Fig. 4.10 shows the variation of  $\zeta$  with  $\xi$  for different times. The data for different times collapse on to a single curve. Away from the shock front,  $\zeta \approx 1$  showing equipartition. However, near the shock front,  $\zeta > 1$ , corresponding to excess thermal energy in the radial direction.



### 4.4.3 Skewness and Kurtosis

To quantify the deviation from gaussianity, we measure the kurtosis  $\kappa$ , and skewness  $S$  of the probability distribution for the velocity fluctuations:

$$\kappa_r = \frac{\langle \delta v_r^4 \rangle}{3\langle \delta v_r^2 \rangle^2}, \quad (4.24)$$

$$\kappa_{\perp} = \frac{\langle \delta v_{\perp}^4 \rangle}{2\langle \delta v_{\perp}^2 \rangle^2}, \quad (4.25)$$

$$S = \frac{\langle \delta v_r^3 \rangle}{\langle \delta v_r^2 \rangle^{3/2}}, \quad (4.26)$$

where,

$$\langle \delta v_r^4 \rangle = \langle (v_r - \langle v_r \rangle)^4 \rangle, \quad (4.27)$$

$$\langle \delta v_r^3 \rangle = \langle (v_r - \langle v_r \rangle)^3 \rangle, \quad (4.28)$$

and in perpendicular direction,

$$\begin{aligned} \langle \delta v_{\perp}^4 \rangle &= \langle (v_{\perp} - \langle v_{\perp} \rangle)^4 \rangle \\ &= \langle v_{\perp}^4 \rangle. \end{aligned} \quad (4.29)$$

In the simulation, we find out the above quantities in each bin (radial binning). Deviation of kurtosis from 1 shows non-gaussian behavior. Likewise, a non-zero skewness shows that the distribution is not symmetric. The variation of  $\kappa_r$  and  $\kappa_{\perp}$  with  $\xi$  is shown in Fig. 4.11 (a) and (b) respectively. While the data for different times collapse onto one curve,  $\kappa_r$  and  $\kappa_{\perp}$  deviate significantly from 1 for almost all  $\xi$ , showing a lack of local equilibrium. For the higher density  $\rho_0 = 0.4$ ,  $\kappa_r$  and  $\kappa_{\perp}$  are close to one near the shock front. Skewness  $S$  also provides a strong evidence for deviation from gaussianity and a lack of local equilibrium. From the variation of  $S$  with  $\xi$ , as shown in Fig. 4.11 (c), it is clear that it is positive for all values of  $\xi$ . Thus, the distribution is clearly asymmetric.

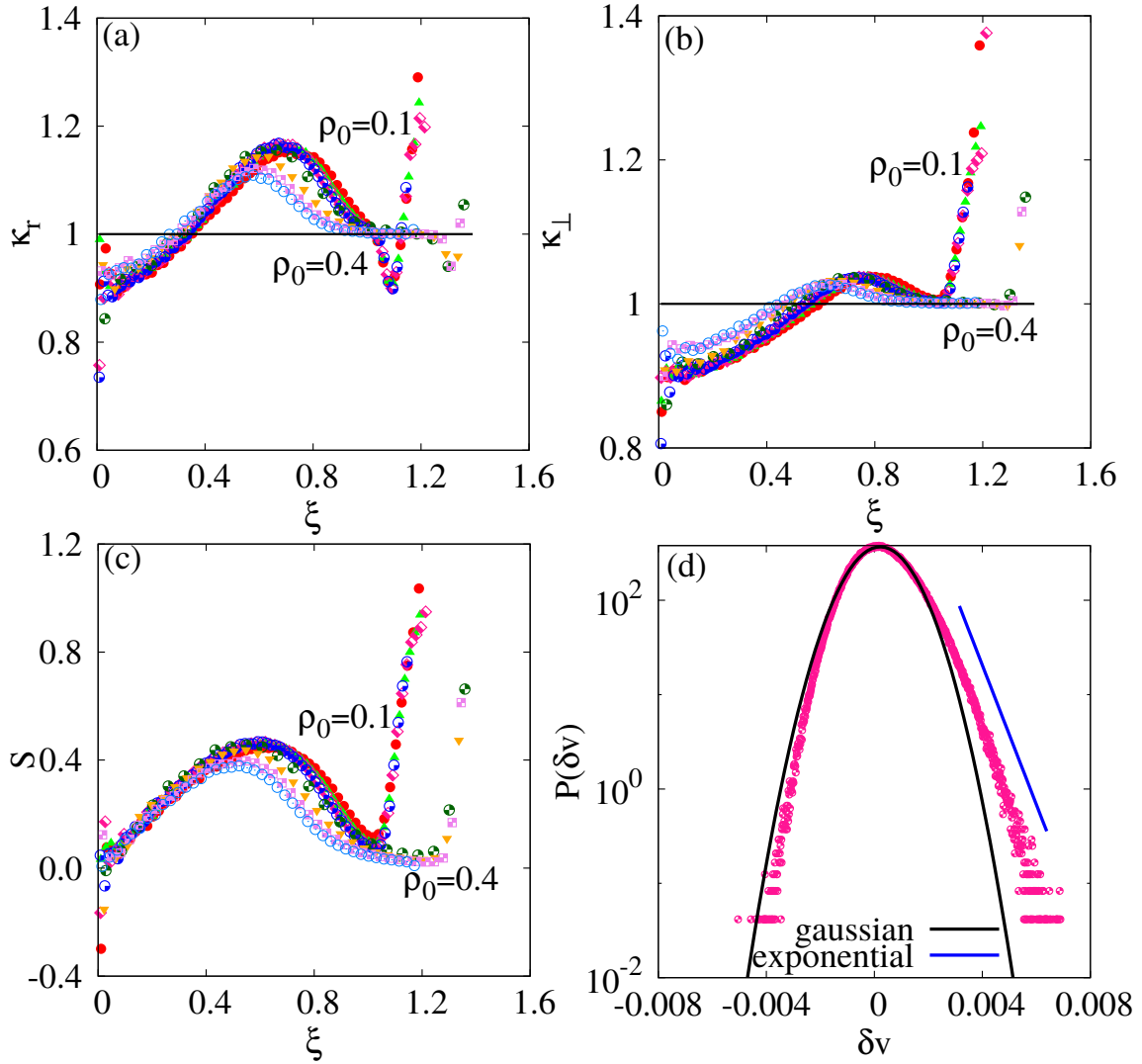


Figure 4.11: The variation with scaled distance  $\xi$  of (a) the kurtosis  $\kappa_r$  for the radial velocity fluctuations [see Eq. (4.24)]. (b) the kurtosis  $\kappa_\perp$  for the velocity fluctuations in the  $\theta$ - $\phi$  direction [see Eq. (4.25)] and (c) skewness  $S$  for the radial velocity fluctuations [see Eq. (4.26)]. The black solid line in (a) and (b) are reference lines of 1, corresponding to gaussianity. The data are for  $\rho_0 = 0.1$  and  $\rho_0 = 0.4$  and for four different times with keys as in Fig 4.1(a). (d) The distribution of the radial velocity fluctuations  $P(\delta v)$  measured at  $r = 61.5$ ,  $t = 30000$  and  $\rho_0 = 0.4$ , corresponding to  $\xi = 0.58$ . The black solid curve represents the gaussian distribution fitted to the data near zero. The blue solid line is an exponential and a guide to the eye.

Note that in the  $\theta$ - $\phi$  directions, due to symmetry, the skewness is zero.

The skewness of the distribution may be directly seen by examining the full probability distribution  $P(\delta v_r, r, t)$  for the fluctuations in the radial velocity. The distribution for a fixed time  $t$  and fixed radial distance  $r$ , corresponding to  $\xi = 0.58$  is shown in Fig 4.11 (d). This corresponds to a region away from the shock front where the skewness in Fig. 4.11(c) is non-zero. It can be seen from the figure that the distribution deviates from the gaussian distribution and is skewed towards the larger positive fluctuations. We find that the data are consistent with an exponential decay for large positive fluctuations.

## 4.5 Effect of heat conduction

The numerically obtained temperature profile shows that there is a temperature gradient in the problem. In the presence of a gradient, the heat flux term may become important. But the effect of heat conduction has been neglected in the TvNS theory. The divergence of temperature for small  $\xi$  in the TvNS solution may be regularized by introducing heat conduction [11, 30, 31]. When the flow is made non-adiabatic, the conservation laws for mass and momentum do not change [see Eqs. (2.16) and (2.17)]. However, the conservation of energy [see Eq. (2.18)] is now modified to [35, 11, 30, 31],

$$\rho [\partial_t e + v \partial_r e] - T [\partial_t \rho + v \partial_r \rho] + \frac{1}{r^2} \partial_r (r^2 q_r) = 0, \quad (4.30)$$

where  $e$  is the internal energy and  $q_r$  is the heat flux in the radial direction, given by

$$q_r = -\lambda \nabla T = -\lambda \partial_r T, \quad (4.31)$$

where  $\lambda$  is the heat conductivity. Within kinetic theory,  $\lambda$  depends on temperature as

$$\lambda = \sqrt{\frac{2k_B^3 T}{\pi^3 m \sigma^4}}, \quad (4.32)$$

where  $\sigma$  is the diameter of the particles and  $m$  is the mass of the particles. The Rankine-Hugoniot condition describing the mass flux and momentum flux are same as described in Eqs. (2.22) and (2.23). The energy flux gives,

$$e_f + \frac{p_f}{\rho_f} + \frac{1}{2}(v_f - D)^2 - \frac{\bar{q}_f}{\rho_0 D} = \frac{1}{2}D^2, \quad (4.33)$$

where  $\bar{q}_f$  is the heat flux at the shock front. In connection with Eq. (2.25), Eq. (4.33) can be written as,

$$3v_f(D - v_f) = v_f^2 + \frac{2\bar{q}_f}{\rho_0 D}. \quad (4.34)$$

Equation (4.30) is converted to the ODE by dimensional analysis given in Eqs. (4.2),

$$\begin{aligned} & \frac{3}{2} \left[ V - \frac{2}{5} \right] \xi R \frac{dE}{d\xi} - \left[ V - \frac{2}{5} \right] \xi E \frac{dR}{d\xi} + 3RE(V - 1) \\ & + \frac{C}{\xi t^{2/5}} \left[ 8E^{3/2} 8\sqrt{E}\xi \frac{dE}{d\xi} + \frac{1}{2\sqrt{E}} \left( \xi \frac{dE}{d\xi} \right)^2 + \sqrt{E}\xi^2 \frac{d^2E}{d\xi^2} \right] = 0, \end{aligned} \quad (4.35)$$

where  $\rho_0$  has been absorbed to the quantity  $C$ . In the limit  $r, t \rightarrow \infty$ , keeping  $\xi$  fixed, it is easy to see that the ratio of the heat conduction term [last term in Eq. (4.35)] to any of the other terms decreases to zero as  $t^{-2/5}$ . Thus, this term is irrelevant in the scaling limit. However, one may take the limiting case of switching on a heat conduction term with a small coefficient, and determine the limit of the scaling functions as this coefficient tends to zero. The boundary condition of no heat flux at the heat center [11, 30, 31] automatically ensures that the gradients in temperatures are set to zero, or equivalently the scaling function  $E \sim \xi^{-2}$ , as seen in the simulations. Thus, the results for the scaling functions obtained by first taking the scaling limit at the level of the hydrodynamics equations, or by taking the scaling limit after solving the hydrodynamic equations with heat conduction may not be the same. Whether the latter limit reproduces quantitatively the results of the simulations, requires a detailed numerical solution of the hydrodynamic equations, which is beyond the scope of this thesis. Note that Eq. (4.35) was derived under the assumption

that  $\lambda \propto T^{1/2}$ . However, if it is imposed that heat conduction term survives in the scaling limit of  $r \rightarrow \infty, t \rightarrow \infty$ , then one obtained the condition  $\lambda \propto T^{1/6}$  [11].

## 4.6 Sonic line

In this section, we check an implicit assumption of the TvNS theory. In the classic solution of a shock, the flow velocity is subsonic within the blast and supersonic when compared to the ambient gas into which the shock is expanding. The subsonic flow results in perturbations relaxing quickly. On the other hand, if there are regions where the flow is supersonic, then the asymptotic self similar solution may not be reached. To check whether this assumption is valid both within the event-driven simulations as well as the TvNS theory modified by the virial EOS, we follow closely the analysis of Ref. [17].

Consider the local sound velocity,

$$c(r, t) = \sqrt{\frac{\gamma p(r, t)}{\rho(r, t)}}. \quad (4.36)$$

Since a perturbation results in an acoustic wave (heat waves have been ignored), the energy carrying perturbation will have a maximal speed  $v(r, t) + c(r, t)$ , where  $v(r, t)$  is the local flow velocity. On the other hand, the phase velocity is the geometric speed at  $r$  and is given by  $\frac{r}{r_f} \frac{dr_f}{dt}$ , where  $r_f$  is the position of the shock front. Since  $r_f \propto t^{2/5}$ , we obtain  $\frac{dr_f}{dt} = \frac{2r_f}{5t}$ , such that the phase velocity is  $\frac{2r}{5t}$ . For the TvNS assumption to hold, the phase velocity should be less than the maximal speed  $v(r, t) + c(r, t)$ . This may be checked by plotting the scaled sound velocity  $C(\xi) = tc/r$  as a function of scaled flow velocity  $V(\xi) = tv/r$ , and compare the data with sonic line

$$\frac{5}{2}V + \frac{5}{2}C = 1. \quad (4.37)$$

If the  $C - V$  plot stays above this line, then perturbations are faster than phase velocity,

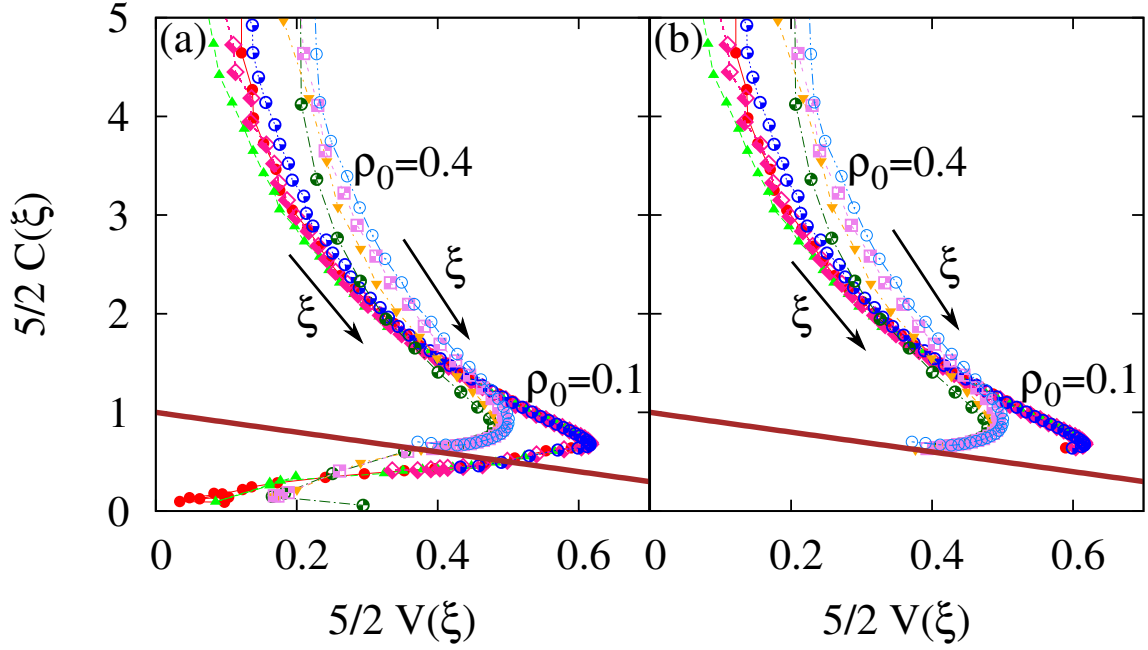


Figure 4.12: The parametric plot of sound velocity( $C$ )-flow velocity( $V$ ). The data are from simulations. The solid reference line represents the sonic line [see Eq. (4.37)]. The arrows indicate the direction of increasing  $\xi$ . (a) The full data. (b) Reduced data, where the data beyond the shock front have been removed. The data are for four different times with keys as in Fig 4.1(a).

and is necessary for the validity of the TvNS solution.

The parametric plot of the scaled sound velocity with the scaled flow velocity, as obtained from simulations, is shown in Fig 4.12(a). While most of the data lies above the sonic line (shown as solid line), there is a region near the shock front where the data from simulation lies below the sonic line for both the two different ambient densities. However, the region that we find below the sonic line may be an artifact of the simulation. The data is obtained by averaging over different histories, each one having a slightly different shock front, resulting in a diffused shock front. To remove this ambiguity, we identify the value of  $\xi$  at which density (or pressure) reaches a maximum as the shock front. We remove the data beyond the shock wave, and plot this reduced data in Fig 4.12 (b). Here, we find that the entire plot lies above the sonic line. So, we conclude that our simulations are in the parameter range corresponding to strong shocks.

The same features may be observed for the theoretical TvNS solution with virial EOS.

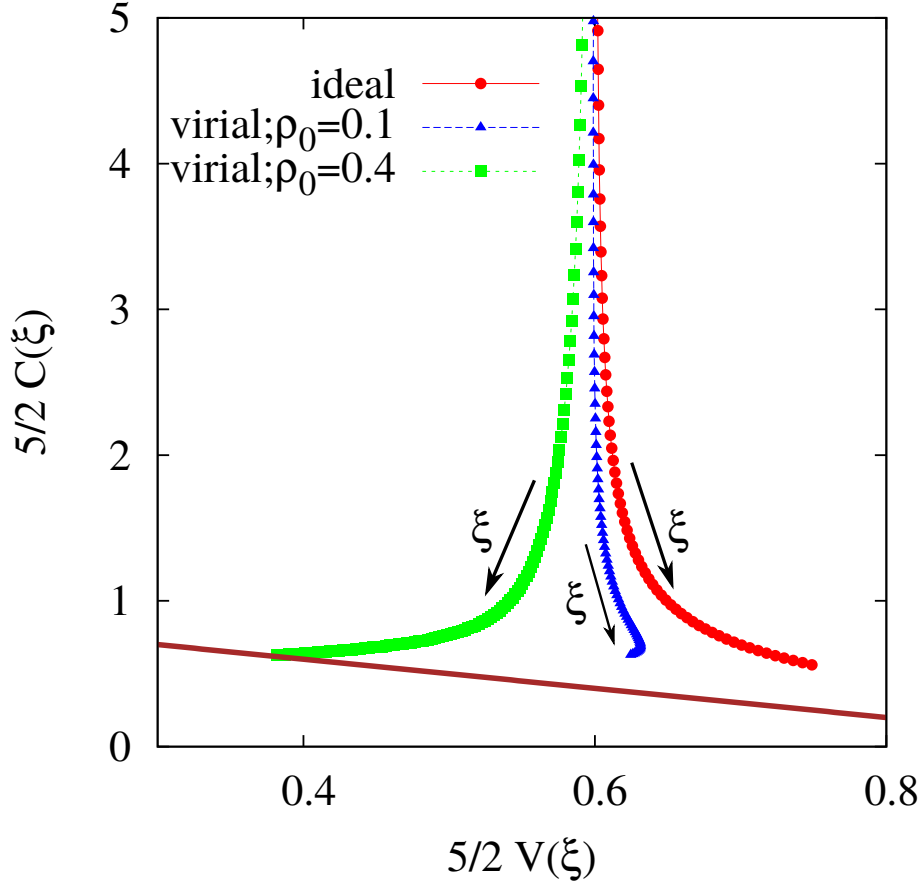


Figure 4.13: The parametric plot of sound velocity( $C$ )-flow velocity( $V$ ). The data are from TvNS solution with virial EOS truncated at the tenth virial coefficient. The solid reference line represents the sonic line [see Eq. (4.37)]. The arrows indicate the direction of increasing  $\xi$ .

The  $C$ - $V$  plot for the same is shown in Fig 4.13, where the virial EOS is truncated at the tenth virial coefficient. It can be seen that for the densities that we have considered, the  $C$ - $V$  parametric plot lies above the sonic line. Any higher ambient density would have resulted in the curve crossing the sonic line.

## 4.7 Conclusion and discussion

To summarize, in this chapter we compared the TvNS solution for the radial distribution of pressure, temperature, density, and flow velocity fields with results from large scale event-driven molecular dynamics simulations of hard spheres in three dimensions. We find that

the TvNS solution is inadequate to describe the numerical data well. In particular, the power law behavior away from the shock front for temperature and density have different exponents in the theory and simulations. In addition, the predictions for the flow velocity do not match the simulation results for all  $\xi$ .

The TvNS theory was modified by using a virial equation of state for the hard sphere gas instead of the ideal gas constitutive relation. We find that the hydrodynamic solution does not noticeably change beyond the inclusion of six virial coefficients. We restricted our analysis to the known ten virial coefficients. While inclusion of the more realistic virial equation of state modifies the theoretical predictions, especially near the shock front, it does not modify any of the exponents, and thus fails to describe the simulation data well.

We also checked the different assumptions of the TvNS theory. The assumption of local equilibrium is a key assumption of the TvNS solution. In particular, the main consequence of this assumption that goes into the theory is the existence of an equation of state for the gas. Though the numerics and theory do not agree for the scaling functions, surprisingly, the local pressure, temperature, and density satisfy the virial equation of state for the hard sphere gas very well, except for a small deviation near the shock front [see Fig. 4.8]. On the other hand, the radial velocity fluctuations are not gaussian, and is skewed towards positive fluctuations. This shows that local equilibrium is not attained. The hydrodynamic equations correspond to the collision less limit of the Boltzmann equation, and does not ensure equilibration. One way to understand the role of these skewed distributions would be to study a system where the local velocities are reassigned at a constant rate from a Maxwell-Boltzmann distribution with the local temperature, and ask whether any qualitative changes are observed. This is a promising area for future study.

Earlier molecular dynamics simulations in two dimensions [17] found that the simulations reproduce well the TvNS solution for low to medium densities, except for a small difference in the discontinuities at the shock front. Also, a slight discrepancy was observed near the shock center. When the number density of the ambient gas is high, the TvNS solution



did not describe well the data near the shock front [17]. This is contrary to our results in three dimensions where the TvNS solution does not match with simulation. The number densities considered in both the studies are similar, and thus we expect the results in this thesis to hold in two dimensions also. In the next chapter, we focus on understanding the reason for the different results that have been reported for two and three dimensions.



# Chapter 5

## **Shock propagation following an intense explosion: Detailed comparison between hydrodynamics and simulation in two dimensions**

### **5.1 Introduction**

This chapter starts from the results obtained in the previous chapter on shock propagation in a three-dimensional dilute elastic gas. In the previous chapter, we compared the celebrated TvNS solutions with the results from simulation of hard sphere gas. We showed that the simulation results in three dimensions are not in agreement with the hydrodynamic solutions. But in contrary to our results in three dimensions, in a recent study on the comparison of system in two dimensions, Barbier et. al. showed that the simulation results match with the TvNS solutions [17]. So in order to check the spatial dimensional dependence of the results, in this chapter, we compare the hydrodynamic solutions in two dimensions with the results from simulations in two dimensions.

In this chapter, we follow the same procedure as in chapter 4. In Sec. 5.2, we rewrite the hydrodynamic equations in two dimensions and compare the results obtained by solving the set of equations with the results from large scale event-driven MD simulations in two dimensions. We observe, there is a discrepancy between the TvNS results and simulation results. In the remaining sections, we check the assumptions made in the theory. In Sec. 5.3, we replace the ideal gas equation of state by the virial equation of state in the TvNS theory, and compare the solutions obtained by solving the modified sets of equations with the solutions from simulation. We find that the hydrodynamic results are modified, especially near the shock front, but still the power-law behavior can not be explained by the modified results of TvNS theory. Assumption of local equilibrium is checked in the Sec. 5.4. We justify the existence of an equation of state in the problem. We also check in this section, the equipartition of energy and prove that the energy is equipartitioned. The kurtosis and skewness are found to be not exist near the shock center. We summarize this chapter in Sec. 5.5. The content of this chapter is included in Ref. [72].

## **5.2 Simulation model and comparison with hydrodynamic solution in two dimensions**

In this section, we give the hydrodynamic solution by TvNS method in two dimensions and compare these results with the solution from event-driven MD simulation in two dimensions.

## 5.2.1 TvNS solution in two dimensions

We start this section by the set of hydrodynamic equations in two dimensions,

$$\partial_t \rho + \partial_r(\rho v) + r^{-1} \rho v = 0, \quad (5.1)$$

$$\partial_t v + v \partial_r v + \rho^{-1} \partial_r p = 0, \quad (5.2)$$

$$\partial_t s + v \partial_r s = 0. \quad (5.3)$$

with the Rankine-hugoniot conditions given by Eq. (2.28).

Convert this set of non-linear coupled partial differential equations to ordinary differential equations by non-dimensionalizing the quantities as earlier,

$$\begin{aligned} p &= \frac{\rho_0 r^2}{t^2} P(\xi), \\ \rho &= \rho_0 R(\xi), \\ v &= \frac{r}{t} V(\xi), \\ \varepsilon &= \frac{k_B T}{m_0} = \frac{r^2}{t^2} E(\xi), \end{aligned} \quad (5.4)$$

where the dimensionless length is,

$$\xi = r \left( \frac{E_0 t^2}{\rho_0} \right)^{-1/4}. \quad (5.5)$$

The new set ordinary differential equations are,

$$\begin{aligned} \left( V - \frac{1}{2} \right) R \frac{dV}{d \ln \xi} + \frac{dP}{d \ln \xi} - RV + RV^2 + 2P &= 0, \\ \frac{dV}{d \ln \xi} + \left( V - \frac{1}{2} \right) \frac{d \ln R}{d \ln \xi} + 2V &= 0, \\ \frac{d}{d \ln \xi} \left( \ln \frac{P}{R^V} \right) - \frac{2(1-V)}{V-1/2} &= 0, \end{aligned} \quad (5.6)$$

with boundary conditions,

$$\begin{aligned} P(\xi_f) &= \frac{1}{2(\gamma + 1)}, \\ V(\xi_f) &= \frac{1}{\gamma + 1}, \\ R(\xi_f) &= \frac{\gamma + 1}{\gamma - 1}. \end{aligned} \tag{5.7}$$

The position of shock front is obtained from the expression for energy,

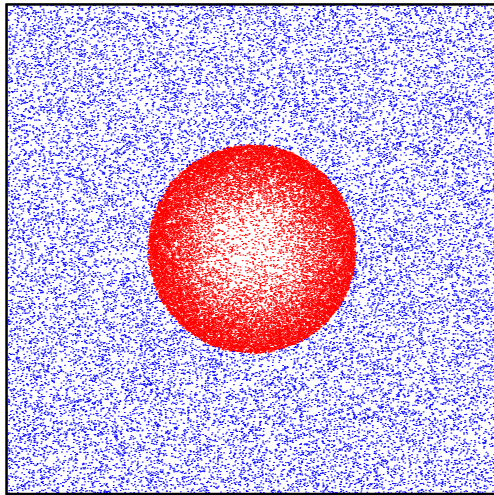
$$2\pi \int_0^{\xi_f} R(\xi) \left[ \frac{V^2(\xi)}{2} + \frac{P(\xi)}{(\gamma - 1)R(\xi)} \right] \xi^3 d\xi = 1. \tag{5.8}$$

For a monoatomic gas in two dimensions  $\gamma = 2$ , as  $\gamma = 1 + \frac{2}{f}$ , where  $f$  represents the degree of freedom which is 2 here. Eq. (5.8) gives the value of  $\xi_f = 1.298335$  for  $\gamma = 2$ .

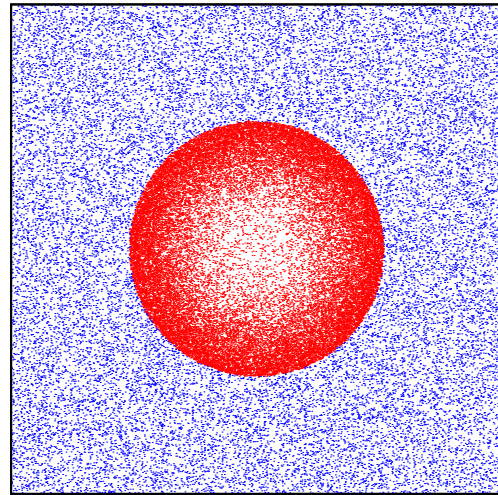
## 5.2.2 Comparison with event-driven simulations

In this section, we compare the predictions of the TvNS solution in two dimensions for density, velocity, pressure, and temperature profiles with results from large scale event-driven simulations [68] of a collection of elastic hard spheres in two dimensions. Consider a system of identical hard particles in two dimensions whose mass and diameter are set to one. Initially, all particles are at rest and uniformly distributed in space. The system is perturbed by an initial localized input of energy at the origin. We model an isotropic impulse by giving a speed  $v_0 = 1$  to 4 particles near the center along  $\pm x$ , and  $\pm y$  directions. The particles move ballistically until they undergo elastic momentum conserving collisions with other particles. The velocities of the particles undergoing collisions change according to the collision rule (See Eq. (4.1))

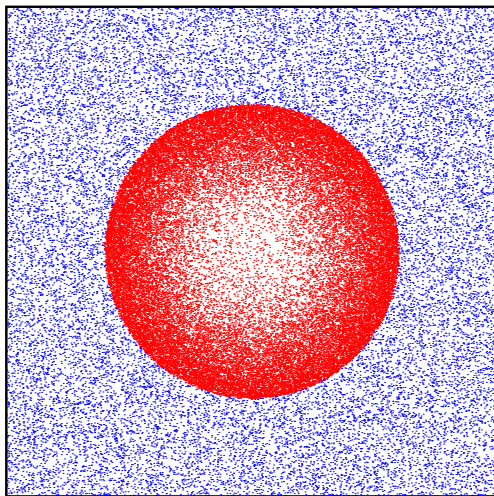
We simulate systems with number densities  $\rho_0 = 0.15$  and  $0.382$ . The system is large enough so that the moving particles do not reach the boundary up to the times we have simulated, so that the boundary effects can be avoided. The data are averaged over 150



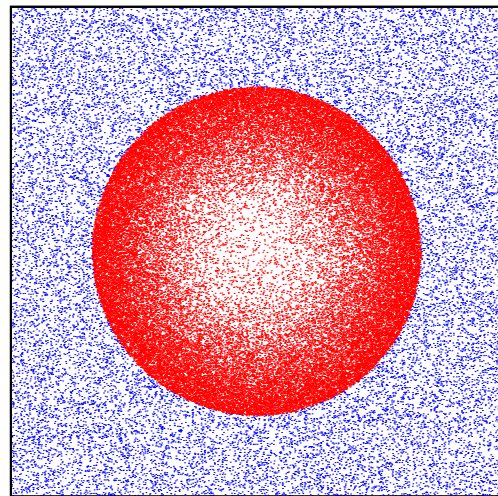
(a)



(b)



(c)



(d)

Figure 5.1: Moving (red) and stationary (blue) particles at times (a)  $t = 100000$ , (b)  $t = 150000$ , (c)  $t = 200000$  and (d)  $t = 250000$ . Energetic particles are injected at the center. All collisions are elastic with  $r = 1$ . The data are for the ambient density  $\rho_0 = 0.15$ .

different histories.

The initial perturbation creates a disturbance that propagates outward in a radially symmetric fashion with a well defined shock front, that separates the moving particles from the stationary ones as shown in Fig 5.1. The radius of this shock front has been earlier shown to increase as  $t^{1/2}$  in event-driven simulations [9, 10], consistent with the TvNS solution. Our aim is to numerically determine the scaling functions  $R(\xi)$ ,  $V(\xi)$ ,  $E(\xi)$ , and  $P(\xi)$ , corresponding to density, velocity, temperature, and pressure respectively.

The numerically obtained scaling functions  $R(\xi)$ ,  $V(\xi)$ ,  $E(\xi)$ , and  $P(\xi)$  are shown in Fig. 5.2 for initial number densities 0.1 and 0.4. For each of the densities, four different times are shown. In the figure, points represent the data obtained from simulation and the solid black line represents the TvNS solution. The data for the four different times collapse onto one curve when plotted against the dimensionless length  $\xi$ . Since the simulations correspond to a monoatomic gas, we set  $\gamma = 2$  in the TvNS solution.

The scaling function  $R(\xi)$  depends on the initial number density  $\rho_0$ , especially close to the shock front [see Fig 5.2(a)]. As  $\rho_0$  decreases, the discontinuity in density at the shock front increases. However, when compared with the entire range of  $\xi$ , the numerically obtained curves are very different from the TvNS solution.

The scaling function  $V$ , shown in Fig 5.2(b), increases linearly from zero, reaches a maximum and then decreases to its value at the shock front. The data for  $V$  from the simulations are again not consistent with the TvNS solution in which  $V$  is non-zero at  $\xi = 0$ , and then monotonically increases to its value at the shock front. Decreasing the ambient number density  $\rho_0$  shifts the numerical data further away from the TvNS solution for small  $\xi$ .

The scaling function  $E(\xi)$ , which measures the local velocity fluctuations, is shown in Fig 5.2(c). There is only a weak dependence on the number density  $\rho_0$ . Fig 5.2(d) shows that the pressure also does not depend on the ambient density.



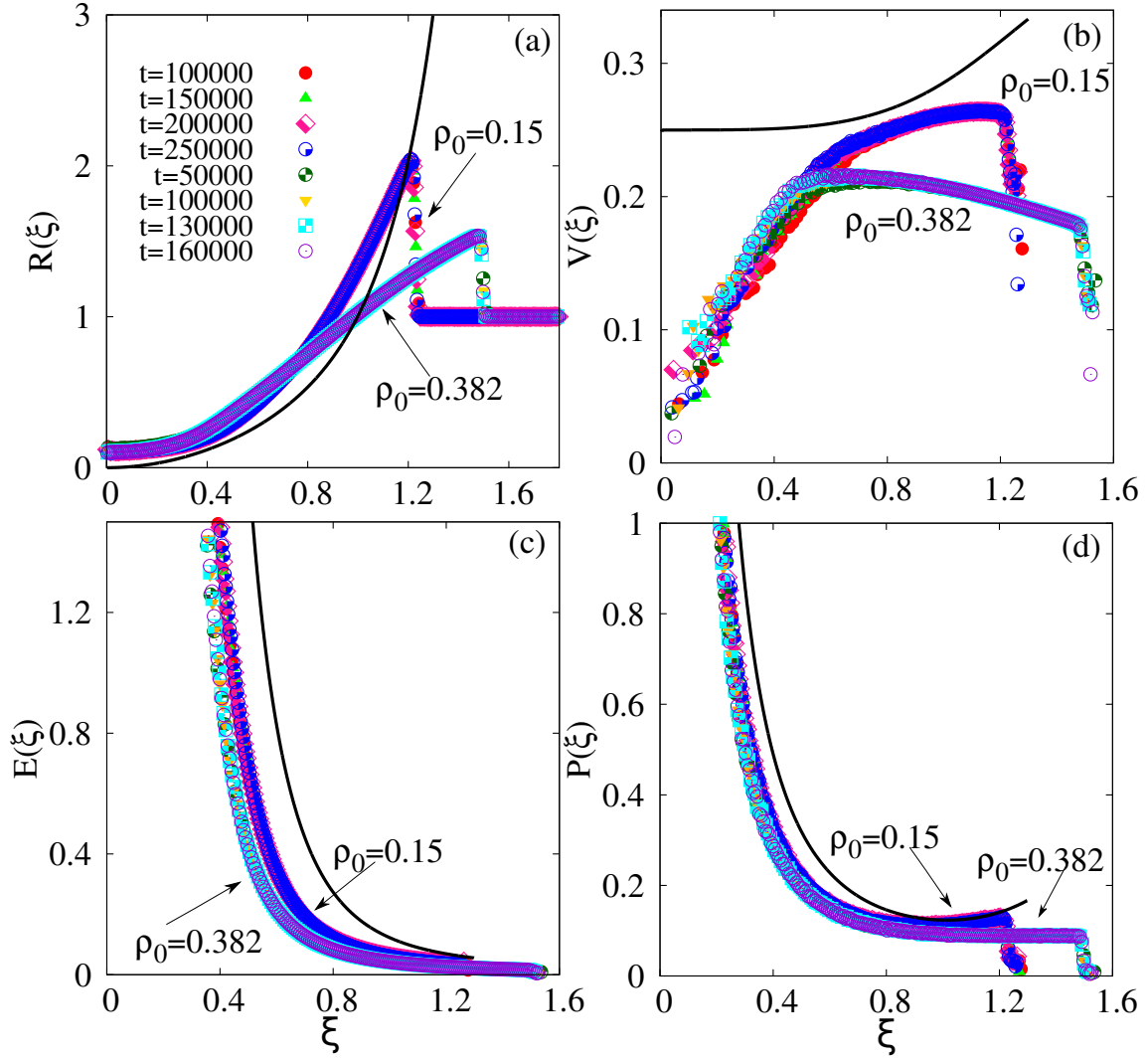


Figure 5.2: The variation of the scaling functions (a)  $R(\xi)$ , (b)  $V(\xi)$ , (c)  $E(\xi)$  and (d)  $P(\xi)$  corresponding to non-dimensionalized density, velocity, temperature and pressure [see Eq. (2.32)] with scaled distance  $\xi$ . The data are shown for 2 different initial densities  $\rho_0 = 0.15$  and  $0.382$ . For  $\rho_0 = 0.15$ , the different times are  $t = 100000, 150000, 200000, 250000$ , and for  $\rho = 0.382$ ,  $t = 50000, 100000, 130000, 160000$ , as indicated in (a). The black solid lines correspond to the TvNS solution [see Eqs. (2.36)-(2.38) and Eq. (4.4)]. The data for  $R, P$ , and  $E$  are also shown on a logarithmic scale in Fig. 5.3.

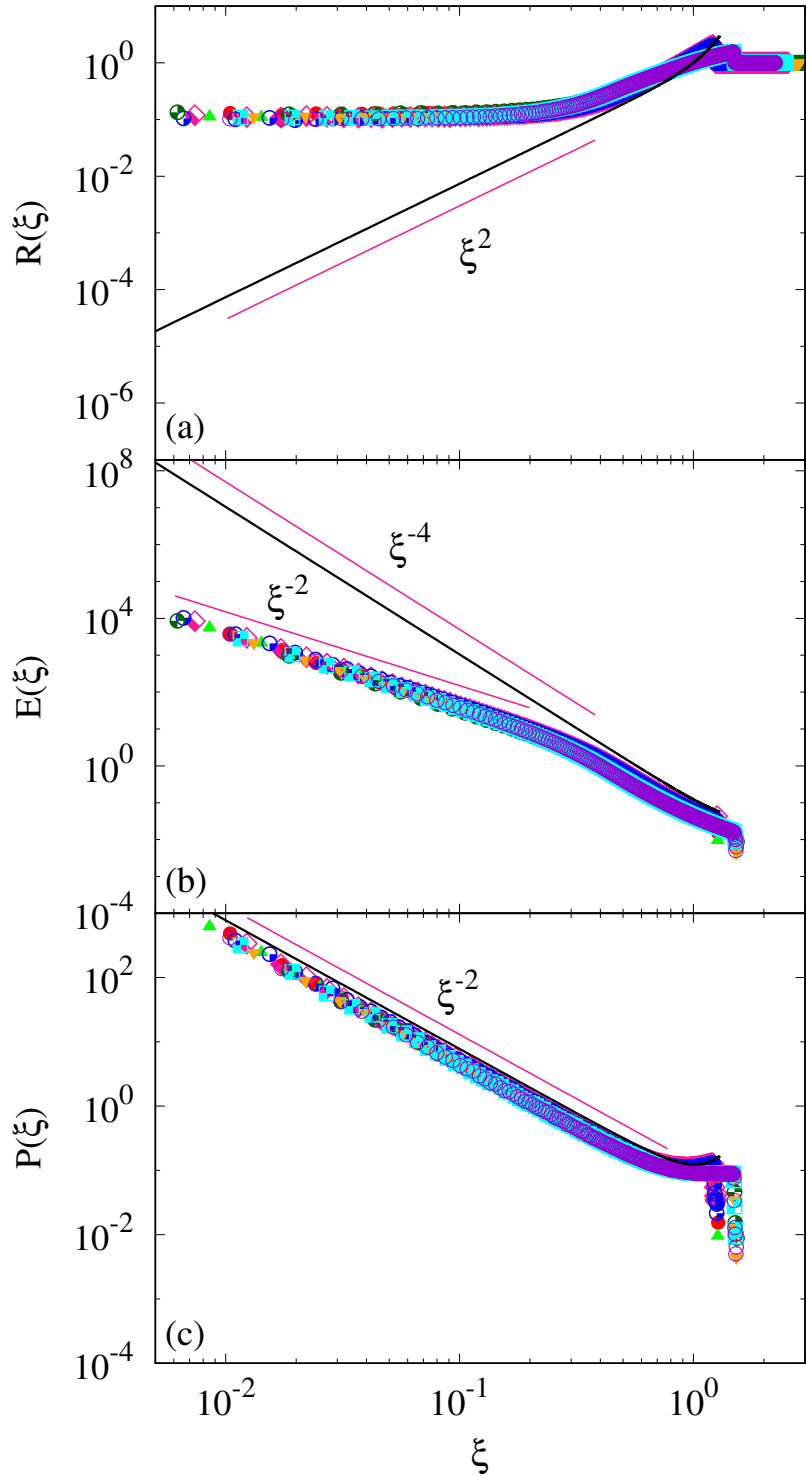


Figure 5.3: The data in Fig. 5.2(a), (c) and (d) are shown in logarithmic scale to emphasize the power-law divergence for small  $\xi$ . The three plots show the variation of the scaling functions (a)  $R(\xi)$ , (b)  $E(\xi)$  and (c)  $P(\xi)$  with scaled distance  $\xi$ . The data are for 2 different initial densities  $\rho_0 = 0.15$  and  $0.382$ . Each density has data for four different times and the symbols are same as described in Fig 5.2 (a). The black solid lines correspond to the TvNS solution.

The behavior of the scaling functions become more worse when they plotted in log-log plot as shown in Fig 5.3. Fig 5.3(a) shows that for small  $\xi$ , the TvNS scaling function increases as a power-law  $\xi^2$  [as in Eq. (2.41)], while the numerically obtained scaling function tends to a non-zero constant. From Fig 5.3(b), it can be seen that  $E$  diverges as a power-law as  $\xi \rightarrow 0$ , with an exponent that we numerically estimate to be close to  $-2$ . The TvNS solution predicts that  $E$  diverges with decreasing  $\xi$  as  $E \sim \xi^{-4}$  [see Eq. (2.42)]. Again, the data from simulations are quantitatively different from the TvNS solution. Unlike the other scaling functions, the data for pressure from simulations are much closer to the TvNS solution. In particular, both data diverge as  $\xi^{-2}$  for small  $\xi$  [see Fig 5.3(c)]. Also, as the number density  $\rho_0$  is decreased, the data tends towards the analytical solution.

In summary, the TvNS solution in two dimensions inadequate to describe the numerical data obtained from simulation in two dimensions. Also, the data from simulations show that the results depend on  $\rho_0$ . On the other hand the TvNS solution is independent of  $\rho_0$ . There could be multiple plausible reasons for the observed differences. One is that the simulations are performed for hard spheres, while the TvNS solution is for the ideal gas. In the hard sphere simulations, there is an upper bound for the local number density, while there is no such bound in the ideal gas. This particularly becomes significant near the shock front where the density becomes high irrespective of the initial density. Secondly, the medium through which shock is propagating is inherently a system out of equilibrium, and the assumption of local equilibrium in the TvNS solution may be incorrect.

Our results in two dimensions also are contradictory to the results obtained in Ref [17], where the numerical data was found to be in agreement with the TvNS solution. In Ref. [17], the equation of state was taken to be Henderson relation [73], while we have used the virial equation of state. To make sure that the discrepancy is not due to the choice of equation of state, we compare the virial equation of state, truncated at  $n = 10$ , with the Henderson relation, as shown in Fig 5.4. Clearly, the two equations of state match for all

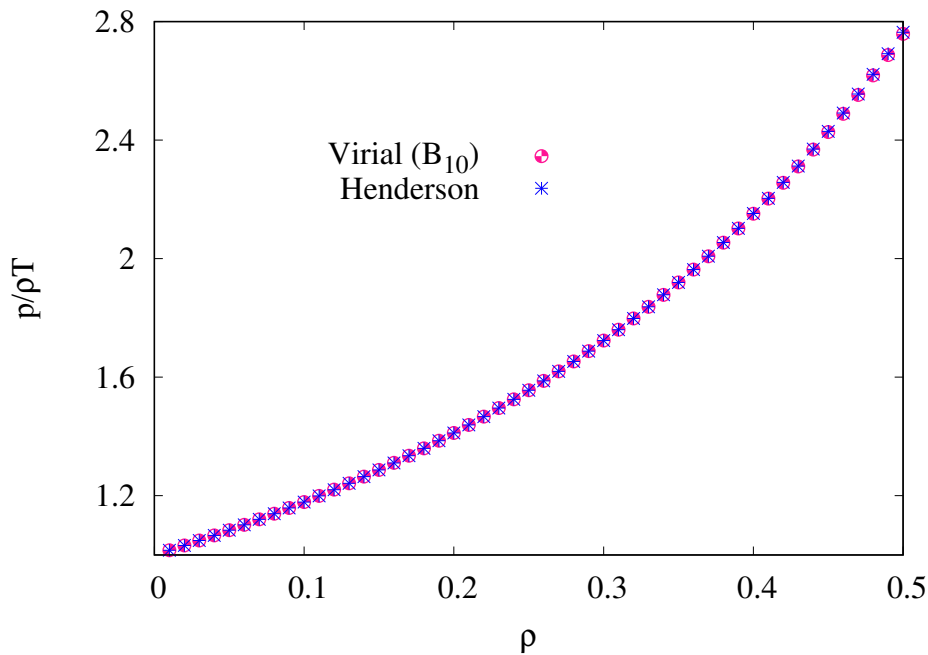


Figure 5.4: The virial equation of state truncated at  $n = 10$  and the Henderson relation are plotted. It is observed that both the curve match well.

the densities that we have considered.

In the following, we test the assumptions made in TvNS theory as we did in Chapter 4. First, we incorporate effects of explosion in the hard sphere model by replacing the equation of state of an ideal gas in the TvNS theory in two dimensions with a virial expansion for the hard sphere gas. Second, we test the assumption of local equilibrium.

### 5.3 Shock propagation in two dimensional elastic media

By considering the virial equation of state given in Eq. (4.6), the hydrodynamic equations of motion for the blast wave propagating through two dimensional media can be written

as,

$$\partial_t \rho + \partial_r(\rho v) + r^{-1} \rho v = 0, \quad (5.9)$$

$$\partial_t v + v \partial_r v + k_B T \left( 1 + \sum_{n=2}^{\infty} n B_n \rho^{n-1} \right) \partial_r \ln \rho + k_B T \left( 1 + \sum_{n=2}^{\infty} B_n \rho^{n-1} \right) \partial_r \ln T = 0, \quad (5.10)$$

$$(\partial_t + v \partial_r) \ln T - \left[ 1 + \sum_{n=2}^{\infty} B_n \rho^{n-1} \right] (\partial_t + v \partial_r) \ln \rho = 0. \quad (5.11)$$

Non-dimensionize the thermodynamic quantities using Eq. (5.4), the Eqs. (5.9)-(5.11) reduce to,

$$\begin{aligned} \left( V - \frac{1}{2} \right) \xi R \frac{dV}{d\xi} + \xi \frac{d}{d\xi} \left[ ER \left( 1 + \sum_{n=2}^{\infty} B_n \rho_0^{n-1} R^{n-1} \right) \right] - RV + RV^2 \\ + 2RE \left[ 1 + \sum_{n=2}^{\infty} B_n \rho_0^{n-1} R^{n-1} \right] = 0, \end{aligned} \quad (5.12)$$

$$\left( V - \frac{1}{2} \right) \xi \frac{dR}{d\xi} + \xi R \frac{dV}{d\xi} + 2RV = 0, \quad (5.13)$$

$$-\left( 1 + \sum_{n=2}^{\infty} B_n \rho_0^{n-1} R^{n-1} \right) \left( V - \frac{1}{2} \right) \frac{\xi}{R} \frac{dR}{d\xi} + \left( V - \frac{1}{2} \right) \frac{\xi}{E} \frac{dE}{d\xi} + 2(V - 1) = 0, \quad (5.14)$$

where the dimensionless length  $\xi$  is defined in Eq. (5.5). The Rankine-Hugoniot boundary conditions at the shock front  $\xi_f$  are,

$$\begin{aligned} \frac{1}{R(\xi_f)} \left[ 1 + \frac{2}{1 + \sum_{n=2}^{\infty} B_n \rho_0^{n-1} R(\xi_f)^{n-1}} \right] &= 1, \\ V(\xi_f) &= \frac{1}{R(\xi_f) [1 + \sum_{n=2}^{\infty} B_n \rho_0^{n-1} R(\xi_f)^{n-1}]}, \\ E(\xi_f) &= \frac{1}{2} V(\xi_f)^2. \end{aligned} \quad (5.15)$$

Eqs. (5.12)-(5.14) with the boundary conditions in Eqs. (5.15) may be solved numerically for a given  $\xi_f$ . The value of  $\xi_f$  is determined, as before, by the condition that total energy

$n$	$B_n$
2	$\frac{\pi}{2}$
3	$(\frac{4}{3} - \frac{\sqrt{3}}{\pi})B_2^2$
4	$[2 - \frac{9\sqrt{3}}{2\pi} + \frac{10}{\pi^2}]B_2^3$
5	$0.33355604B_2^4$
6	$0.1988425B_2^5$
7	$0.11486728B_2^6$
8	$0.0649930B_2^7$
9	$0.0362193B_2^8$
10	$0.0199537B_2^9$

Table 5.1: The values of the virial coefficients  $B_n$  for the hard sphere gas in two dimensions. The data are taken from Ref. [71].

is conserved, which in terms of the scaling functions is

$$2\pi \int_0^{\xi_f} R(\xi) \left[ \frac{V^2(\xi)}{2} + E(\xi) \right] \xi^3 d\xi = 1, \quad (5.16)$$

which is equivalent to Eq. (2.35) for  $d = 2$  with  $\gamma = 2$  and  $P = RE$ .

For the hard sphere gas in two dimensions, the virial coefficients  $B_n$  are known analytically for up to  $n = 4$  and through Monte Carlo simulations up to  $n = 10$  [71]. These are tabulated in Table 5.1.

The initial density  $\rho_0$  appears explicitly in the hydrodynamic equations as well as the boundary conditions and therefore it affects the results. The limit  $\rho_0 \rightarrow 0$  in these equations should reproduce the TvNS solution. We thus expect that there could be significant deviations for larger densities. We now compare the results for the solution for the hydrodynamic equation in two dimensions with virial EOS for hard sphere gas with that for the ideal gas as well as those obtained from simulations in two dimensions.

In Figs. 5.5 and 5.6, the TvNS solution with virial EOS is denoted by lines while the simulation data are shown by points for  $\rho_0 = 0.15$  and  $\rho_0 = 0.382$  respectively. We first focus on the effect of truncating the virial EOS by including only the first  $n$  virial terms.

We find that the scaling functions for density, velocity, temperature, and pressure for  $n = 6, 8, 10$  are indistinguishable from each other for both densities [see Figs. 5.5 and 5.6], showing that errors introduced by truncating the EOS at  $n = 10$  are negligible. Second, we observe that as  $n$  or  $\rho_0$  increases, the discontinuities at the shock front decreases, and the position of the shock front  $\xi_f$  increases. Third, and more importantly, the inclusion of virial EOS does not alter the exponents of the power-law divergence of the scaling functions at small  $\xi$ . Also, the exponents are independent of  $\rho_0$ .

Near the shock front, in comparison to the ideal gas EOS, we find that the virial EOS does a better job of describing the scaling functions obtained from simulations. For the density scaling function, the discontinuity at the shock front is better captured by the virial EOS for both densities [see Figs. 5.5(a) and 5.6(a)]. For the scaled velocity, the virial EOS matches well with the simulation data away from the shock center for  $\rho_0 = 0.15$  [see Fig. 5.5(b)], and captures the correct trend for  $\rho_0 = 0.382$  [see Fig. 5.6(b)]. For both temperature [see Figs. 5.5(c) and 5.6(c)] and pressure [see Figs. 5.5(d) and 5.6(d)], the scaling functions obtained from virial EOS are closer to the simulation data than the ideal gas EOS.

Away from the shock front, the power-law behavior of the scaling function remain unchanged with the inclusion of the virial EOS. This is because near the shock center, the gas is dilute, and the virial EOS tends towards the ideal gas law. Thus, as for the TvNS theory discussed in Sec. 5.2, the modified theory is insufficient to describe the simulation data [see insets of Figs. 5.5 and 5.6].

Thus, we conclude that while replacing the ideal gas assumption in the TvNS solution with the virial EOS for the hard sphere gas introduces some dependence on the initial density  $\rho_0$ , it fails to capture the strong deviations from the TvNS solution, especially near the shock center, that is observed in the event-driven simulations.

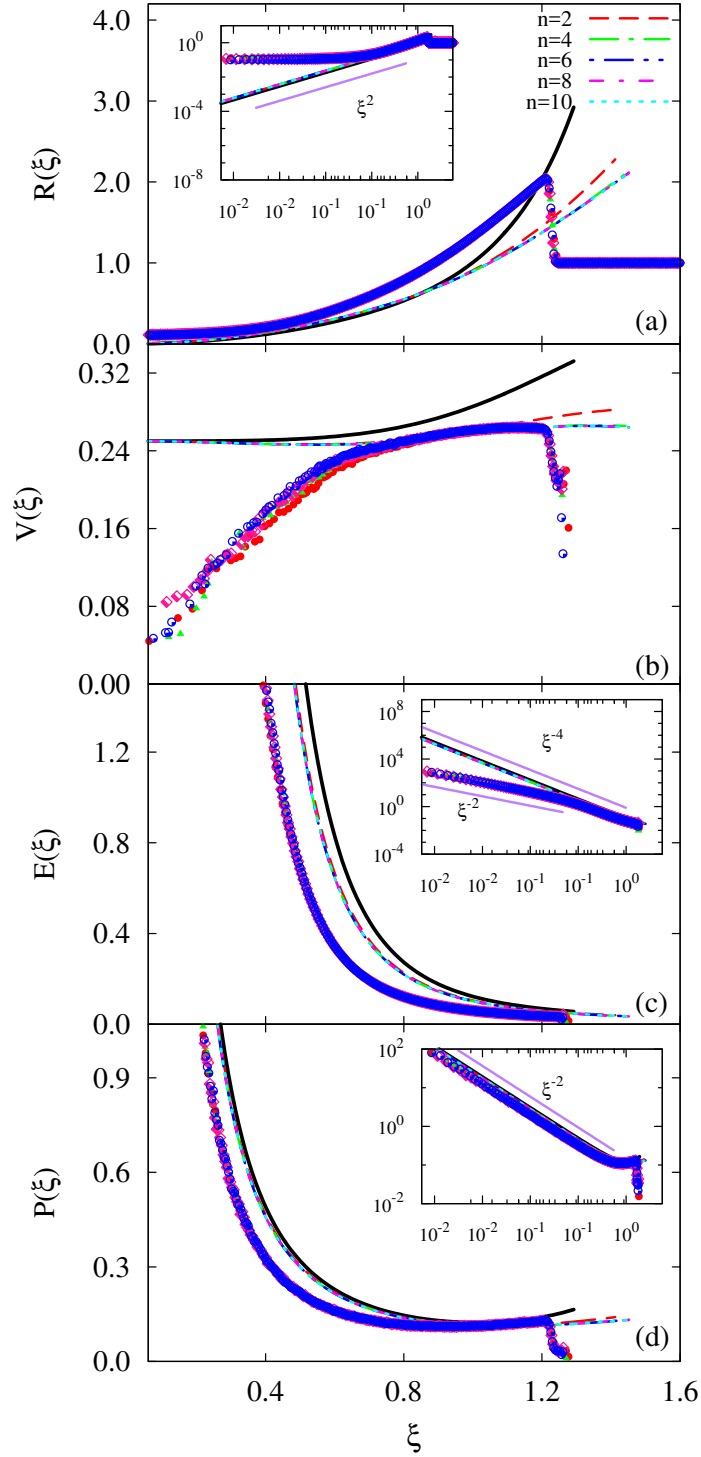


Figure 5.5: The scaling functions (a)  $R(\xi)$ , (b)  $V(\xi)$ , (c)  $E(\xi)$ , and (d)  $P(\xi)$  corresponding to density, velocity, temperature and pressure respectively versus  $\xi$  for ambient density  $\rho_0 = 0.15$  is compared with the theoretical solution for the hydrodynamic equations with virial EOS for the hard sphere gas. The simulation data (represented by points) correspond to four different times with keys as shown in Fig 5.2(a). The lines represent the virial EOS solution with the virial expansion truncated at  $n = 2, 4, 6, 8, 10$ . Black solid curve represents the case of ideal gas. The inset shows the plots on a log-log scale, accentuating the small  $\xi$  behavior.



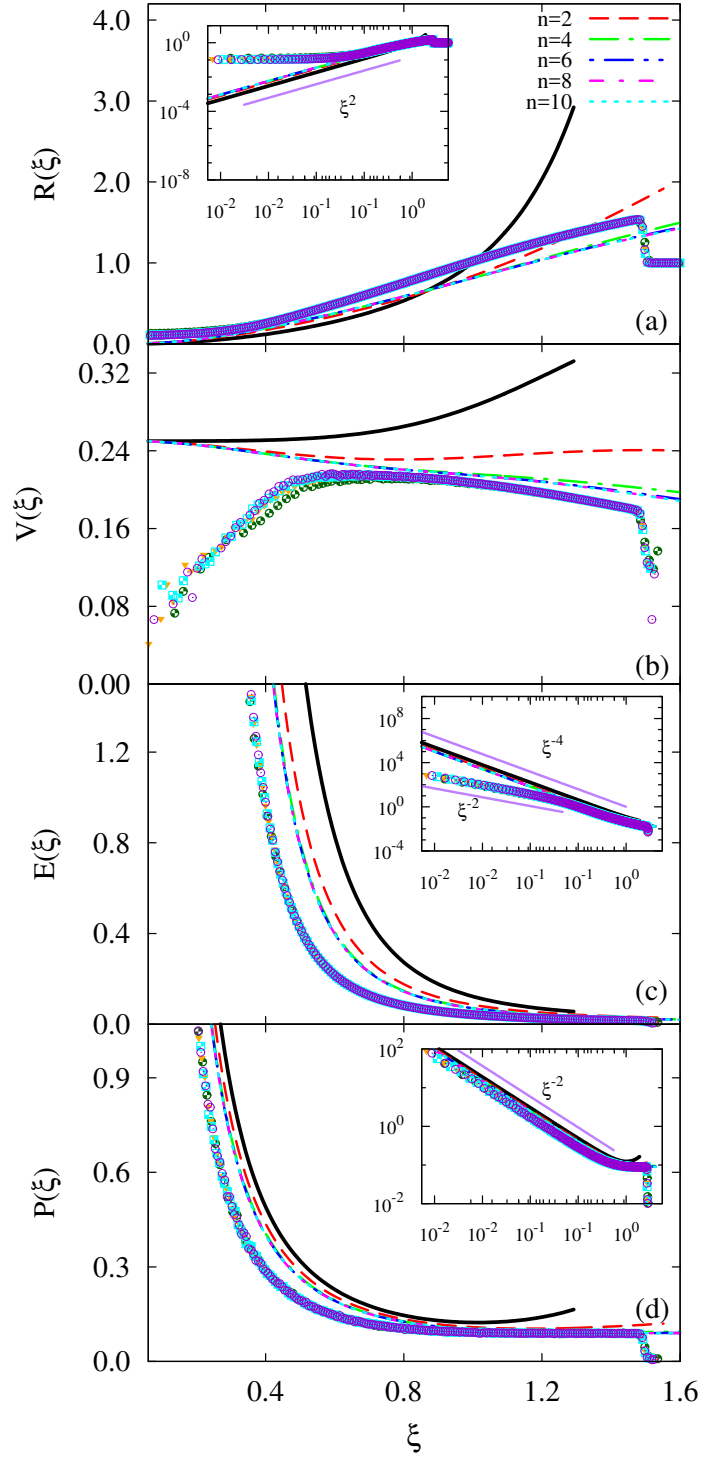


Figure 5.6: The scaling functions (a)  $R(\xi)$ , (b)  $V(\xi)$ , (c)  $E(\xi)$ , and (d)  $P(\xi)$  corresponding to density, velocity, temperature and pressure respectively versus  $\xi$  for ambient density  $\rho_0 = 0.382$  is compared with the theoretical solution for the hydrodynamic equations with virial EOS for the hard sphere gas. The simulation data (represented by points) correspond to four different times with keys as shown in Fig 5.2(a). The lines represent the virial EOS solution with the virial expansion truncated at  $n = 2, 4, 6, 8, 10$ . Black solid curve represents the case of ideal gas. The inset shows the plots on a log-log scale, accentuating the small  $\xi$  behavior.

## 5.4 Local Equilibrium

As we have done in chapter 4, here also we numerically check the assumption of local equilibrium in the TvNS solution. First, we check whether the EOS of a hard sphere gas is obeyed. Second, we check whether the thermal energy is locally equipartitioned equally in the two directions. Finally, we calculate the skewness and kurtosis of the distribution of velocity fluctuations to check the deviation from a gaussian.

### 5.4.1 Equation of state

To check the central assumption of TvNS theorem of the existence of an EOS, we measure the local thermodynamic quantities independently and check whether they obey the hard sphere virial EOS. In order to do that we measure the ratio as we did in Sec. 4.4.1 of chapter 4. We write the equation here for convenience,

$$\chi(n) = \frac{P(\xi)}{E(\xi)R(\xi) \left[ 1 + \sum_{k=2}^n B_k \rho_0^{k-1} R(\xi)^{k-1} \right]}, \quad (5.17)$$

where  $n$  is the number of terms retained in the virial expansion [ $n = 1$  corresponds to ideal gas]. For large  $n$ , if  $\chi \approx 1$ , then we conclude that the virial EOS is obeyed, and the assumption of EOS is justified.

The dependence of  $\chi(n)$  on  $\xi$  for  $n = 2, 4, 6, 8, 10$  is shown in Fig. 5.7 for two different times. While for small  $n$ , there is deviation from one near the shock front, quite remarkably, as  $n$  increases,  $\chi(n)$  fluctuates about 1 for all  $\xi$ . This clearly shows that the assumption of an EOS is quite justified.

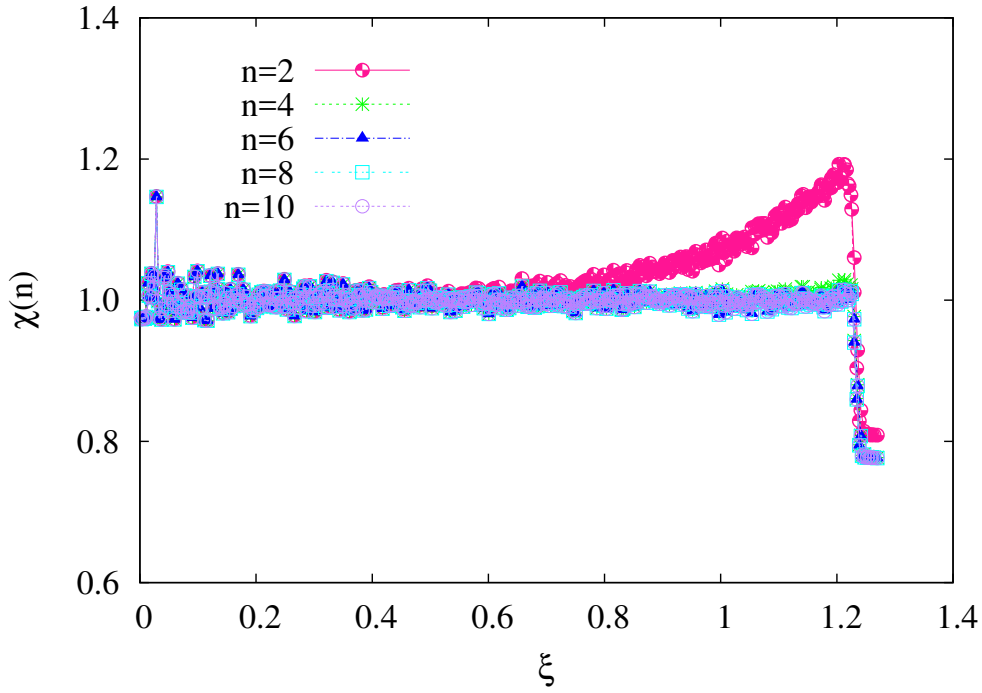


Figure 5.7: The variation of  $\chi(n)$  [see Eq. (5.17)] with  $\xi$  for  $n = 2, 4, 6, 8, 10$ . The data are for times 150000 and 250000 and for ambient number density  $\rho_0 = 0.15$ . For large  $n$ ,  $\chi(n)$  fluctuates about 1.

## 5.4.2 Equipartition

We check whether the thermal energy is equipartitioned equally in the twodirections by measuring the ratio

$$\zeta = \frac{\langle \delta v_r^2 \rangle}{\langle \delta v_\perp^2 \rangle}, \quad (5.18)$$

where  $\delta v_r$  and  $\delta v_\perp$  are the velocity fluctuations in the radial and transverse directions respectively. If the thermal energy is equipartitioned, then  $\zeta = 1$ . Fig. 5.8 shows the variation of  $\zeta$  with  $\xi$  for different times. The data for different times collapse on to a single curve. Away from the shock front,  $\zeta \approx 1$  showing equipartition. However, near the shock front,  $\zeta > 1$ , corresponding to excess thermal energy in the radial direction.

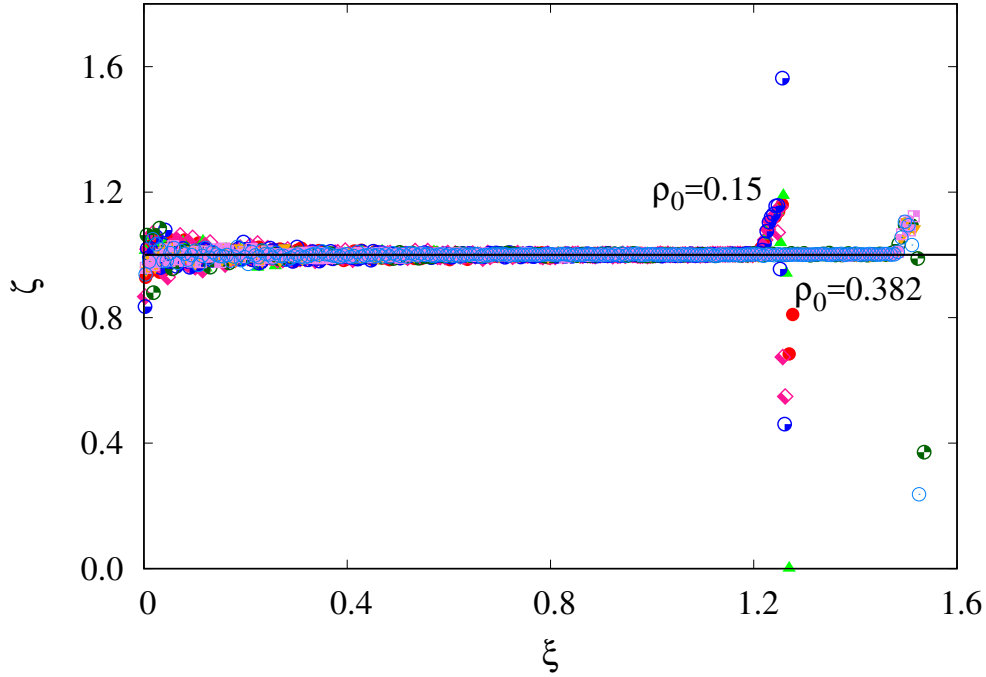


Figure 5.8: The variation of  $\zeta$ , the ratio of energies in the radial and transverse directions [see Eq. (5.18)] with the scaled distance  $\xi$ . The data is for four different times with keys as in Fig 5.2(a), for two ambient densities  $\rho_0 = 0.15$  and  $0.382$ . Away from the shock front,  $\zeta \approx 1$ .

### 5.4.3 Skewness and Kurtosis

To quantify the deviation from gaussianity, we measure the kurtosis  $\kappa$ , and skewness  $S$  of the probability distribution for the velocity fluctuations. The kurtosis and skewness are defined as,

$$\kappa = \frac{\langle \delta v^4 \rangle}{\langle \delta v^2 \rangle^2}, \quad (5.19)$$

$$S = \frac{\langle \delta v_r^3 \rangle}{\langle \delta v_r^2 \rangle^{3/2}}. \quad (5.20)$$

For a gaussian distribution, the kurtosis is 3, and skewness is zero. Deviation from these values show the non-gaussian behavior. The radial and transverse components of kurtosis are denoted by  $\kappa_r$  and  $\kappa_\perp$  respectively and the variation of these quantities with  $\xi$  is shown in Fig 5.9 (a) and (b) respectively. While the data for different times collapse onto one curve,  $\kappa_r$  shows deviation from 3 near the shock center, showing a lack of local equilibrium

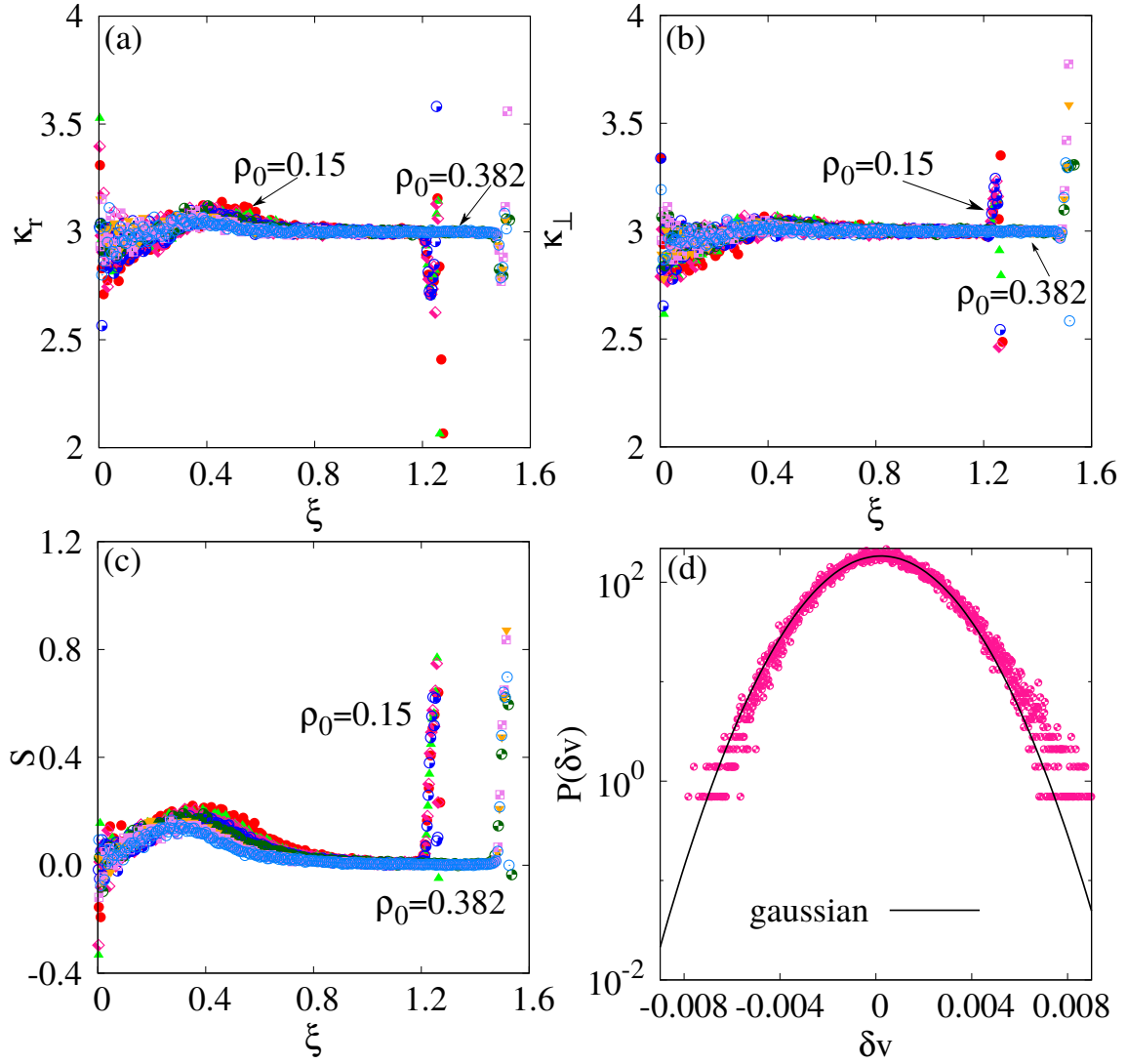


Figure 5.9: The variation with scaled distance  $\xi$  of (a) the kurtosis  $\kappa_r$  for the radial velocity fluctuations. (b) the kurtosis  $\kappa_\perp$  for the velocity fluctuations in the  $\theta$  direction and (c) skewness  $S$  for the radial velocity fluctuations. The data are for  $\rho_0 = 0.15$  and  $\rho_0 = 0.382$  and for four different times with keys as in Fig 5.2(a). (d) The distribution of the radial velocity fluctuations  $P(\delta v)$  measured at  $r = 462.5$ ,  $t = 250000$  and  $\rho_0 = 0.15$ , corresponding to  $\xi = 0.41$ . The black solid curve represents the gaussian distribution fitted to the data near zero.

near the shock center, but  $\kappa_{\perp}$  shows the value of 3 for almost all  $\xi$ . Skewness  $S$  also provides a strong evidence for deviation from gaussianity near the shock center and a lack of local equilibrium, but Fig 5.9 (c) shows the existence of local thermal equilibrium away from the shock center. From the variation of  $S$  with  $\xi$ , as shown in Fig. 5.9 (c), it is clear that it is positive for the values of  $\xi$  near to shock center. Thus, the distribution is clearly asymmetric.

The skewness of the distribution may be directly seen by examining the full probability distribution  $P(\delta v_r, r, t)$  for the fluctuations in the radial velocity. The distribution for a fixed time  $t$  and fixed radial distance  $r$ , corresponding to  $\xi = 0.58$  is shown in Fig 5.9(d). This corresponds to a region away from the shock front where the skewness in Fig. 5.9(c) is non-zero. It can be seen from the figure that the distribution deviates from the gaussian distribution and is skewed towards the larger positive fluctuations.

## 5.5 Conclusion and discussion

To summarize this chapter, we compared the TvNS solution for the radial distribution of pressure, temperature, density, and flow velocity fields with results from large scale event-driven molecular dynamics simulations of hard spheres in two dimensions. We find that the TvNS solution is inadequate to describe the numerical data well. In particular, the power-law behavior away from the shock front for temperature and density have different exponents in the theory and simulations. Our findings are conflicting with the results obtained in a recent study of two dimensions [17], which showed that the TvNS results match well with the solutions from simulations almost all regions of  $\xi$ , with a slight discrepancy near the shock center.

We modified TvNS theory in two dimensions by using a virial equation of state for the hard sphere gas instead of the ideal gas constitutive relation. We restricted our analysis to the known ten virial coefficients. While inclusion of the more realistic virial equation

of state modifies the theoretical predictions, especially near the shock front, it does not modify the exponents, and thus fails to describe the simulation data. Also, it is noted that the numerical data for the radial distribution of flow velocity for the density  $\rho_0 = 0.15$  matches with the modified theoretical data in a range of region away from the shock center.

We also checked the different assumptions of the TvNS theory. We find that the assumption of the existence of a local equation of state is borne out in our simulations. Though the numerics and theory do not agree for the scaling functions, the local pressure, temperature and density satisfy the virial equation of state for the hard sphere gas very well, except for a small deviation near the shock front [see Fig. 5.7]. On the other hand, the radial velocity fluctuations are not gaussian, and is skewed towards positive fluctuations near the shock center. This shows that local equilibrium is not attained near the shock center.





# Chapter 6

## Shock propagation in locally driven granular systems

### 6.1 Introduction

In chapters 4 and 5, we compared the results of the explosion problem in the hydrodynamic limit with the results from simulations of microscopic models in three and two dimensions respectively. The explosion problem is a typical example of the response of a dilute elastic gas at rest to an external perturbation that is applied as an instantaneous impulse. Crater formation and shock propagation in dilute inelastic gases are examples for the response of granular systems to a localized perturbation. The externally applied perturbation often results in a disturbance that grows in time as a power-law and the power-law exponents may be obtained by simple tractable models of suitably excited spherical particles where energy dissipation is only through inelastic collisions [10, 64]. Here, we discuss a model in which the systems, both elastic and inelastic, are perturbed by a continuous energy injection to a localized region. This scenario has been set in recent experiments with Hele-Shaw cell, an arrangement of two circular glass plates separated by very small distance with a hole at the center on the top plate through which the ma-

terial is injected to perturb the system of granular materials. Few examples include the pattern formation during air injection in a system of polydisperse spherical glass beads in a radial Hele-cell [22], pattern formation of various shapes due to the displacement of one granular material by another [23], a system of spherical glass beads in a Hele-Shaw cell is driven by the pressurised nitrogen gas resulting in fingering pattern [21], pattern formation in a dry dense granular medium of sand when it is invaded by aqueous glycerin solution [24], emergence of random pattern during the fluid injection in a system of polydisperse glass beads [65].

In this chapter we study a simple model of hard spheres at rest that is driven at the origin by a continuous injection of particles from outside. From a combination of event-driven simulations and scaling arguments, we determine the exponents governing the growth of the disturbance. The results are compared with the data from two experiments [21, 22] and excellent agreement is obtained.

The remainder of the chapter is organized as follows. In Sec. 6.2 we define the model precisely and give details of the event-driven simulations that we performed. The exponents characterizing the growth of the different physical quantities in the problem are determined using scaling arguments in Sec. 6.3. The assumptions and predictions of the scaling argument are tested using large scale simulations in Sec. 6.4 for both the elastic and the inelastic system. In Sec. 6.5 we show that the results in this study are able to explain data from two experiments on driven granular systems. Section 6.6 contains a brief summary and a discussion of results. The content of this chapter is published in Ref. [74].

## 6.2 Model

Consider a  $d$ -dimensional system of hard spheres whose mass and diameter are set to one. The particles move ballistically until they undergo momentum-conserving binary collisions with other particles. If  $\vec{u}_1$  and  $\vec{u}_2$  are the velocities of two particles 1 and 2

before collision, then the velocities after collision,  $\vec{v}_1$  and  $\vec{v}_2$ , are given by

$$\vec{v}_1 = \vec{u}_1 - \frac{1+r}{2}[\hat{n} \cdot (\vec{u}_1 - \vec{u}_2)]\hat{n}, \quad (6.1)$$

$$\vec{v}_2 = \vec{u}_2 - \frac{1+r}{2}[\hat{n} \cdot (\vec{u}_2 - \vec{u}_1)]\hat{n}, \quad (6.2)$$

where  $r$  is the coefficient of restitution and  $\hat{n}$  is the unit vector along the line joining the centers of particles 1 and 2. In a collision, the tangential component of the relative velocity remains unchanged as there is no force acting along this direction, while the magnitude of the longitudinal component is reduced by a factor  $r$ . The collisions are elastic when  $r = 1$ , and inelastic and dissipative otherwise.

Initially, all particles are at rest and uniformly distributed in space. The system is driven locally by a continuous input of energy restricted to a small region by injecting particles at a constant rate  $J$  at the origin. The injected particles have a speed  $v_0$  in a randomly chosen direction until they undergo their first collision, after which the injected particles are removed from the system. Driving in this manner injects energy into the system, but conserves the total number of particles. We will refer to this model as the conserved model.

We also consider a non-conserved model. This model is identical to the conserved model described above, but the injected particles stay in the system, thereby increasing the total number of particles at a constant rate  $J$ . While the conserved model is applicable to two-dimensional granular systems driven by a gas (where the gas may escape in the third dimension), the non-conserved model is applicable to two-dimensional granular systems driven by granular material. We will show in Sec. 6.3 that the scaling laws at large times are identical for both models. We will therefore present numerical results only for the conserved model.

We simulate systems with number density 0.25 (packing fraction 0.196) in two dimensions and 0.40 (packing fraction 0.209) in three dimensions, using event-driven molecular

dynamics [68]. These number densities are much smaller than the random close-packed density. The total number of particles is  $8 \times 10^6$  and is large enough such that the disturbance induced by the injection of particles does not reach the boundary up to the simulation times considered in this model. We set  $v_0 = 1$ , the rate of injection of particles  $J$  is set to 1, and the injected particles have the same mass and diameter as the other particles in the system. In the simulations, the collisions are inelastic with constant restitution coefficient  $r$  when the relative velocities of the particles are greater than a cut off velocity  $\delta$  and considered to be elastic otherwise. This procedure prevents the occurrence of the inelastic collapse of infinite collisions within a finite time, which is a hindrance in simulations, and is also in accordance with the fact that the coefficient of restitution tends to 1 with decreasing relative velocity between the colliding particle [75]. The value of  $\delta$  is  $10^{-4}$ , unless specified otherwise. The results are independent of  $\delta$ .

The numerical results in this chapter are shown only for the conserved model and are typically averaged over 48 different realizations of the initial particle configurations. All lengths are measured in units of the particle diameter and time in units of initial mean collision time  $t_0 = v_0^{-1} n^{-1/d}$ , where  $n$  is the number density.

### 6.3 Scaling Argument

In order to develop scaling arguments to describe the propagation of energy, it is important to first visualize how the inelastic system evolves in comparison to the elastic system. When the energetic particles are injected from the center, in both cases particles get disturbed up to a distance and the zone of disturbance propagates radially outward. Figures 6.1 and 6.2 show the time evolution of the elastic and inelastic systems with  $r = 1$  and  $r = 0.1$ , respectively, in two dimensions for the conserved model. In the elastic system, the circular region of moving particles (marked in red) has nonzero density everywhere. In contrast, in the case of the inelastic system, particles cluster together and form a dense

band adjacent to the front of the disturbance, forming a vacant region around the center. This circular band moves outward with time and grows by absorbing more particles. We observe the same features in the simulations of the nonconserved model.

We look for scaling solutions, similar to that found for the problem with a single impact in Ref. [10]. Let  $R_t$  be the typical radius of the disturbance at time  $t$ . We assume that it is the only relevant length scale in the problem. We assume a power-law growth for the radius of disturbance,  $R_t \sim t^\alpha$ . The typical velocity  $v_t$  is then given by,  $v_t \sim dR/dt \sim t^{\alpha-1}$ . The total number of moving particles that have undergone collisions  $N_t$  is given by the volume swept out by the disturbance in the conserved model, and the sum of the volume swept out by the disturbance and the injected particles for the nonconserved model. The volume swept out by the disturbance scales as  $R_t^d \sim t^{\alpha d}$ , where  $d$  is the spatial dimension, while the number of injected particles scales as  $Jt$ . Therefore, in the limit of large time,  $N_t \sim R_t^d \sim t^{\alpha d}$  for the conserved model and  $N_t \sim R_t^d \sim t^{\max[\alpha d, t]}$  for the nonconserved model. We discuss the two models separately.

### 6.3.1 Conserved model

The energy of the system scales as

$$E_t \sim N_t v_t^2 \sim t^{\alpha(d+2)-2}. \quad (6.3)$$

The exponent  $\alpha$  may be determined for the elastic and inelastic cases using different conservation laws. For the elastic system, energy is not dissipated during collisions. However, due to the constant driving, the total energy must increase linearly with time, i.e.,  $E_t \sim t$ . Comparing it with the scaling behavior of energy  $E_t \sim t^{\alpha(d+2)-2}$ , we conclude

$$\alpha = \frac{3}{d+2}, \quad r = 1. \quad (6.4)$$

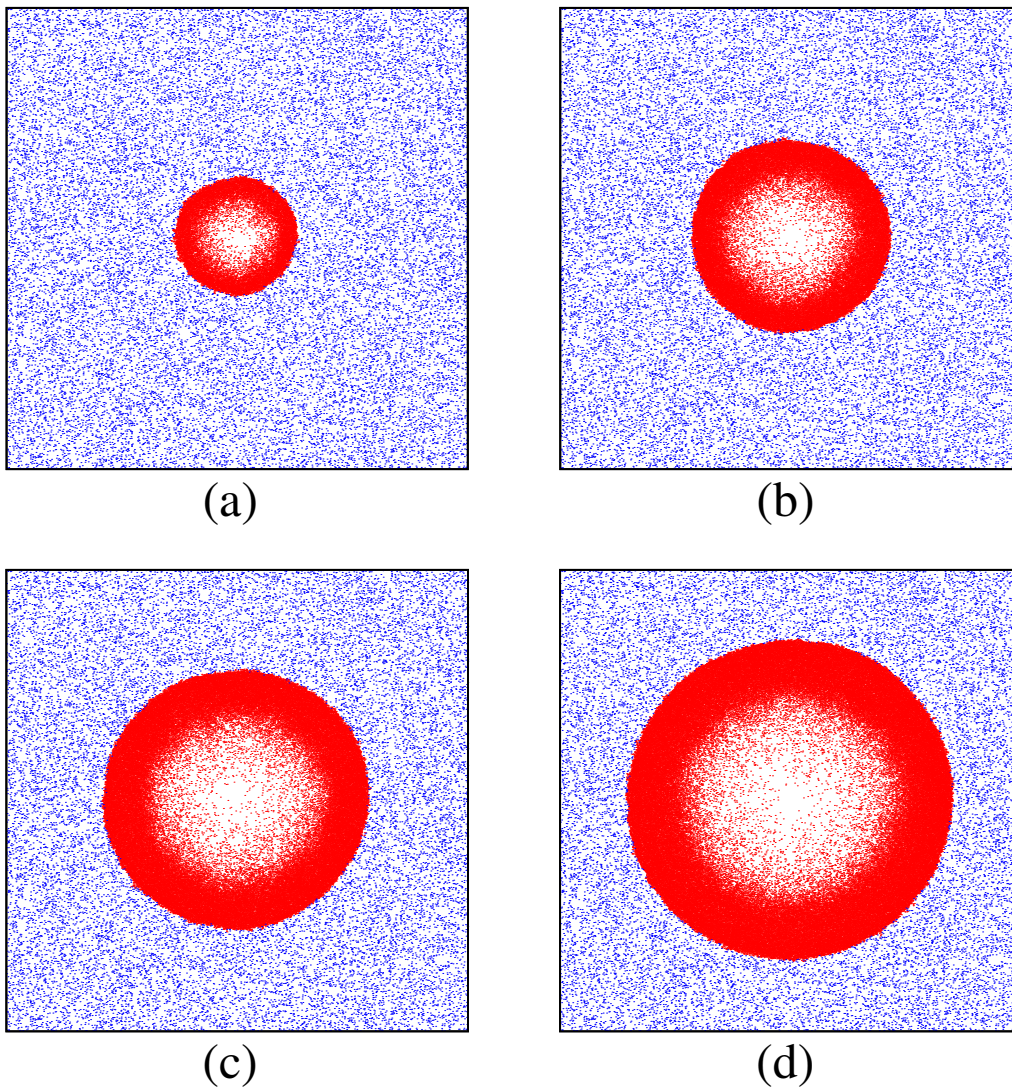


Figure 6.1: Moving (red) and stationary (blue) particles at times (a)  $t = 500$ , (b)  $t = 1000$ , (c)  $t = 1500$  and (d)  $t = 2000$ . Energetic particles are injected at the center. All collisions are elastic with  $r = 1$ . The data are for the conserved model.

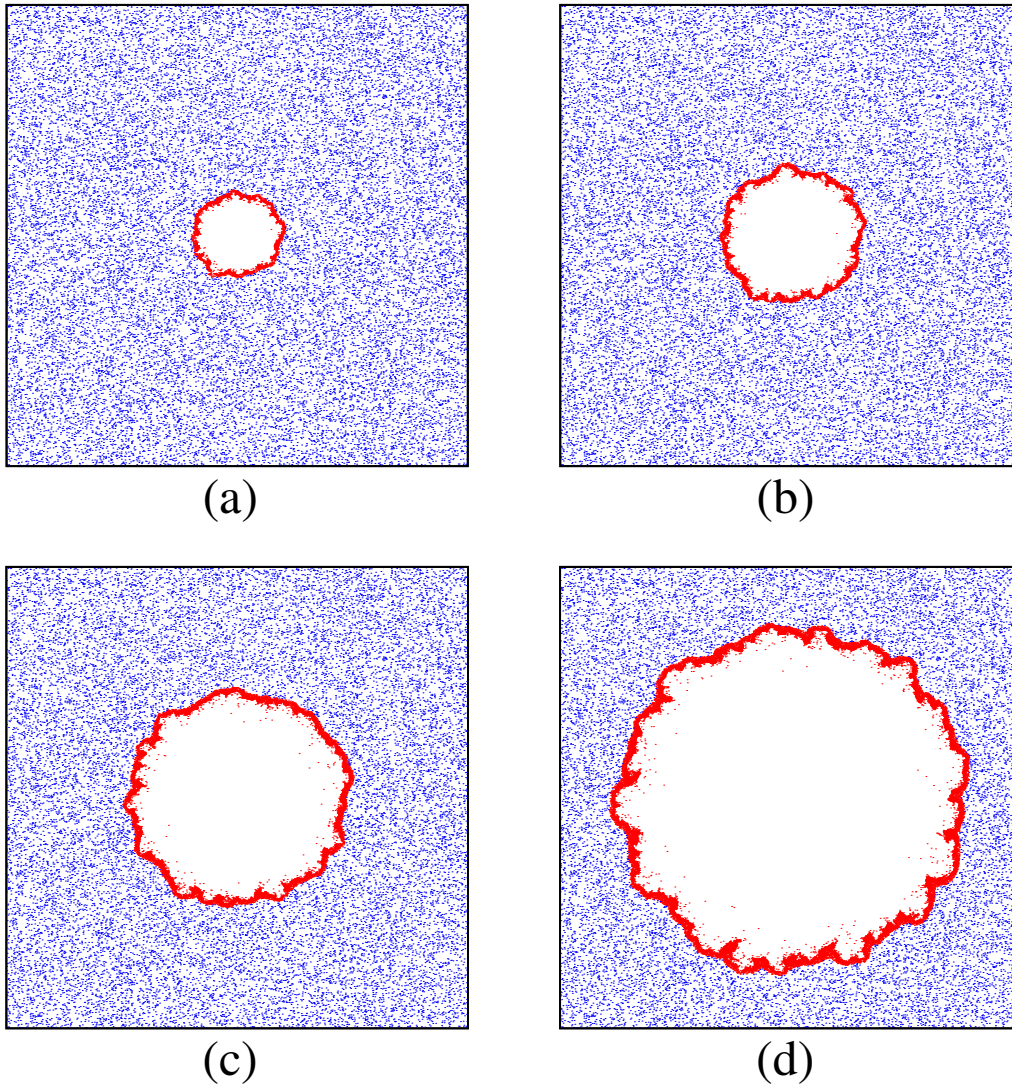


Figure 6.2: Moving (red) and stationary (blue) particles at times (a)  $t = 1000$ , (b)  $t = 2000$ , (c)  $t = 4000$  and (d)  $t = 8000$ . Energetic particles are injected at the center. All collisions are inelastic with  $r = 0.1$ . The data are for the conserved model.

This result coincides with the power-law scaling exponent obtained in the case of astrophysical blast waves [28].

For the inelastic system, the total energy is no longer conserved. However, the formation of the bands, as can be seen in Fig. 6.2, implies that there is no transfer of momentum from a point in the band to a point diametrically opposite to it by particles streaming across. Thus, once the bands form, radial momentum is conserved during collisions and flows radially outward [10, 64]. Due to the continuous driving, the radial momentum must increase linearly with time  $t$ . We confirm this in simulations by measuring radial momentum as the sum of the radial velocities of all the moving particles. As shown in Fig. 6.3, radial momentum increases linearly with time, at large times, in both two and three dimensions. There is an initial transient period (see the inset of Fig. 6.3), where the initial growth is not linear, reflecting the time taken to form stable dense bands. The radial momentum, in terms of the exponent  $\alpha$ , scales as  $N_t v_t \sim t^{\alpha(d+1)-1}$ . Comparing it with the linear increase in  $t$ , we obtain

$$\alpha = \frac{2}{d+1}, \quad r < 1. \quad (6.5)$$

### 6.3.2 Non-conserved model

We show that the non-conserved model has the same scaling laws as described in Eqs. (6.4) and (6.5). The energy of the system scales as

$$E_t \sim N_t v_t^2 \sim t^{\max[\alpha d, 1] + 2\alpha - 2}. \quad (6.6)$$

In the elastic case, energy is conserved and  $E_t \sim t$ . Comparing with Eq. (6.6), we obtain  $\alpha = 3/(d+2)$  if  $\alpha d \geq 1$  and  $\alpha = 1$  if  $\alpha d < 1$ . For  $d \geq 1$ , the only solution is  $\alpha = 3/(d+2)$ ,



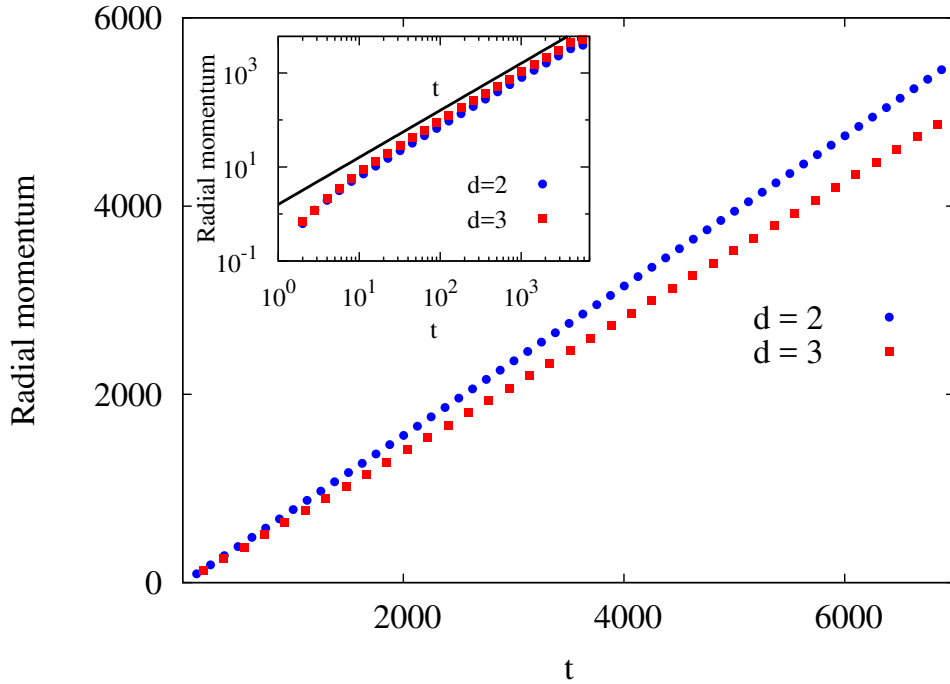


Figure 6.3: Radial momentum as a function of time  $t$  for two and three-dimensional inelastic systems, showing a linear increase. The inset shows the data on a log-log scale, which show an initial transient regime before the linear growth is attained. The data are for the conserved model.

as obtained for the conserved model [see Eq. (6.4)].

For the inelastic case, the radial momentum increases linearly with time (see Sec. 6.3.1). The radial momentum scales as  $N_t v_t \sim t^{\max[\alpha d, 1] + \alpha - 1}$ . Comparing it with the linear increase in  $t$ , we obtain  $\alpha = 2/(d + 1)$  if  $\alpha d \geq 1$  and  $\alpha = 1$  if  $\alpha d < 1$ . For  $d \geq 1$ , the only solution is  $\alpha = 2/(d + 1)$ , as obtained for the conserved model [see Eq. (6.5)].

We conclude that the scaling laws are identical for both the conserved and non-conserved models. In the remaining part of the chapter, we discuss only the conserved model.

## 6.4 Numerical Results

All the numerical results presented in this section are for the conserved model. The results for the non-conserved model are similar and omitted for the sake of brevity.

### 6.4.1 Elastic

We first show that the power-law growth of the shock radius  $R_t$ , the number of moving particles  $N_t$ , and the total energy  $E_t$ , as obtained in Sec. 6.3 using scaling arguments, is correct, using event-driven molecular dynamics simulations. For the elastic system, the scaling arguments predict  $R_t \sim t^{3/4}$ ,  $E_t \sim t$ , and  $N_t \sim t^{3/2}$  in two dimensions and  $R_t \sim t^{3/5}$ ,  $E_t \sim t$ , and  $N_t \sim t^{9/5}$  in three dimensions. The results from simulations, shown in Figs. 6.4(a)–6.4(c) for  $R_t$ ,  $E_t$ , and  $N_t$ , respectively, are in excellent agreement with the above scaling and confirm the value of the exponent  $\alpha$  as given by Eq. (6.4).

The scaling argument leading to the exponent in Eq. (6.4) assumes the existence of only one length and one velocity scale, and leads to the correct scaling of the bulk quantities  $R_t$ ,  $N_t$ , and  $E_t$  with time. This assumption may be further checked by studying the scaling behavior of local space-dependent physical quantities. We define coarse-grained radial density distribution function  $\rho(r, t)$  as the number of moving particles per unit volume, located within a shell of radius of  $r$  to  $r + dr$ . Similarly, the radial velocity distribution function  $v(r, t)$  and the radial energy distribution function  $e(r, t)$  are defined as the average radial velocity of particles and the average kinetic energy per unit volume, respectively, contained within the shell at any time  $t$ . We expect these local coarse-grained quantities to have the following scaling forms:

$$\begin{aligned}\rho(r, t) &\sim f_\rho(r/t^\alpha), \\ v(r, t) &\sim t^{\alpha-1} f_v(r/t^\alpha), \\ e(r, t) &\sim t^{-\beta} f_e(r/t^\alpha),\end{aligned}\tag{6.7}$$

where  $\beta = 2(1 - \alpha)$ , since  $e$  scales as  $v^2$ .

In Figs. 6.5(a) and 6.5(b), when  $\rho(r, t)$  for the elastic system is plotted against the scaled distance  $r/t^\alpha$ , the data for different times collapse onto a single curve for  $\alpha = 3/4$  in two dimensions and for  $\alpha = 3/5$  in three dimensions. The curve reveals that there is

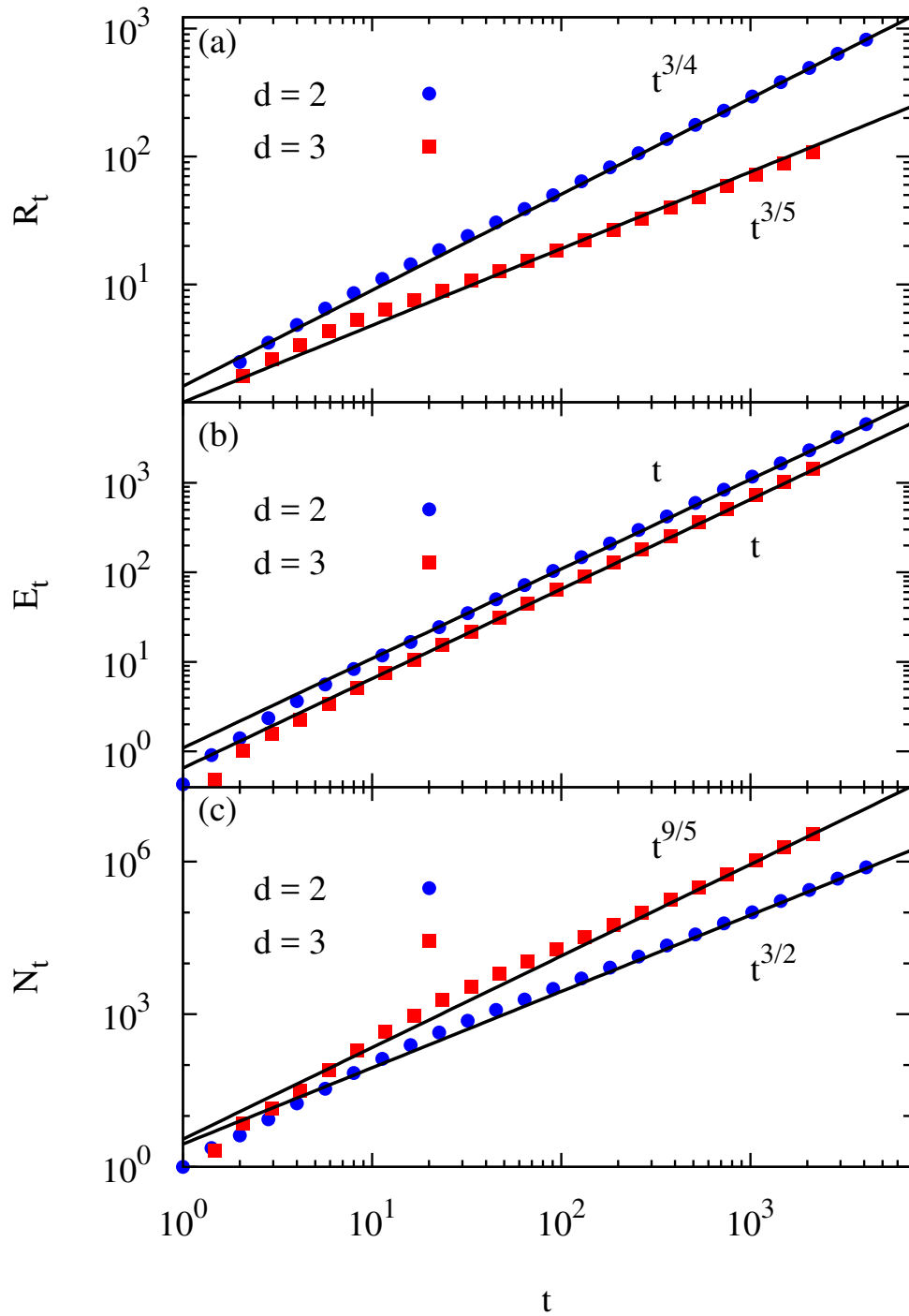


Figure 6.4: Simulation results for the elastic system ( $r = 1$ ) for the temporal variation of (a) radius  $R_t$ , (b) kinetic energy  $E_t$ , and (c) number of moving particles  $N_t$  in two and three dimensions. The solid lines are power laws with exponents as predicted by the scaling arguments presented in the text. The data are for the conserved model.

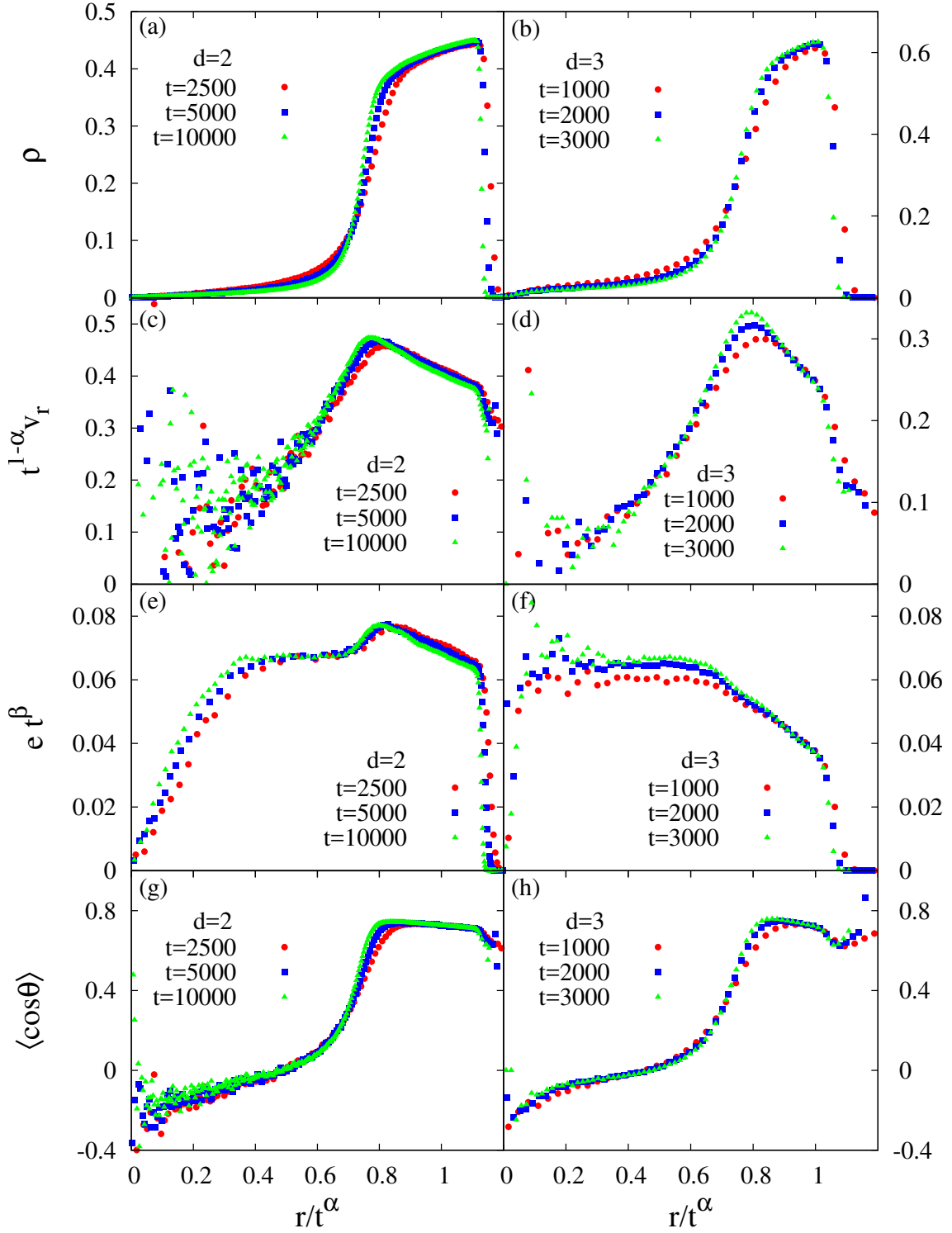


Figure 6.5: Scaled radial distribution functions against scaled distances  $r/t^\alpha$  for the elastic gas: (a)  $\rho(r, t)$ , (c)  $v(r, t)$ , (e)  $e(r, t)$ , and (g)  $\langle \cos \theta(r, t) \rangle$  in two dimensions and (b), (d), (f), and (h) corresponding quantities in three dimensions. Here  $\alpha = 3/(d + 2)$ , as in Eq. (6.4), and  $\beta = 2(1 - \alpha)$ . The data are for the conserved model.

a substantial number of moving particles spread out between the location of the shock front (around scaled distance  $r/t^\alpha \approx 1$ ) and scaled distances approximately equal to 0.5. However, the curve is nonzero and decreases to zero (as a power-law) for small distances. Thus the region of disturbed particles does not have an empty core, unlike the case of the inelastic system, as we will see below. From Figs. 6.5(c)–6.5(f) we observe that data for  $v(r, t)$  and  $e(r, t)$  also collapse onto a single curve in both two and three dimensions when scaled as in Eq. (6.7) with the same values of  $\alpha$ . Both radial velocity and density initially increase as the distance from the shock front increases. This leads to more compaction near the shock front due to faster particles pushing against the slower particles. Finally, in order to understand better the direction of motion of the particles in this driven gas, we calculate the distribution function of  $\langle \cos \theta(r, t) \rangle$ , where  $\theta$  is the angle made by the instantaneous particle velocity with respect to the outward unit radial vector at its location, and the averaging is performed over all particles contained within the shell from radius  $r$  to  $r + dr$ . In Figs. 6.5(g) and 6.5(h) we see that for small values of the scaled distance less than 0.2 the scaling function is negative, while for scaled distances greater than 0.8, its value is positive and close to 1, for both two and three dimensions. This implies that near the shock front the particles are mostly directed radially outward, while near the center of the sphere the particles are on average moving inward, a feature related to the fact that the particle collisions are elastic. The inward-moving particles are responsible for the transfer of radial momentum across the origin and lead to the breakdown of conservation of radial momentum in a particular direction.

## 6.4.2 Inelastic

Now we turn to the case more relevant to granular matter, namely, of systems with particles suffering *inelastic* collisions. The scaling dependence on time  $t$  of various quantities in such systems relies on the basic assumption of radial momentum growing linearly as a function of time  $t$  (see Sec. 6.3). In Fig. 6.2 we saw that the perturbed particles cluster in

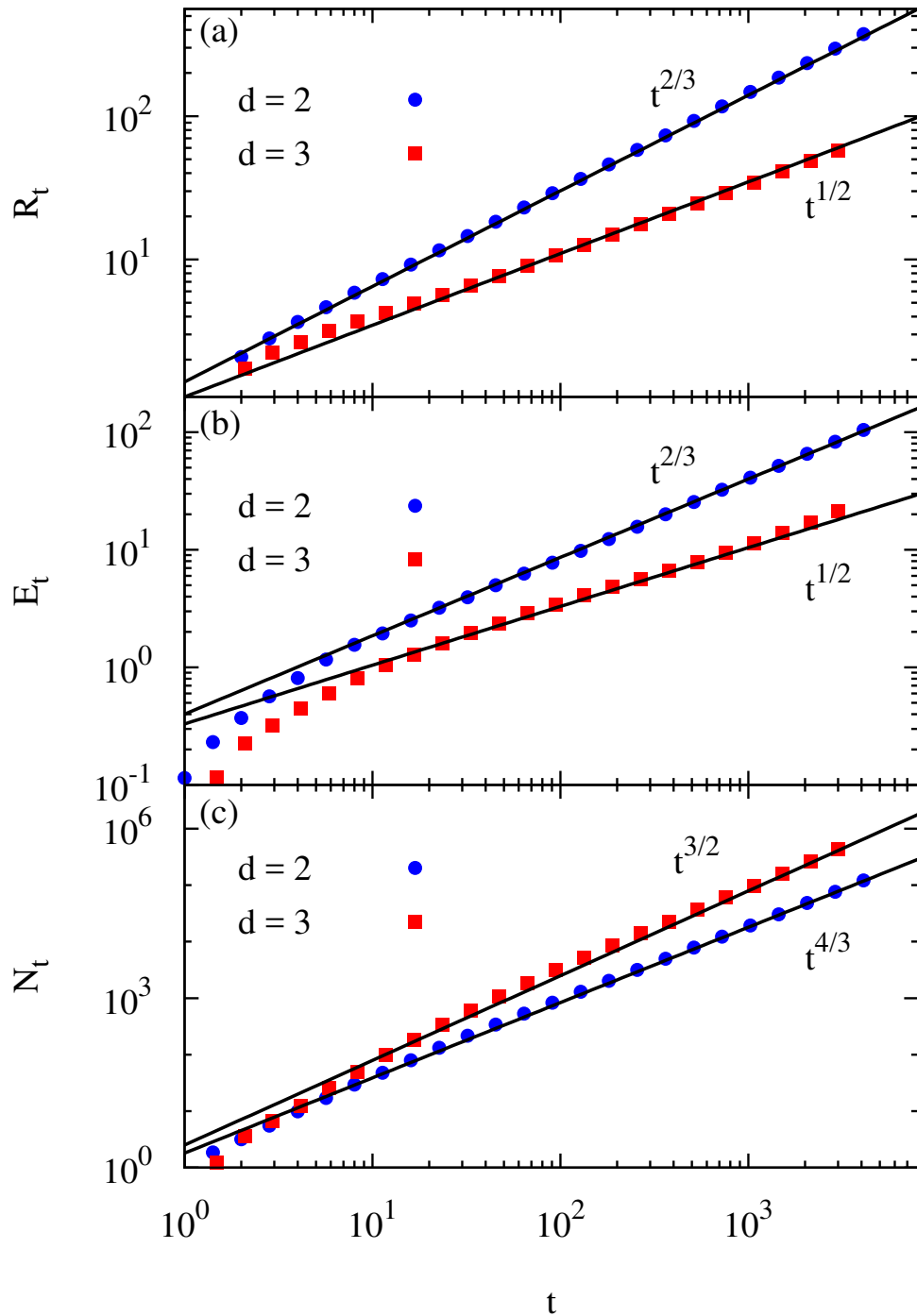


Figure 6.6: Simulation results for the inelastic system ( $r = 0.1$ ) for the temporal variation of (a) radius  $R_t$ , (b) kinetic energy  $E_t$ , and (c) number of moving particles  $N_t$  in two and three dimensions. The solid lines are power laws with exponents as predicted by the scaling arguments presented in the text. The data are for the conserved model.

an outward moving narrow band. For the inelastic system, the scaling arguments predict  $R_t \sim t^{2/3}$ ,  $E_t \sim t^{2/3}$ , and  $N_t \sim t^{4/3}$  in two dimensions and  $R_t \sim t^{1/2}$ ,  $E_t \sim t^{1/2}$ , and  $N_t \sim t^{3/2}$  in three dimensions. The results from simulations, shown in Fig. 6.6(a)–6.6(c) for  $R_t$ ,  $E_t$ , and  $N_t$ , respectively, are in excellent agreement with the above scaling and confirm the value of the exponent  $\alpha$  as given by Eq. (6.5).

Next we study the radial distribution functions for the inelastic gas and compare them with the elastic cases considered in Sec. 6.4.1. The data for the different distributions for different times collapse onto a single curve when scaled as in Eq. (6.7) with  $\alpha$  as in Eq. (6.5) for both two dimensions [see Figs. 6.7(a), 6.7(c), 6.7(e), and 6.7(g)] and three dimensions [see Figs. 6.7(b), 6.7(d), 6.7(f), and 6.7(h)]. From Figs. 6.7(a) and 6.7(b) we see that the particle density is highly localized between scaled distances 0.8 and 1 and falls to zero rapidly for smaller scaled distances; this is to be compared to the elastic gases [see Figs. 6.5(a) and 6.5(b)] where there is a larger spatial spread of density. Similar spatial localization is also observed in the velocity and energy distribution functions [see Fig. 6.7(c)–6.7(f)]. Another clear indication of the narrow banding of inelastic particles moving nearly perfectly radially outward is that the distribution  $\langle \cos \theta(r, t) \rangle$  approaches the value 1 [see Figs. 6.7(g) and 6.7(h)]. Like for the elastic case, the radial velocity increases as one moves away from the shock front, stabilizing the dense bands containing the particles.

## 6.5 Comparison with experiments

There are quite a few experiments [21, 65, 23, 22, 24] that study pattern formation in a layer of granular matter driven locally at the center through the injection of another material, gas or liquid, but not all of them study physical quantities, which is relevant for the predictions of our model. In this section we discuss two experiments that provide quantitative data on driven granular particles and we show how our scaling theory and

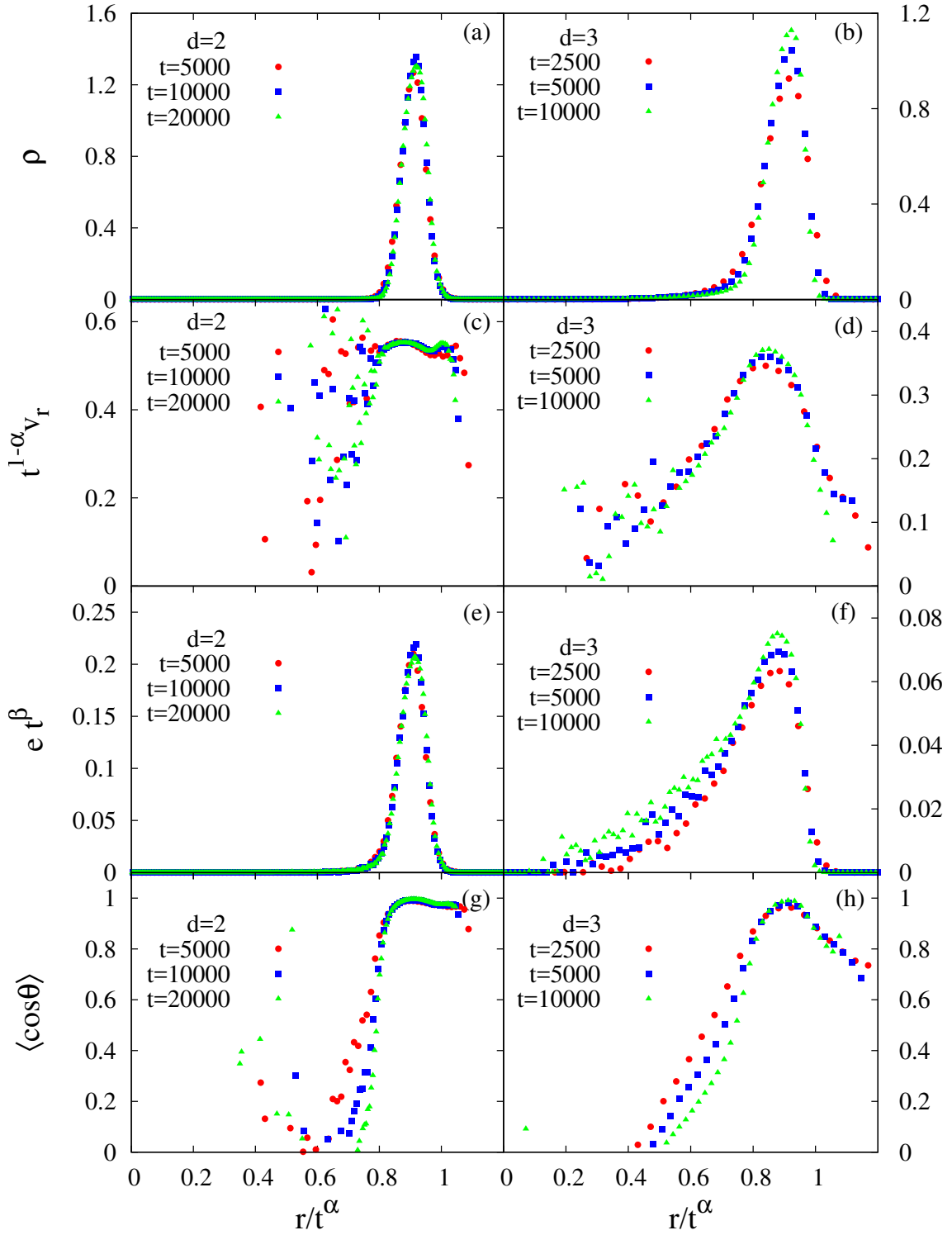


Figure 6.7: Scaled radial distribution functions against scaled distances  $r/t^\alpha$  for the inelastic gas: (a)  $\rho(r, t)$ , (c)  $v(r, t)$ , (e)  $e(r, t)$ , and (g)  $\langle \cos\theta(r, t) \rangle$  in two dimensions and (b), (d), (f), and (h) corresponding quantities in three dimensions. Here  $\alpha = 2/(d + 1)$ , as in Eq. (6.5), and  $\beta = 2(1 - \alpha)$ . The data are for the conserved model.



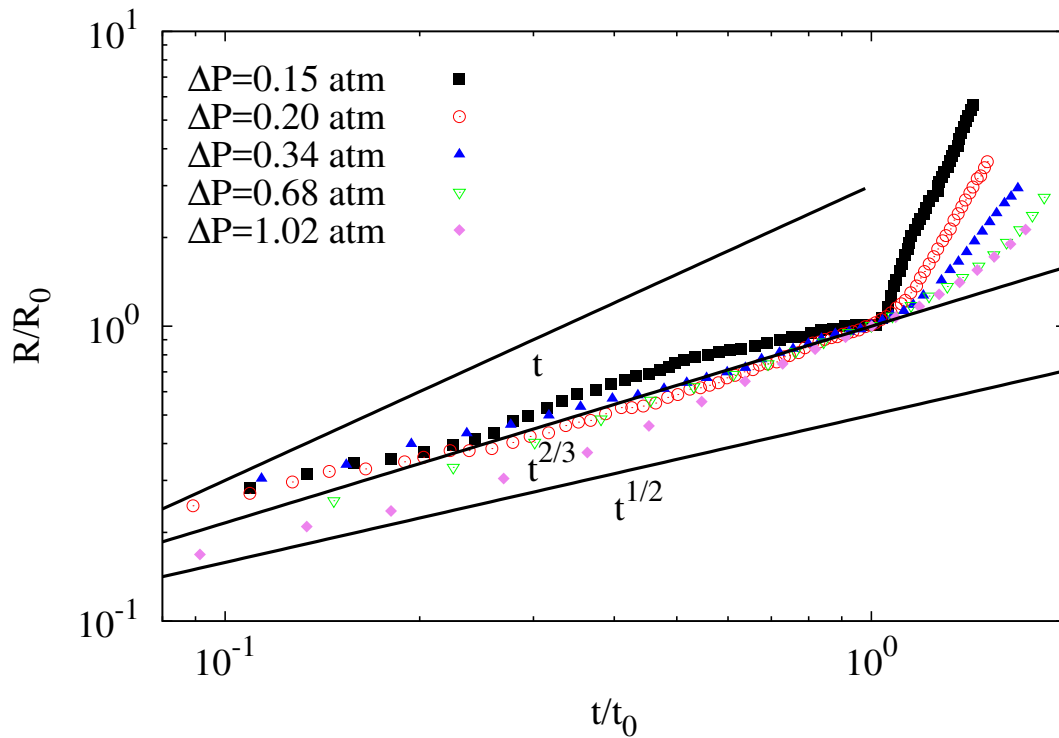


Figure 6.8: Experimental data (taken from Ref. [21]) for the scaled radius  $R$  of the longest finger from the center, as a function of normalized time  $t/t_0$ . Here  $R_0 = R(t_0)$ . The data have been plotted for different gas overpressures. The solid lines are power laws  $t^{1/2}$ ,  $t^{2/3}$ , and  $t^1$  and are shown for reference.

simulations provide an explanation for the radial growth law as seen in these experiments.

The first experiment of interest is pattern formation in spherical glass beads that are distributed uniformly within a circular Hele-Shaw cell [21]. The beads, initially at rest, were perturbed by the continuous injection of pressurized nitrogen through a hole at the center of the top plate of the cell. The driving was uniform (similar to what we assume in this work). The cell boundary was open so that any bead driven to the edge could freely flow out of the cell. The patterns formed were recorded with high-speed camera. When the driving pressure was high enough, the continuous perturbation led to the formation of a time-dependent growing viscous fingering pattern. Our interest is the radial growth law of this pattern in the early stage; at the late stage beyond some characteristic time  $t_0$ , a wild growth in radius due to effect of boundaries is seen, which is not of interest in this chap-

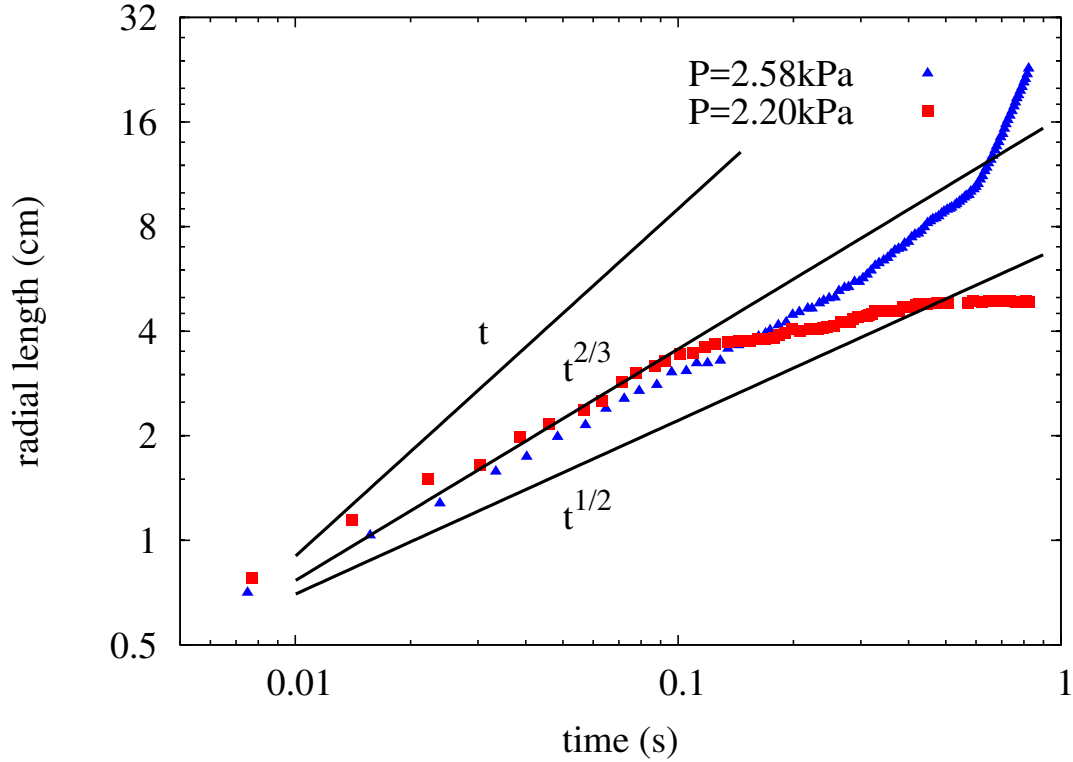


Figure 6.9: Experimental data (taken from Ref. [22]) for the growth of maximum radial coordinate of the central zone of disturbance with time for two different values of injection pressures. The solid lines are power laws  $t^{1/2}$ ,  $t^{2/3}$ , and  $t^1$  and are shown for reference.

ter. We replot the published data [Fig. 1(c) in Ref. [21]] in Fig. 6.8 for scaled radius  $R/R_0$  against scaled time  $t/t_0$ , where  $R_0 = R(t_0)$ . Quite strikingly, we find that the data converge close to the power-law  $R_t \sim t^{2/3}$ , as shown in Fig. 6.8, consistent with our theoretical prediction for the two-dimensional inelastic system [see Eq. (6.5)]. However, the scaling analysis assumes that the only means of dissipation is inelasticity. The experiment has dissipative frictional forces too, but it is evident from the data being consistent with the power-law that possibly the frictional effect is nullified by the critical pressure, beyond which beads start moving, and eventually inelasticity remains as the dominant mechanism of dissipation. We note that the experimental paper [21] erroneously mentions a linear growth of radius, but it is clear that the line proportional to  $t$  in Fig. 6.8 describes the data poorly. We also note that the power-law  $t^{1/2}$  in Fig. 6.8 is a poorer fit to the data than the power-law  $t^{2/3}$ .

We look at another similar experiment with granular material confined in a circular Hele-Shaw cell with central air injection [22]. When the injection pressure is sufficient enough, the particles in the system move out by forming a central (roughly circular) region devoid of particles. Around this central region, there is a zone where the granular material is compacted. The patterns formed have been recorded by using a high-speed, high-resolution CCD camera. The data obtained from this experiment [Fig. 13(a) in Ref. [22]] also follow the power-law  $R_t \sim t^{2/3}$  as shown in Fig. 6.9, consistent with our growth-law exponent [see Eq. (6.5) with  $d = 2$ ]. We note that the power laws  $t^{1/2}$  and  $t^1$  in Fig. 6.9 are poorer fits to the data than the power-law  $t^{2/3}$ . Thus, again we see that the simple scaling law obtained from the dominance of inelastic dissipation, and band formation, is experimentally relevant.

## 6.6 Conclusion and discussion

We studied shock propagation in a granular system that is continuously driven in a localized region. We analyzed both the elastic and inelastic systems through scaling arguments and extensive event-driven molecular dynamics simulations. By identifying that energy grows linearly in the elastic system and radial momentum grows linearly in the inelastic system, the exponents governing the power-law growth of bulk quantities such as radius of disturbance and number of moving particles were obtained. For the inelastic system, the linear growth of radial momentum crucially depended on the formation of dense bands enclosing an empty region, due to inelastic collision, as seen in the simulations. There are very few driven granular systems where exact results can be obtained. The solution in this chapter provides an example where the exponents, presumably exact, may be determined through scaling arguments.

We analyzed two experiments on pattern formation that arise due to the injection of a gas at a localized point in a two-dimensional granular medium. The experimentally obtained

radial growth of the pattern was shown to be consistent with the results in this chapter, even though the present study ignores friction that would appear to be relevant in experiments. The experimental patterns show the formation of bands that have fractal structure, which is not captured by our model. However, the detailed structure of the bands does not play a role in determining the growth-law exponent, as the scaling arguments required only conservation of radial momentum, which in turn depends only on the existence of a band enclosing an empty region and not on its structure.

We described numerical results for the model where the injected energetic particles were removed from the system after their first collision. However, we presented scaling arguments to show that the power-law exponents for the non-conserved model, in which the injected energetic particles remain in the system, are identical to that of the conserved model. Simulations are also consistent with the predictions of scaling theory. Such models may be valid for experiments where granular material is driven through injection of other granular material.

Unlike the power-law exponents, it does not appear to be possible to analytically determine the form of the scaling functions for the different local densities. For the elastic system, one might ask whether the TvNS solution [1, 3, 2] that describes shock propagation following an intense blast may be modified to the case of continuous driving. The local conservation laws of density, energy, and momentum continue to hold for localized continuous driving away from the source. However, we find in our preliminary studies that the solution develops singularities at a finite distance between the origin and the shock front. This could be because the additional assumption of local thermal equilibrium made in the TvNS solution may not hold when the driving is continuous. A detailed analysis of the elastic case is a promising area for future study.

# Chapter 7

## Summary and outlook

In this thesis, we have studied shock propagation in dilute media.

In chapter 4 we revisited the classic solution describing the propagation of a blast wave through a medium at rest, following an intense explosion. We compared the TvNS solution for the radial distribution of pressure, temperature, density, and flow velocity fields with results from large scale event-driven molecular dynamics simulations of hard spheres in three dimensions. We find that the TvNS solution fails to describe the numerical data well. In particular, the power-law behavior away from the shock front for temperature and density have different exponents in the theory and simulations.

The TvNS theory was modified by using a virial equation of state for the hard sphere gas instead of the ideal gas constitutive relation. We find that the hydrodynamic solution does not noticeably change beyond the inclusion of six virial coefficients. We restricted our analysis to the known ten virial coefficients. While inclusion of the more realistic virial equation of state modifies the theoretical predictions, especially near the shock front, it does not modify any of the exponents, and thus fails to describe the simulation data.

We also checked the different assumptions of the TvNS theory. The assumption of local equilibrium is a key assumption of the TvNS solution. In particular, the main consequence

of this assumption that goes into the theory is the existence of an equation of state for the gas. Though the numerics and theory do not agree for the scaling functions, surprisingly, the local pressure, temperature and density satisfy the virial equation of state for the hard sphere gas very well, except for a small deviation near the shock front [see Fig. 4.8]. On the other hand, the radial velocity fluctuations are not gaussian, and is skewed towards positive fluctuations. This shows that local equilibrium is not attained. The hydrodynamic equations correspond to the collision less limit of the Boltzmann equation, and does not ensure equilibration.

One way to understand the role of the observed skewed distributions would be to study a system where the local velocities are reassigned at a constant rate from a Maxwell-Boltzmann distribution with the local temperature, and ask whether any qualitative changes are observed. This is a promising area for future study. This model also can be extended to study the response of a system of binary mixtures to a sudden impact. This may give rise to a density gradient along with temperature gradient. The disturbance caused by the shock is on an average spherically symmetric. In the thesis, we have focussed on the average behavior and ignored the fluctuations. These fluctuations could give rise to instabilities and can be used to understand the instabilities shown in astrophysical systems and so opens applications to the area of astrophysical systems. We studied the system where the particles move radially outward following a localized perturbation. Instead of this kind of explosion problem, it is also interesting to study the astrophysically important phenomena called implosion where the particles are migrating to a localized region. Finally, we have assumed that the ambient temperature is zero. Introducing an ambient temperature would allow us to study the crossover from strong to weak shocks. This is a promising area for further study.

Earlier molecular dynamics simulations in two dimensions [17] found that the simulations reproduce well the TvNS solution for low to medium densities, except for a small difference in the discontinuities at the shock front. Also, a slight discrepancy was observed near

the shock center. When the number density of the ambient gas is high, the TvNS solution did not describe well the data near the shock front [17]. This is contrary to our results in three dimensions where the TvNS solution does not match with simulation. So, in chapter 5, we compared the TvNS solutions for the radial distributions for the thermodynamic quantities in two dimensions with the solutions from large scale event-driven simulations in two dimensions. We doubtlessly found that the results from theory in two dimensions do not match with the results from simulation in two dimensions. We revisited all the assumptions in theory in the similar way as we did in three dimensional study.

In chapter 6, we studied shock propagation in a granular system that is continuously driven in a localized region. We analyzed both the elastic and inelastic systems through scaling arguments and extensive event-driven molecular dynamics simulations. By identifying that energy grows linearly in the elastic system and radial momentum grows linearly in the inelastic system, the exponents governing the power-law growth of bulk quantities such as radius of disturbance and number of moving particles were obtained. For the inelastic system, the linear growth of radial momentum crucially depended on the formation of dense bands enclosing an empty region, due to inelastic collision, as seen in the simulations. There are very few driven granular systems where exact results can be obtained. The solution in this chapter provides an example where the exponents, presumably exact, may be determined through scaling arguments.

We analyzed two experiments on pattern formation that arise due to the injection of a gas at localized point in a two-dimensional granular medium. The experimentally obtained radial growth of the pattern was shown to be consistent with the results in this thesis, even though the present study ignores friction that would appear to be relevant in experiments. The experimental patterns show the formation of bands that have fractal structure, which is not captured by our model. However, the detailed structure of the bands does not play a role in determining the growth-law exponent, as the scaling arguments required only conservation of radial momentum, which in turn depends only on the existence of a band

enclosing an empty region and not on its structure.

In the case of driven granular systems, which we studied, the injection of particles with different size from those in the system, can retain the fingering patterns observed in experiments. Another fascinating case is the problem of splatter, in which the particles are confined in half-space and perturb this system. Thus the study of shock propagation followed by sudden impact and continuous perturbation, offers a variety of possibilities for the future.



# Bibliography

- [1] G. Taylor, “The formation of a blast wave by a very intense explosion. i. theoretical discussion,” *Proc. R. Soc. Lond. A*, vol. 201, pp. 159–174, 1950.
- [2] J. von Neumann, “The point source solution,” in *Collected Works*, pp. 219–237, New York: Pergamon Press, 1963.
- [3] L. Sedov, *Similarity and Dimensional Methods in Mechanics*. Florida: CRC Press, 10 ed., 1993.
- [4] G. Taylor, “The formation of a blast wave by a very intense explosion. ii. the atomic explosion of 1945,” *Proc. R. Soc. Lond. A*, vol. 201, pp. 175–186, 1950.
- [5] L. Sedov, “Propagation of strong blast waves,” *Prikl. Mat. Mech*, vol. 10, pp. 241–250, 1946.
- [6] M. J. Edwards, A. J. MacKinnon, J. Zweiback, K. Shigemori, D. Ryutov, A. M. Rubenchik, K. A. Keilty, E. Liang, B. A. Remington, and T. Ditmire, “Investigation of ultrafast laser-driven radiative blast waves,” *Phys. Rev. Lett.*, vol. 87, p. 085004, August 2001.
- [7] A. Edens, T. Ditmire, J. Hansen, M. Edwards, R. Adams, P. Rambo, L. Ruggles, I. Smith, and J. Porter, “Study of high mach number laser driven blast waves,” *Phys. Plasmas*, vol. 11, pp. 4968–4972, October 2004.

- [8] A. S. Moore, D. R. Symes, and R. A. Smith, “Tailored blast wave formation: Developing experiments pertinent to laboratory astrophysics,” *Phys. Plasmas*, vol. 12, pp. 052707–1–052707–7, May 2005.
- [9] T. Antal, P. L. Krapivsky, and S. Redner, “Exciting hard spheres,” *Phys. Rev. E*, vol. 78, p. 030301, Sep 2008.
- [10] Z. Jabeen, R. Rajesh, and P. Ray, “Universal scaling dynamics in a perturbed granular gas,” *Eur. Phys. Lett.*, vol. 89, p. 34001, 2010.
- [11] A. Ghoniem, M. Kamel, S. Berger, and A. Oppenheim, “Effect of internal heat transfer on the structure of self-similar blast waves,” *J. Fluid Mech*, vol. 117, pp. 473–491, 1982.
- [12] J. VonNeumann and R. Richtmyer, “A method for the numerical calculation of hydrodynamic shocks,” *Journal of Applied Physics*, vol. 21, p. 232, 1950.
- [13] M. N. Plooster, “Shock waves from line sources: numerical solutions and experimental measurements,” *The Phys. Fluids*, vol. 13, p. 2665, 1970.
- [14] G. Guderley, “Powerful spherical and cylindrical compression shocks in the neighbourhood of the centre and of the cylinder axis,” *Lufifahrtforschung*, vol. 19, pp. 302–312, 1942.
- [15] R. B. Lazarus, “self-similar solutions for converging shocks and collapsing cavities,” *SIAM J. Numer. Anal.*, vol. 18, pp. 316–371, 1981.
- [16] R. Anand, “Shock dynamics of strong imploding cylindrical and spherical waves with non-ideal gas effects,” *Wave Motion*, vol. 50, pp. 1003–1015, 2013.
- [17] M. Barbier, D. Villamaina, and E. Trizac, “Microscopic origin of self-similarity in granular blast waves,” *Phys. Fluids*, vol. 28, p. 083302, 2016.
- [18] H. M. Jaeger, S. R. Nagel, and R. P. Behringer, “Granular solids, liquids, and gases,” *Rev. Mod. Phys.*, vol. 68, pp. 1259–1273, Oct 1996.

- [19] I. S. Aranson and L. S. Tsimring, “Patterns and collective behavior in granular media: Theoretical concepts,” *Rev. Mod. Phys.*, vol. 78, pp. 641–692, Jun 2006.
- [20] L. P. Kadanoff, “Built upon sand: theoretical ideas inspired by granular flows,” *Rev. Mod. Phys.*, vol. 71, p. 435, 1999.
- [21] X. Cheng, L. Xu, A. Patterson, H. M. Jaeger, and S. R. Nagel, “Towards the zero-surface-tension limit in granular fingering instability,” *Nat Phys*, vol. 4, p. 234, 2008.
- [22] O. Johnsen, R. Toussaint, K. J. Måløy, and E. G. Flekkøy, “Pattern formation during air injection into granular materials confined in a circular hele-shaw cell,” *Phys. Rev. E*, vol. 74, p. 011301, Jul 2006.
- [23] S. F. Pinto, M. S. Couto, A. P. F. Atman, S. G. Alves, A. T. Bernardes, H. F. V. de Resende, and E. C. Souza, “Granular fingers on jammed systems: New fluid-like patterns arising in grain-grain invasion experiments,” *Phys. Rev. Lett.*, vol. 99, p. 068001, Aug 2007.
- [24] H. Huang, F. Zhang, P. Callahan, and J. Ayoub, “Granular fingering in fluid injection into dense granular media in a hele-shaw cell,” *Phys. Rev. Lett.*, vol. 108, p. 258001, June 2012.
- [25] L. Woltjer, “Supernova remnants,” *Ann. Rev. Astron. Astrophys.*, vol. 10, pp. 129–158, 1972.
- [26] S. Gull, “A numerical model of the structure and evolution of young supernova remnants,” *Mon. Not. R. Astr. Soc.*, vol. 161, pp. 47–69, 1973.
- [27] D. F. Cioffi, C. F. McKee, and E. Bertschinger, “Dynamics of radiative supernova remnants,” *The Astrophysical Journal*, vol. 334, pp. 252–265, 1988.
- [28] J. P. Ostriker and C. F. McKee, “Astrophysical blastwaves,” *Rev. Mod. Phys.*, vol. 60, pp. 1–68, Jan 1988.

- [29] Y. B. Zel'dovich and Y. P. Raizer, *Physics of Shock Waves and High Temperature Hydrodynamic Phenomena*. New York: Dover Publications, Inc., 2002.
- [30] A. Abdel-Raouf and W. Gretler, "Quasi-similar solutions for blast waves with internal heat transfer effects," *Fluid Dyn. Res.*, vol. 8, pp. 273–285, 1991.
- [31] H. Steiner and W. Gretler, "The propagation of spherical and cylindrical shock waves in real gases," *Phys. Fluids*, vol. 6, p. 2154, 1994.
- [32] R. Latter, "Similarity solution for spherical shock wave," *Journal of Applied Physics*, vol. 26, p. 954, 1955.
- [33] H. L. Brode, "Numerical solutions of spherical blast waves," *Journal of Applied Physics*, vol. 26, p. 766, 1955.
- [34] E. T. Vishniac, "The dynamic and gravitational instabilities of spherical shocks," *The Astrophysical Journal*, vol. 274, pp. 152–157, 1983.
- [35] G. Whitham, *Linear and Nonlinear Waves*. New York: Wiley, 1974.
- [36] T. Hirschler and H. Steiner, "A self-similar solution for the implosion problem in a dusty gas," *Fluid Dyn. Res.*, vol. 32, pp. 61–67, 2003.
- [37] N. F. Ponchaut, H. Hornung, D. Pullin, and C. Mouton, "On imploding cylindrical and spherical shock waves in a perfect gas," *J. Fluid Mech.*, vol. 560, pp. 103–122, 2006.
- [38] V. I. Dokuchaev, "Self-similar shock solution with sustained energy injection," *Astronomy and Astrophysics*, vol. 395, pp. 1023–1029, July 2002.
- [39] S. Falle, "A numerical calculation of the effect of stellar winds on the interstellar medium," *Aston. and Astrophys.*, vol. 43, pp. 323–336, 1975.
- [40] V. Berezhinsky and V. Dokuchaev, "Hidden source of high-energy neutrinos in collapsing galactic nucleus," *Astroparticle Physics*, vol. 15, pp. 87–96, 2001.

- [41] J. Castor, R. McCray, and R. Weaver, “Interstellar bubbles,” *The Astrophysical Journal*, vol. 200, pp. L107–L110, 1975.
- [42] R. Weaver, R. McCray, and J. Castor, “Interstellar bubbles. ii. structure and evolution,” *The Astrophysical Journal*, vol. 218, pp. 377–395, 1977.
- [43] M. Barbier, D. Villamaina, and E. Trizac, “Blast dynamics in a dissipative gas,” *Phys. Rev. Lett.*, vol. 115, p. 214301, November 2015.
- [44] P. K. Haff, “Grain flow as a fluid-mechanical phenomenon,” *J. Fluid Mech*, vol. 134, pp. 401–430, 9 1983.
- [45] I. Goldhirsch and G. Zanetti, “Clustering instability in dissipative gases,” *Phys. Rev. Lett.*, vol. 70, pp. 1619–1622, Mar 1993.
- [46] S. McNamara and W. R. Young, “Dynamics of a freely evolving, two-dimensional granular medium,” *Phys. Rev. E*, vol. 53, pp. 5089–5100, May 1996.
- [47] E. Ben-Naim, S. Y. Chen, G. D. Doolen, and S. Redner, “Shocklike dynamics of inelastic gases,” *Phys. Rev. Lett.*, vol. 83, pp. 4069–4072, Nov 1999.
- [48] M. Shinde, D. Das, and R. Rajesh, “Violation of the prod law in a freely cooling granular gas in one dimension,” *Phys. Rev. Lett.*, vol. 99, p. 234505, Dec 2007.
- [49] M. Shinde, D. Das, and R. Rajesh, “Equivalence of the freely cooling granular gas to the sticky gas,” *Phys. Rev. E*, vol. 79, p. 021303, Feb 2009.
- [50] M. Shinde, D. Das, and R. Rajesh, “Coarse-grained dynamics of the freely cooling granular gas in one dimension,” *Phys. Rev. E*, vol. 84, p. 031310, Sep 2011.
- [51] L. Frachebourg, “Exact solution of the one-dimensional ballistic aggregation,” *Phys. Rev. Lett.*, vol. 82, pp. 1502–1505, Feb 1999.
- [52] S. Chen, Y. Deng, X. Nie, and Y. Tu, “Clustering kinetics of granular media in three dimensions,” *Physics Letters A*, vol. 269, pp. 218–223, May 2000.

- [53] S. Miller and S. Luding, “Cluster growth in two- and three-dimensional granular gases,” *Phys. Rev. E*, vol. 69, p. 031305, Mar 2004.
- [54] X. Nie, E. Ben-Naim, and S. Chen, “Dynamics of freely cooling granular gases,” *Phys. Rev. Lett.*, vol. 89, p. 204301, Oct 2002.
- [55] S. N. Pathak, D. Das, and R. Rajesh, “Inhomogeneous cooling of the rough granular gas in two dimensions,” *Eur. Phys. Lett.*, vol. 107, p. 44001, August 2014.
- [56] S. N. Pathak, Z. Jabeen, D. Das, and R. Rajesh, “Energy decay in three-dimensional freely cooling granular gas,” *Phys. Rev. Lett.*, vol. 112, p. 038001, January 2014.
- [57] C. C. Maaß, N. Isert, G. Maret, and C. M. Aegerter, “Experimental investigation of the freely cooling granular gas,” *Phys. Rev. Lett.*, vol. 100, p. 248001, Jun 2008.
- [58] S. Tatsumi, Y. Murayama, H. Hayakawa, and M. Sano, “Experimental study on the kinetics of granular gases under microgravity,” *J. Fluid Mech.*, vol. 641, p. 521, September 2009.
- [59] A. M. Walsh, K. E. Holloway, P. Habdas, and J. R. de Bruyn, “Morphology and scaling of impact craters in granular media,” *Phys. Rev. Lett.*, vol. 91, p. 104301, September 2003.
- [60] P. T. Metzger, R. C. Latta, J. M. Schuler, and C. D. Immer, “Craters formed in granular beds by impinging jets of gas,” *AIP Conf. Proc.*, vol. 1145, p. 767, 2009.
- [61] Y. Grasselli and H. J. Herrmann, “Crater formation on a three dimensional granular heap,” *Gran Matt*, vol. 3, no. 4, pp. 201–204, 2001.
- [62] J. F. Boudet, J. Cassagne, and H. Kellay, “Blast shocks in quasi-two-dimensional supersonic granular flows,” *Phys. Rev. Lett.*, vol. 103, p. 224501, Nov 2009.
- [63] A. Vilquin, H. Kellay, and J. F. Boudet, “Shock waves induced by a planar obstacle in a vibrated granular gas,” *J. Fluid Mech.*, vol. 842, pp. 163–187, March 2018.

- [64] S. N. Pathak, Z. Jabeen, P. Ray, and R. Rajesh, “Shock propagation in granular flow subjected to an external impact,” *Phys. Rev. E*, vol. 85, p. 061301, Jun 2012.
- [65] B. Sandnes, H. A. Knudsen, K. J. Måløy, and E. G. Flekkøy, “Labyrinth patterns in confined granular-fluid systems,” *Phys. Rev. Lett.*, vol. 99, p. 038001, Jul 2007.
- [66] L. Landau and E. Lifshitz, *Course of Theoretical Physics- Fluid Mechanics*. Oxford: Butterworth-Heinemann, 1987.
- [67] G. Barenblatt, *Scaling, Self-similarity, and Intermediate Asymptotics: Dimensional Analysis and Intermediate Asymptotics*. Cambridge: Cambridge University Press, 1987.
- [68] D. C. Rapaport, *The art of molecular dynamics simulations*. Cambridge: Cambridge University Press, 2004.
- [69] J. P. Joy, S. N. Pathak, and R. Rajesh, “Shock propagation following an intense explosion: comparison between hydrodynamics and simulations,” *arXiv:1812.03638 [cond-mat.stat-mech]*, December 2018.
- [70] M. Isobe, “Hard sphere simulation in statistical physics - methodologies and applications,” *Molecular Simulation*, vol. 42, pp. 1317–1329, August 2016.
- [71] B. M. McCoy, *Advanced Statistical Mechanics*. Oxford: Oxford Science Publications, 2009.
- [72] J. P. Joy and R. Rajesh, “Shock propagation in the hard sphere gas in two dimensions: comparison between simulations and hydrodynamics,” *arXiv:1907.03416 [cond-mat.stat-mech]*, July 2019.
- [73] D. Henderson, “A simple equation of state for hard discs,” *Mol. Phys.*, vol. 30, pp. 971–972, 1975.
- [74] J. P. Joy, S. N. Pathak, D. Dibyendu, and R. Rajesh, “Shock propagation in locally driven granular systems,” *Phys. Rev. E*, vol. 96, p. 032908, September 2017.

[75] C. V. Raman., “The photographic study of impact at minimal velocities,” *Phys. Rev.*, vol. 12, pp. 442–447, Dec 1918.